

University of Southampton Research Repository ePrints Soton

Copyright © and Moral Rights for this thesis are retained by the author and/or other copyright owners. A copy can be downloaded for personal non-commercial research or study, without prior permission or charge. This thesis cannot be reproduced or quoted extensively from without first obtaining permission in writing from the copyright holder/s. The content must not be changed in any way or sold commercially in any format or medium without the formal permission of the copyright holders.

When referring to this work, full bibliographic details including the author, title, awarding institution and date of the thesis must be given e.g.

AUTHOR (year of submission) "Full thesis title", University of Southampton, name of the University School or Department, PhD Thesis, pagination

UNIVERSITY OF
Southampton

Faculty of Physical Science and Engineering



**A Study of the Lifetime of Miniaturized
Ablative Pulsed Plasma Thrusters**

by
Simone Ciaralli

Thesis for the degree of Doctor of Philosophy

Supervisors:

Prof Stephen B. Gabriel

Dr Michele Coletti

December 2014

Academic Thesis: Declaration of Authorship

I, Simone Ciaralli, declare that this thesis entitled “*A study of lifetime of miniaturized ablative pulsed plasma thrusters*” and the work presented in it are my own and have been generated by me as the result of my own original research.

I confirm that:

- This work was done wholly or mainly while in candidature for a research degree at this University;
- Where any part of this thesis has previously been submitted for a degree or any other qualification at this University or any other institution, this has been clearly stated;
- Where I have consulted the published work of others, this is always clearly attributed;
- Where I have quoted from the work of others, the source is always given. With the exception of such quotations, this thesis is entirely my own work;
- I have acknowledged all main sources of help;
- Where the thesis is based on work done by myself jointly with others, I have made clear exactly what was done by others and what I have contributed myself;
- Parts of this work have been published as:
 1. Ciaralli S, Coletti M and Gabriel S B, “*An impulsive thrust balance for μ -PPTs applications*”, *Measurement and Science Technology*, Vol. 24, 115003, 2013
 2. Coletti M, Ciaralli S and Gabriel S B, “*PPT development for nanosatellites applications: experimental results*”, *IEEE transaction on plasma science*, Vol. 43, no 1, 2015
 3. Ciaralli S, Coletti M and Gabriel S B, “*Performance and lifetime testing of a Pulse Plasma Thruster for Cubesat applications*”, submitted to *Aerospace Science and Technology*, May 2014
 4. Ciaralli S, Coletti M and Gabriel S B, “*Performance and lifetime testing of a Pulse Plasma Thruster for Cubesat applications*”, submitted to *Acta Astronautica*, November 2014

Signed:

Date:

Abstract

Miniaturized satellites are one of the fastest growing sectors in the space industry, allowing cheap access to space. These satellites are currently limited by their lack of orbit control and their lifetime is therefore determined by the natural, drag-induced, de-orbiting. These issues can be solved using a dedicated propulsion system. Cold-gas micro-thrusters, successfully flown on miniaturized satellites, are characterised by a very low specific impulse (typically less than 100 s), which considerably limits their capabilities. Moreover, they require pressurized tanks, pressure regulators and valves that may significantly increase the dry mass of the system. Pulsed Plasma Thrusters (PPTs) represent an excellent alternative to the chemical thrusters thanks to their high scalability in terms of geometry, power input and performance.

Within this research programme, the factors that affect the lifetime of solid state propellant PPTs for miniaturized satellites (e.g. Cubesat and nanosatellites) applications have been studied and addressed. Moreover, efforts have been made to optimise a PPT as a sub-system to be integrated into a satellite spacecraft. This included the characterization of the electromagnetic noise that PPTs generate and that may cause failures on the other Cubesat subsystems and a study aimed at the optimization of the PPT ignition process to produce a lighter and more reliable conditioning electronics.

To complete all these tasks, a miniaturized PPT (called PPTCUP, which stands for PPT for Cubesat Propulsion) has been developed and tested in collaboration with Mars Space Ltd and Clyde Space Ltd. Results from the PPTCUP test campaign have proved the reliability of the thruster, being able to perform a number of shots almost two times bigger than the nominal number required to demonstrate the discharge chamber lifetime. Moreover, it has been found that the unit can work correctly in the range of the Cubesat operating temperatures, withstands the mechanical vibrations during launch and has main natural frequencies compliant with the Cubesat requirements. The results of the EMC characterization test show that the electromagnetic noise generated during the main PPT discharge is mostly compliant with the requirements or small enough to be impossible to distinguish from the facility background noise.

The dedicated study to identify the best spark plug system working with a relative low breakdown voltage has shown that the semiconductor-coated spark plug insulator are able to trigger the PPT main discharge at a lower voltage (i.e. about 1700 V against the 7500 V needed for the no-coated propellant rods) without affecting the overall thruster performances.

Acknowledgments

Within the University of Southampton I would like to thank his supervisor Prof. Stephen B Gabriel for the all the discussions, advice and support over the past 3 years and all the personnel working at the Tony Davis High Voltage Laboratory, particularly technician Michael “Mike” Smith, for the provision of most of the hardware and materials needed throughout the PhD.

Within Mars Space Ltd I would like to thank my advisor and friend Dr Michele Coletti for his confidence and guidance. He dedicated a lot of time in recalling his experience on electric propulsion and PPTs, showing excellent knowledge and skills. I am also very grateful to Dr Francesco Guarducci, Miss Aloha Mingo Perez and my best friend Daniele Frollani for their invaluable help.

I would like to thank Mr Alan Kane and Mr Marcos Compadre of Clyde Space Ltd for their patience and support early on in the PhD and for all the work done together over the past 3 years.

Eternal thanks to my parents Roberta and Claudio, my sister Arianna, who have always supported me and who are my lighthouse in the darkest days of my life. Infinite thanks to my beloved friend and fiancée Laura, who I met in Southampton changing my life forever, for her patience in reading, advising and correcting this work.

Finally, I would like the dedicate this work to a Man who, even if passed away about 18 years ago, is still the most incredible person I have ever met. Thanks to him, his grandson discovered his passion for the Physics and the Math becoming the person he is now. Grazie nonno Renato.

Table of contents

Abstract.....	iii
Acknowledgments.....	iv
Table of contents.....	v
List of Figures.....	viii
List of Tables.....	xiii
Nomenclature.....	xiv
List of abbreviations.....	xvi
Chapter 1. Introduction.....	1
1.1. Research motivation.....	1
1.2. Research objective.....	2
1.3. Dissertation outline.....	3
Chapter 2. Pulsed Plasma Thrusters: literature review.....	5
2.1. General PPT overview.....	5
2.1.1. PPT discharge description.....	7
2.1.2. PPT classification.....	8
2.1.2.1. Classification by electrode shape.....	9
2.1.2.2. Classification by propellant feeding system.....	11
2.2. Solid propellant PPTs.....	12
2.2.1. PPTs performance review.....	12
2.2.2. Lifetime limiting factors.....	16
2.2.2.1. Carbonization issue.....	16
2.2.2.2. Spark plug system.....	18
2.2.3. Spark plug insulator.....	21
2.2.3.1. Semiconductor coating selection.....	22
2.2.3.2. Metal coating selection.....	25
2.2.4. Electromagnetic noise.....	26
2.3. Performance models.....	28
2.3.1. Conservation of charge equation.....	29
2.3.2. Conservation of momentum equation.....	33
2.3.3. Energy distributions and efficiencies.....	35
2.3.4. Constant element PPT discharge model.....	37
2.3.5. Variable element PPT discharge model.....	39
Chapter 3. Experimental set-up.....	45

3.1.	Experimental apparatus.....	46
3.1.1.	Vacuum facility.....	46
3.1.2.	Electrical set-up.....	47
3.2.	Diagnostics.....	50
3.2.1.	PPT electrical characterization.....	51
3.2.2.	Mass bit consumption measurement.....	51
3.2.3.	Impulse bit measurements.....	52
3.2.3.1.	Natural frequency evaluation.....	55
3.2.3.2.	Moment of inertia evaluation.....	56
3.2.3.3.	Arm displacement evaluation.....	58
3.2.3.4.	Sensor head and thruster distances from rotational axis evaluation.....	59
3.2.3.5.	Error budget.....	60
3.2.3.6.	Balance noise analysis.....	61
3.3.	PPTCUP discharge chamber engineering model (PPTCUP-EM).....	63
3.3.1.	Electrode shape.....	65
3.3.2.	Nozzle side walls shape.....	67
3.3.3.	Back-plate geometry.....	68
3.3.4.	Housing material.....	69
3.3.5.	Spark plug electrodes.....	70
3.4.	PPTCUP qualification model (PPTCUP-QM).....	71
3.4.1.	QM discharge chamber.....	72
3.4.2.	Electronic board.....	73
3.4.3.	External box.....	75
3.5.	Spark plug insulator samples.....	75
Chapter 4.	Experimental test campaigns results.....	79
4.1.	PPTCUP experimental testing overview.....	79
4.2.	PPTCUP performances.....	81
4.2.1.	PPTCUP-EM: influence of spark position on performance.....	82
4.2.2.	PPTCUP-EM: propellant feeding performance influence.....	84
4.2.3.	PPTCUP-EM: electronic board prototype performance influence.....	87
4.2.4.	PPTCUP-QM performance characterization.....	88
4.3.	Carbonization and propellant charring.....	91
4.4.	Electromagnetic noise interference.....	96
4.4.1.	Noise characterization from the PPTCUP-EM testing.....	96
4.4.2.	PPTCUP-QM EMC test results.....	100

4.4.2.1.	Conducted emissions.....	100
4.4.2.2.	Radiated emissions.....	103
4.4.2.3.	Radiated susceptibility	105
4.5.	Spark plug breakdown voltage study results.....	106
4.5.1.	Coated spark plug insulator selection	107
4.5.2.	Coated spark plug insulator characterization test.....	107
Chapter 5.	Conclusions.....	114
5.1.	Overview.....	114
5.2.	Contributions.....	115
5.2.1.	PPT discharge chamber carbonization	115
5.2.2.	PPT performance optimization	116
5.2.3.	Spark plug breakdown voltage.....	116
5.2.4.	Electromagnetic interference and compatibility	117
5.3.	Achievements.....	117
5.3.1.	Project achievements.....	117
5.3.2.	Personal achievements	118
5.4.	Future work.....	119
5.4.1.	PPTCUP-QM further development.....	119
5.4.2.	PPT numerical model development	119
5.4.3.	Spark plug breakdown voltage.....	120
ANNEX A.	NanoPPT performance results	122
1.	Experimental set-up	124
2.	Experimental results.....	125
2.1.	Electrical characteristics	125
2.2.	Impulse bit	127
2.3.	Mass bit and specific impulse	128
ANNEX B.	PPTCUP-QM environment test results	130
1.	Thermal cycling test results	130
2.	Mechanical test results.....	130
3.	EMC test results.....	133
3.1.	Conducted emissions.....	133
3.2.	Radiated emissions.....	136
List of publications	138
References	140

List of Figures

Figure 1-1 – PPTCUP shot	3
Figure 2-1 - Sketch of a solid state PPT functioning [14].....	6
Figure 2-2 – Exemplary image of a solid propellant PPT main discharge after about 100 ns from the initial spark of the igniter [25].....	7
Figure 2-3 – Deformed plume at the exit of a gas-fed PPT (p=100 mTorr of argon) [26]	8
Figure 2-4 – Flared electrodes PPT [39].....	10
Figure 2-5 - Coaxial PPT with divergent outer electrode [19].....	10
Figure 2-6 – Z-pinch PPT concept [20].	11
Figure 2-7 - PPT working principles: a) Z-pinch, b) Inverse pinch.....	11
Figure 2-8 – Breech-fed PPT [1].....	13
Figure 2-9 – Side-fed PPT [39].....	13
Figure 2-10 – V-fed PPT [42].	14
Figure 2-11 - Thrust efficiency against stored energy for different PPT [35].	15
Figure 2-12 - Main discharge chamber and “forechamber” proposed by RIAME MAI [29].	17
Figure 2-13 – RIAME MAI PPT arrangement [29]. Note the grooves on the lateral walls. .	17
Figure 2-14 - Propellant bars sublimation condition after 100,000 shots at different E_0 [48].	18
Figure 2-15 – ADD SIMP-LEX [35].	19
Figure 2-16 – Spark plug coating concept.	19
Figure 2-17 - Example of spark plug made by the Bendix Corporation [8].	20
Figure 2-18 – Scheme of a <i>triggeless</i> vacuum arc [63].	21
Figure 2-19 – Resistivity of an a-Si:H layer grown and measured in vacuum [78].....	24
Figure 2-20 – AC resistivity of an a-Ge:H layer as function of the voltage frequency [79].	25
Figure 2-21 – Amorphous-crystalline transaction (Ge layer). Note the growth of the nucleation centres [79].....	25
Figure 2-22 – Radiated signal (top) and capacitor voltage discharge (bottom) [85].	27
Figure 2-23 – EO-1 PPT radiate electric field test results [88]. The solid line is the limit set for the unit, the square and the circle markers indicate the results obtained respectively without and with the additional shield envelope.....	28
Figure 2-24 – PPT RLC circuit model.....	29
Figure 2-25 – PPT equivalent RCL circuit	30
Figure 2-26 - Concept of the propagation of the current sheet in a parallel plate electrode PPT.....	31
Figure 2-27 – Comparison of L' for different h/w values ($d_{el} = 10$ mm, $\tau = 2$ mm)	34
Figure 2-28 - Non-dimensional discharge current (constant element model).....	38

Figure 2-29 - Non-dimensional discharge voltage (constant element model)	38
Figure 2-30 - Snowplow model typical results. $E_0 = 2\text{J}$, $R = 70\text{ m}\Omega$, $L = 20\text{ nH}$, $m = 3.3\text{ g/s}$, $C = 1.7\text{ }\mu\text{F}$	41
Figure 2-31 - Slug model typical results. $E_0 = 2\text{J}$, $R = 70\text{ m}\Omega$, $L = 20\text{ nH}$, $m_{bit} = 5\text{ }\mu\text{g}$, $C = 1.7\text{ }\mu\text{F}$	43
Figure 2-32 - Thruster efficiency against efficiency parameter K	44
Figure 3-1 - Vacuum facility at Mars Space Ltd premises.	46
Figure 3-2 – EMC test vacuum facility a) bell jar with the PPTCUP-QM box, b) bell jar and pumping system.	47
Figure 3-3 – Electrical set-up used for the testing of PPTCUP and NanoPPT driven by their electronic boards	48
Figure 3-4 – GSE-2 electrical circuit.	49
Figure 3-5 – GSE-2 electrical set-up used.	50
Figure 3-6 – Mettler-Toledo XP205 high precision scale.....	52
Figure 3-7 – PPT balance set-up. PPTCUP-EM installed on the balance arm	53
Figure 3-8 – Definition of thrust misalignment and parallel thrust.	53
Figure 3-9 – Balance arm schematics (not to scale).	54
Figure 3-10 - Example of FT used to evaluate the natural oscillation frequency. In the picture $f_{nat} = 2.145 \pm 0.003\text{ Hz}$	56
Figure 3-11 - Linear fitting results to evaluate J_{arm} (slope) and k (y-axis intercept). Error bars are not shown because they would not be visible. R-square = 0.9816.....	57
Figure 3-12 – Thrust stand schematic (not to scale) showing the position of the electrical connections	57
Figure 3-13 - Example of acquired displacement signal (grey curve) and its best fitting (black curve). R-square = 0.9986.....	59
Figure 3-14 - Example of optical sensor linear region characteristic fitting.....	59
Figure 3-15 - Balance Bode diagrams ($\zeta t = 0.0145\text{ s}^{-1}$ and $\omega_0 = 13.44\text{ rad s}^{-1}$).....	62
Figure 3-16 - Induced noise $N(t)$ FT.	62
Figure 3-17 – Comparison between the inducted noise RMS and the ideal RMS amplitude (in the example $I_{bit} = 40\text{ }\mu\text{Ns}$).....	63
Figure 3-18 – 3D section of the PPTCUP-EM discharge chamber	64
Figure 3-19 – 3-D section views of PPTCUP-BB (a) and PPTCUP-EM (b).....	65
Figure 3-20 - Definition of side-fed and V-fed configurations.....	65
Figure 3-21 – 3-D models of the EM electrodes: a) Lower electrode (anode), b) Upper electrode (cathode).....	66
Figure 3-22 - Details of electrodes divergence angle.....	66
Figure 3-23 – a) Possible conducting path on the nozzle wall, due to the carbonization effects (PPTCUP-BB) [105] b) gap between the electrodes and the walls (PPTCUP-QM)..	67
Figure 3-24 – Lateral nozzle walls (a) PPTCUP-EM, (b) PPTCUP-BB.	68

Figure 3-25 – a) Configuration without back plate protection: carbon deposited on the back-plate (in green) shorting the electrodes. b) Configuration with back-plate-protection (in red): no electrodes shorting	69
Figure 3-26 – PPTCUP-BB back plate carbonization a) Boron nitride b) Macor c) Shapal-M. Pictures taken after about 1000 shots [105]	70
Figure 3-27 – 3D section of the PPTCUP-EM spark plug system (plug inserted in the <i>Close Hole</i>).	71
Figure 3-28 - PPTCUP-QM module (without the box lid).	72
Figure 3-29 - Example of possible PPTCUP-QM assembly with Cubesat structures.	72
Figure 3-30 – PPTCUP-QM discharge chamber main components	73
Figure 3-31 – PPTCUP-QM electronic board.....	74
Figure 3-32 – PPTCUP-QM grounding scheme	74
Figure 3-33 – PPTCUP spark plug insulator geometry. Dimensions are in mm.	76
Figure 3-34 – NanoPPT spark plug insulator geometry.....	77
Figure 3-35 – Tested spark plugs: a) PTFE and a-Ge:H, b) PTFE and a-Si:H, c) Macor and a-Ge:H, d) Macor and a-Si:H.....	78
Figure 4-1 – PPTCUP test campaign sequence.	80
Figure 4-2 - Comparison of the typical a) discharge current curves and b) discharge voltage curves for different spark plug positions (phase 1). Side-fed configuration.....	83
Figure 4-3 – Typical PPTCUP-BB discharge voltage curve [105]......	83
Figure 4-4 – PPTCUP-EM driven shot counter (phase 1)	85
Figure 4-5 – PPTCUP-EM <i>Ibit</i> measurements (phase 1).....	86
Figure 4-6 - Examples of typical PPT performances decay a) from [109] b) from [110].....	86
Figure 4-7 – HV board prototype used during the phase 2 of the experimental test campaign.	87
Figure 4-8 – PPTCUP-EM discharge voltage curve when powered by the HV board (phase 2).	88
Figure 4-9 – PPTCUP-QM discharge voltage comparison (phase 3)	89
Figure 4-10 - Discharge voltage fitting.....	90
Figure 4-11 - Details of the carbonization occurred in the PPTCUP-EM discharge chamber.	92
Figure 4-12 - Back plate protection at the end the test campaign (phase 1): a) discharge side b) rear side.....	93
Figure 4-13 - a) Upper and b) Lower housing cover at the end the test campaign (phase 1).93	
Figure 4-14 - Housing components (discharge side) at the end the test campaign (phase 1).94	
Figure 4-15 - SEM picture taken in the centre of divergent part of the cathode (discharge side) at the end the test campaign (phase 1).....	95
Figure 4-16 – PPTCUP-EM cathode (on the left) and anode at the end the test campaign (phase 1): a) discharge side b) rear side	95

Figure 4-17 - PTFE propellant bars charring: a) side-fed PPTCUP-EM (after about 250,000 shots, phase 1), b) PPTCUP-BB (after about 3,000 shots) [105].....	96
Figure 4-18 – PPTCUP-EM driven by HV board grounding scheme (phase 2).....	97
Figure 4-19 - Noise measurements for a thruster shot ($E = 2$ J) and spark plug only shot measured on the power line.	98
Figure 4-20 – Conducted emission test set-up.	101
Figure 4-21 – Conducted emissions (ground line, differential mode) test results. The blue and red curves represent respectively the background noise and the noise with the thruster on. The black line indicates the requirements.....	102
Figure 4-22 – EO-1 PPT conducted emissions [117].....	102
Figure 4-23 - Radiated emission test set-up.....	103
Figure 4-24 – Radiated electric field test results. The blue and red curves represent respectively the background noise and the noise with the thruster on. The black line indicates the requirements.....	104
Figure 4-25 – Radiated magnetic field test results. The blue and red curves represent respectively the background noise and the noise with the thruster on. The black line indicates the requirements.....	105
Figure 4-26 - Radiated susceptibility test set-up.....	106
Figure 4-27 – Comparison of the a) discharge current and b) discharge voltage curves.....	108
Figure 4-28 – Firing rate β trend with the number of shots.	109
Figure 4-29 - Spark plug insulators coated with a-Ge:H a) Macor new b) Macor after 15,000 shots c) PTFE new d) PTFE after 13,000 shots.....	110
Figure 4-30 – SEM picture of the a-Ge:H layer before the beginning of the test.....	111
Figure 4-31 – SEM picture of the a-Ge:H layer at the end of the lifetime: a) magnification x100 b) magnification x500. Highlighted: the cracks on the a-Ge:H layer (red circles) and traces of carbon in the shape of globules (blue circle).....	112
Figure 4-32 - Details of the carbon globules deposited on the semiconductor layer of a coated spark plug insulators.....	113
Figure A-1 – Assembled breech-fed NanoPPT.....	122
Figure A-2 – PPT electronics a) HV board b) digital board for communications and telemetry.....	123
Figure A-3 - NanoPPT configuration: a) configuration 1, nominal, b) configuration 2, “wide” bank.....	124
Figure A-4 – Electrical set-up.....	125
Figure A-5 – Discharge current curves (“wide bank” configuration).....	125
Figure A-6 – Discharge voltage curves (“wide bank” configuration).....	126
Figure A-7 – Current parameter ψ trend with shot energy (“wide bank” configuration)	126
Figure A-8 – Comparison of the typical discharge voltage curves for configuration 1 and 2.....	127
Figure A-9 – Impulse bit trend with energy.....	127

Figure A-10 – Ablated mass bit trend with energy.	128
Figure A-11 – Specific impulse trend with energy.	128
Figure B-1 – Mechanical test set-up	131
Figure B-2 – PPTCUP conducted emission tests results: a) + 3.3 V differential mode, b) + 7.6 V differential mode, c) ground differential mode, d) +3.3 V common mode and e) +7.6 V common mode.....	135
Figure B-3 – PPTCUP electric field radiated emission tests results: a) horizontal antenna arrangement, b) vertical antenna arrangement	136
Figure B-4 – PPTCUP magnetic field radiated emission tests results.	137

List of Tables

Table 1-1 – Orbit keeping capabilities (using a PPT that delivers $I_T = 44$ Ns) [5]	3
Table 2-1 – PPTs main classification.....	9
Table 2-2 – Typical PPT range of characteristics	16
Table 3-1 - Balance moment of inertia and torsional elastic constant	58
Table 3-2 – Balance error budget summary.....	61
Table 3-3 – Macor and Shapal-M physical properties comparison	70
Table 3-4 – Tested spark plug insulators	77
Table 4-1 - Comparison of the different spark plug positions performances. Side-fed configuration.....	84
Table 4-2 - Comparison of the different propellant bars configuration. Spark plug in the <i>Close Hole</i>	85
Table 4-3 – PPTCUP-EM total impulse capability.....	87
Table 4-4 – PPTCUP-QM electrical parameters and performance summary	90
Table 4-5 – RMS noise values	98
Table 4-6 - Noise emitted by the PPTCUP spark plug and the main discharge	99
Table 4-7 – Spark plug insulators selection summary	107
Table 4-8 – Summary of the NanoPPT performance validation test results.....	108
Table A-1 – NanoPPT design parameters.....	123
Table A-2 – NanoPPT electrical parameters.....	126
Table B-1 – Random vibration test parameters.....	131
Table B-2 – Low sine sweep test results.....	132

Nomenclature

A	[m ²]	Propellant Area
B	[T]	Magnetic Field
C	[F]	Capacitance
C_n		Nozzle Divergent Coefficient
D	[m]	Magnetic Dipole Length
d_{el}	[m]	Electrodes Length
E	[J]	Energy
E_0	[J]	Main Capacitor Stored Energy
f	[N/m ²]	Force Density
F	[N]	Lorentz Force
f_{nat}	[Hz]	Natural Frequency
g_0	[m/s ²]	Standard Gravity Acceleration
h	[m]	Electrodes Separation Distance
$H(s)$		Transfer Function
I	[A]	Current
I_{bit}	[Ns]	Impulse Bit
$I_{bit_{EM}}$	[Ns]	Electromagnetic Impulse Bit
I_{el}	[A]	Electric Dipole Peak Current
I_{mag}	[A]	Magnetic Dipole Peak Current
I_{sp}	[s]	Specific Impulse
I_T	[Ns]	Total Impulse
j	[A/m ²]	Current Density
J	[kgm ²]	Moment Of Inertia
K		Efficiency Parameter
k	[kgm ² /s ²]	Torsional Elastic Constant
L	[H]	Inductance
L'	[H/m]	Inductance Per Unit Of Length
L_0	[H]	Initial Inductance
L_{dip}	[m]	Electric Dipole Length
L_e	[H]	Electrode Inductance
L_p	[H]	Plasma Inductance
m	[kg]	Mass
m_{bit}	[kg]	Ablated Mass Per Shot
M_{prop}	[kg]	Propellant Mass
N	[Nm]	Noise Induced Vibration
N_{el}	[V/m]	Electric Dipole Noise
N_i	[V]	Induced Noise
N_{mag}	[V/m]	Magnetic Dipole Noise
n_{shots}		Number Of Shots
P	[W]	Power
P_2		Power Of Two
r	[m]	Radius
R	[Ω]	Resistance
R_e	[Ω]	Electrode Resistance

R_p	[Ω]	Plasma Resistance
r_{sens}	[m]	Sensor Distance
r_{th}	[m]	Thrust Distance
T	[N]	Thrust
t	[s]	Time
td	[s]	PPT Discharge Time
t_{nat}	[s]	Natural Oscillation Period
u_e	[m/s]	Propellant Exhaust Mean Velocity
v	[m/s]	Plasma Sheet Velocity
V	[V]	Voltage
V_0	[V]	Initial Voltage
w	[m]	Electrodes Width
x_{max}	[m]	Maximum Arm Displacement
x_{sens}	[m]	Sensor Displacement
α	[m/V]	Sensor Trans-Characteristic Slope
α_d	[deg]	Divergence Propellant Angle
β		Firing Rate
β_{mass}		Propellant Mass Margin
γ		Disturbance Coefficient
Γ		Total Number of Samples
δ	[m]	Plasma Sheet Thickness
δ_{coat}	[m]	Coating Thickness
δX		Uncertainty In X Measurement
η_{th}		Overall Efficiency
ζ		Damping Ratio
$\zeta\tau$	[Hz]	Torque Damping
θ	[rad]	Angular Displacement
θ_n	[rad]	Nozzle Divergence Angle
λ	[kgm ² /s]	Damping Coefficient
μ_0	[H/m]	Magnetic Permeability In Vacuum
ρ	[Ω m]	Resistivity
τ	[m]	Electrodes Thickness
ψ	[A ² s]	Current Parameter
Ψ	[V]	Raw Optical Sensor Signal
ω	[rad/s]	Angular Velocity
ω_0	[rad/s]	Natural Angular Velocity
V	[m ³]	Plasma Sheet Volume

List of abbreviations

(A-)PPT	(Ablative) Pulsed Plasma Thruster
AC	Alternate Current
AMC	Advanced Monolithic Ceramics
BB	Bread Board Model
CS	Clyde Space Ltd
DC	Direct Current
EDX	Energy Dispersive X-Ray
EM	Engineering Model
EMC	Electromagnetic Compatibility
EMI	Electromagnetic Interference
EO-1 PPT	Earth Observing 1 PPT
ESA	European Space Agency
ESL	Equivalent Series Inductance
ESR	Equivalent Series Resistance
FT	Fourier Transform
GSE	Ground Support Equipment
HV-PS	High Voltage Power Supply
IRS	Institute für Raumfahrtssysteme
LEO	Low Earth Orbit
LTA	Late Time Ablation
LV	Low Voltage
Macor	Machinable Glass Ceramics
MSL	Mars Space Ltd
PECVD	Plasma-Enhanced Chemical Vapour Deposition
PPTCUP	PPT for Cubesat Propulsion
PTFE	Polytetrafluoroethylene
QM	Qualification Model
RD	Reference Document
RF	Radio Frequency
RIAME	Research Institute of Applied Mechanics and Electrodynamics
RMS	Root Mean Square
SEM	Scanned Electron Microscope
TMIT	Tokyo Metropolitan Institute Of Technology
UoS	University Of Southampton
VAT	Vacuum Arc Thruster

Chapter 1. Introduction

1.1. Research motivation

Miniaturized satellites are one of the fastest growing sectors in the space industry, allowing cheap access to space. They are normally launched into sun-synchronous low earth orbits (LEOs) with an altitude of less than 600 km. These satellites are currently limited by their lack of orbit control and their lifetime is therefore determined by the natural, drag-induced, de-orbiting.

These issues can be solved using a dedicated propulsion system. Cold-gas micro-thrusters are a kind of chemical propulsion system that has been successfully flown on miniaturized satellites. However, they are characterised by a very low specific impulse (typically less than 100 s), which considerably limits their capabilities. Moreover, they require pressurized tanks, pressure regulators and valves that may significantly increase the dry mass of the system.

Pico-satellites, i.e. Cubesats, are characterized by a tight mass budget (e.g. 1 kg for a 1U Cubesat or 3 kg for a 3U Cubesat) and conventional chemical propulsion system might not be the best solution.

Pulsed Plasma Thrusters (PPTs) represent an excellent alternative to the chemical thrusters thanks to their high scalability in terms of geometry, power input and performance. The PPTs are an example of electric propulsion system: they belong to the electromagnetic propulsion system group, being the thrust originated by a self-induced magnetic field.

Despite the advantages of using a PPT compared with a standard cold gas thruster, PPTs that have been scaled down to match the Cubesat mission requirements and the mass and volume budgets are still affected by issues that limit their lifetime. Developed in the late 60s, PPTs are one of the first examples of electric propulsion successfully employed in space but the devices that flew in the past were too big and heavy for miniaturized satellite applications [1], [2]. Moreover, the design of such miniaturized PPTs should be optimized to allow the thruster to deliver the best performance throughout their lifetime. At last, since the device is an impulsive thruster, a dedicated study and characterization of the electromagnetic noise that the thruster might generate has to be carried out to avoid possible failures of the other subsystems and more importantly of the payload during the space flight.

1.2. Research objective

The main objective of this research programme is to study and possibly address the factors that affect the lifetime of solid state propellant PPTs for miniaturized satellites applications. A second objective is the optimization of the PPT as a subsystem to be integrated into a satellite spacecraft. This includes the characterization of the electromagnetic noise that PPTs generate and that may cause failures on the other Cubesat subsystems and a study aimed at the optimization of the PPT ignition process to produce a lighter and more reliable ignition conditioning electronics.

To complete all these tasks, a miniaturized PPT has been developed and tested (Figure 1-1), including all the possible design modifications that could improve the lifetime and the performance. In addition to that, a parallel study on the PPT spark plugs has been carried out. The spark plug is used to trigger the main discharge of a PPT and it is one of the most critical components to design because the reliability and the lifetime of a PPT mainly depend on the reliability of the spark plug.

It has to be pointed out that the design of this “optimized” PPT is based on the first model of PPT for Cubesat propulsion (PPTCUP). In the recent past, the University of Southampton, in collaboration with Mars Space Ltd and Clyde Space Ltd, successfully completed a research study funded by the ESA-ITI program producing a breadboard PPT model for Cubesat applications (PPTCUP-BB) [3], [4]. This thruster has been designed to deliver a total impulse (I_T) in the range between 28.4 and 44.0 Ns and to match the tight Cubesat mass and volume budgets. As shown in Table 1-1, the use of a PPT able to deliver $I_T = 44$ Ns can significantly increase the expected Cubesats lifetime and consequently makes them appealing for a wider range of space missions and increases their economical attractiveness.

Table 1-1 – Orbit keeping capabilities (using a PPT that delivers $I_T = 44$ Ns) [5]

Altitude	Cubesat Size	Natural Life	Life with PPTCUP	Life increase
250 km	1U	5.7d	17d	+200%
	2U	11d	22d	+100%
	3U	17d	28d	+66%
350 km	1U	2m 8d	5m 21d	+150%
	2U	4m 16 d	8m	+75%
	3U	6m 24d	10m 8d	+50%
450 km	1U	1y 5m	3y 3m	+133%
	2U	2y 10m	4y 8m	+67%
	3U	4y 2m	6y	+44%

100 cm² area, $C_D=2.2$, NRLMSISE-00 atmosphere

If the objectives of this research are achieved, the outcome of the project will be an optimized and reliable PPT. Considering the advantages of using a PPT system shown in Table 1-1, this will globally strengthen the UK’s reputation in electric propulsion (in which the UK is a European and World leader) and possibly of the UK space propulsion sector.

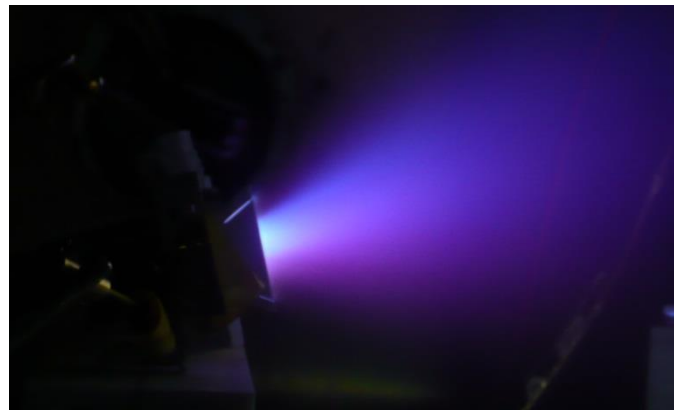


Figure 1-1 – PPTCUP shot

1.3. Dissertation outline

The structure of the dissertation shows a number of stages undertaken in order to develop a fully functional PPTCUP from its initial design stages to the final lifetime tests.

Following a brief introduction and research motivation and objectives, the rest of this dissertation consists of four more chapters.

In chapter 2, a complete literature review is reported: after a general overview of the PPT, the bibliographical search is focused on the issues that typically characterise ablative PPTs and on the studies and practical solutions that in the past different authors proposed.

The experimental apparatus developed for completing this research program, including the design and the characterization of an innovative impulsive micro-thrust balance, and the most important details of the design modifications introduced in the PPTCUP are presented in chapter 3.

In chapter 4, the results of the tests performed on the PPTCUP are reported and discussed, pointing out the achieved lifetime, the thruster performances and the electromagnetic noise generated by the unit. Moreover, the study aimed at the optimization of the spark plug process is presented.

Finally, chapter 5 provides a summary of this dissertation work, focusing on the most significant innovations found with this research program and proposes some ideas for possible future works.

Chapter 2. Pulsed Plasma Thrusters: literature review

2.1. General PPT overview

PPTs are long standing electric propulsion thrusters that are reliable, relatively simple and low cost. They can be categorized as electromagnetic devices as they accelerate neutral plasma to produce thrust. A pulsed, high-current arc discharge lasting few microseconds is produced between two electrodes: it heats, ionizes and accelerates the propellant particles through the Lorentz force generated by the interaction between the discharge itself and the self-induced magnetic field. Part of the thrust is also generated by thermal expansion particularly if a nozzle is included in the design.

Developed in the late 60s, the PPTs are one of the first examples of electric propulsion employed in space, with the Zond-2 (USSR) and the LES-6 (USA) being the first satellites to use Plasma Thrusters [1] -[2]. PPTs have been employed both for attitude and orbital control in several further satellites, like the SMS [6] - [7] and the LES-8/9 [8], [9], [10], [11]. The thrust level is generally regulated by changing the pulse repetition rate rather than varying the energy level, as the single shot impulse is usually very stable and repeatable [1], [12], [13].

A typical PPT design is shown in Figure 2-1 and consists of a pair of electrodes connected to a capacitor bank, where the electrical energy that will be used to produce the thrust is stored. The energy level can vary from few joules of the smallest thrusters to many hundreds of joules, with the related power consumption ranging from a fraction to hundreds of watts, depending on the pulse repetition rate [1].

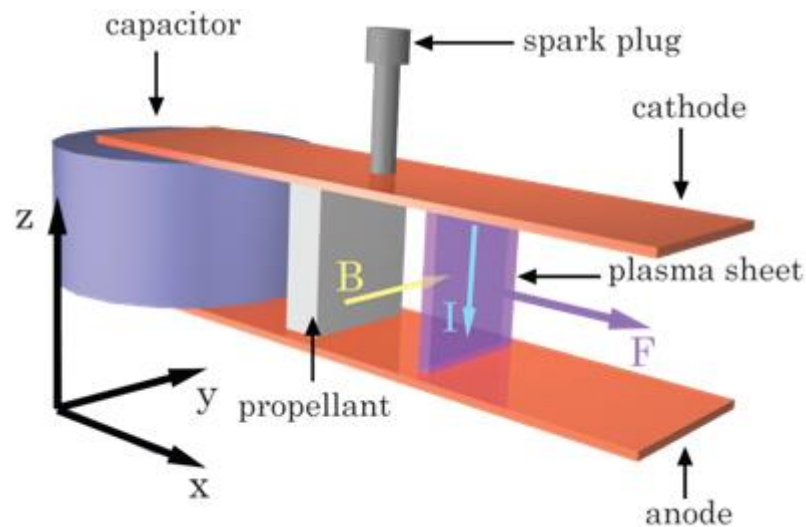


Figure 2-1 - Sketch of a solid state PPT functioning [14].

In a solid propellant PPT the discharge originates across the surface of a solid insulator, most commonly polytetrafluoroethylene (PTFE) also known as Teflon®. The main discharge is sustained by the particles ablated and ionized from the propellant surface. There are also PPTs where the space between the electrodes is filled with a gas or a liquid that is ionized by the discharge. These kinds of thruster are named gas-fed and liquid propellant PPTs respectively. Despite the choice of the propellant state, the ionized particles form a plasma sheet that is subject to the Lorentz force (F) caused by the interaction of the current flowing across the sheet (I) and the self-induced magnetic field (B), generated by the discharge current itself. Moreover, as discharge energy heats the propellant, a pressure field acts on the thruster surfaces. The propellant is also accelerated by a gasdynamic thrust [15], [16] that jointly with the electromagnetic force expels the gaseous propellant. Different authors [17], [18] confirmed experimentally that the thermodynamic and electromagnetic effects coexist, suggesting that the importance of the gasdynamic thrust component increases proportionally with amounts of available propellant in the discharge chamber.

2.1.1. PPT discharge description

The current discharge, which occurs between the PPT electrodes, consists of three sections: initiation, propagation and expulsion [1], [19], [20], [21].

The initiation of the main capacitor discharge is usually provided by a spark plug. It is charged to high voltages (up to order of tens of kV) then it produces a first discharge ionizing a small amount of propellant. The released plasma lowers the breakdown voltage between the main electrodes allowing the generation of the main discharge. At this point the energy stored into the main capacitor bank can be released [2], [22], [23]. In gas-fed PPTs the inter-electrode space is filled with propellant, until the gas density becomes so high that it reduces the dielectric strength. At this point the gas spontaneously triggers the capacitor discharge. In this way, the system reliability would be improved as the system would not need a spark plug. However as it is not possible to determine precisely the discharge timing, the gas-fed PPTs are always equipped with spark plugs [19]. At last, even if the spark plug is the most used device to ignite the main discharge, different ways have been investigated and the most promising alternative mechanism might be the use of low energy laser beam (between 0.01 and 0.5 J) [23, 24]. It has been demonstrated that the PPT discharge could be initiated by shining an IR laser pulse on the thruster back-plate [23] or on the propellant bar [24].

After the breakdown occurs, a low intensity glow discharge immediately focuses in a thin arc, i.e. a plasma sheet, located at the breech of the thruster to minimize the discharge circuit inductance (see Figure 2-2) [20]. This phenomenon is usually called skin effect, because it is similar to the confinement of high frequency currents on the external surface of conductors. The thin arc is sustained by the ionized particles that come from the available propellant between the electrodes [25].

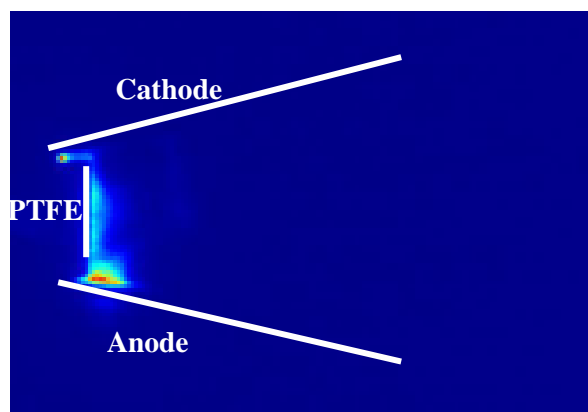


Figure 2-2 – Exemplary image of a solid propellant PPT main discharge after about 100 ns from the initial spark of the igniter [25].

The intense energy released by the discharge heats the propellant to temperatures high enough to cause its ionization. Once the arc has formed in the position that minimizes the inductance of the discharge circuit, the interaction between the self-induced magnetic field (\mathbf{B}) and the discharge current determines the Lorentz force:

$$\mathbf{f} = \mathbf{j} \times \mathbf{B} \quad (1)$$

where \mathbf{f} is the Lorentz force per unit of volume and \mathbf{j} is the current density.

The reaction force that is applied on the thruster is the thrust. In order to recover some of the thermal energy deposited into the plasma, some thrusters have flared electrodes or have even been equipped with proper nozzles [1].

When the plasma sheet reaches the end of the electrodes, pushed by the Lorentz force, it is expelled out of the thruster. To minimize the losses due to possible misalignment of the thrust vector, the velocity profile of the propellant has to be as uniform as possible. The major problem that prevents achievement of this optimal condition is the fact that the sheet might reach the end of the electrodes when the discharge is not completely extinguished because there is still some energy stored in the capacitor. If this happens the current continues to flow and the arc structure does not vanish. Since it remains attached to the electrodes extremity, it tends to warp, assuming a curved shape. This might cause a serious loss in thrust, because of the significant misalignment of the plume velocity profile. Figure 2-3 shows the light emitted by argon ions during the discharge of gas-fed PPT and captured by a camera after being filtered to exclude the glow of the neutrals and enhance the contrast in the regions where current was flowing [26]. To limit this loss, the geometry electrodes and the total capacitance of the capacitor bank where the energy is initially stored should be carefully chosen to allow the discharge to be completely extinguished once the current sheet has reached the end of the electrode [20], [27], [28].

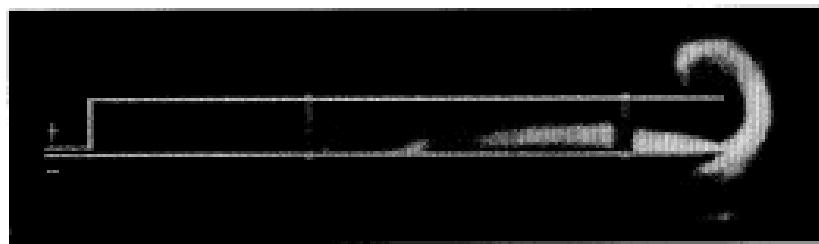


Figure 2-3 – Deformed plume at the exit of a gas-fed PPT ($p=100$ mTorr of argon) [26]

2.1.2. PPT classification

PPTs can be designed in a broad variety of configurations. Not only the energy level stored in the main capacitor bank plays an important role, but also the kind of propellant, the propellant feeding mechanism, the ignition method and the electrode configuration do significantly influence the final performance of the propulsion

system. In Table 2-1, a summary of all the most common classes of PPTs is presented. Further details on each of these groups are discussed in the reported reference documents. However, in the relevant literature, PPTs have been usually classified either by their electrode geometry or by the way their propellant is stored and feeds the thruster. Both criteria are presented and briefly discussed in the following sections.

Table 2-1 – PPTs main classification

Classification	Class/Type	Reference documents
Electrodes geometry	Parallel Plate	[1], [29], [30], [31]
	Coaxial	[19], [20]
	Linear or Z-Pinch	[32]
	Inverse Pinch	[33]
Propellant state	Solid propellant	[7], [29], [30], [31], [34], [35], [3]
	Gas-fed	[19]
	Liquid propellant	[36], [37] [38]
Propellant feeding system	Side-fed	[35], [3]
	Breech-fed	[1], [34]
Ignition method	Spark plug	[7], [29], [30], [31], [34], [35], [3]
	Laser	[24]

2.1.2.1. Classification by electrode shape

The electrode geometry classification criterion leads to the four possible PPTs classes:

- Parallel Plate PPTs
- Coaxial PPTs
- Linear or Z-Pinch PPTs
- Inverse Pinch PPTs

Rectangular parallel plate electrodes represent the simplest possible PPT electrode configuration (shown in Figure 2-1). However, among the thrusters with plane electrodes, it is quite common to find flared electrodes configuration, as shown in Figure 2-4, or, more recently, tongue shaped electrodes [34].

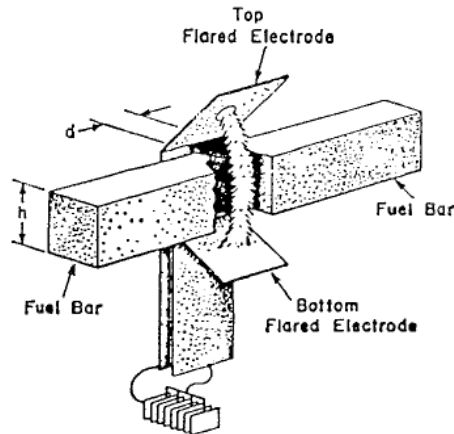


Figure 2-4 – Flared electrodes PPT [39].

In coaxial electrodes PPTs, the outer electrode, which can be either the anode or the cathode, can be straight (cylindrical shape) or might present a divergence angle (truncated-conical shape, as shown in Figure 2-5). Once the discharge is triggered, it assumes the structure of an annular sheet. The self-induced magnetic field has therefore an azimuthal shape encircling the central electrode. Since there is no magnetic flux outside the thruster, field distortions due to presence of edges, which characterize the parallel electrode configuration, are avoided. The drawback of the coaxial configuration is that both discharge current density and the magnetic field are not uniform and vary with $1/r$, where r is the radial position inside the thruster. Consequently the Lorentz force is proportional to $1/r^2$. It has been conjectured (and to the best knowledge of the author still not proven) that this is one of the possible reasons why this configuration is strongly characterized by phenomena such as plume divergence, radial current instability and loss of orthogonality between current arc and electrodes [20].

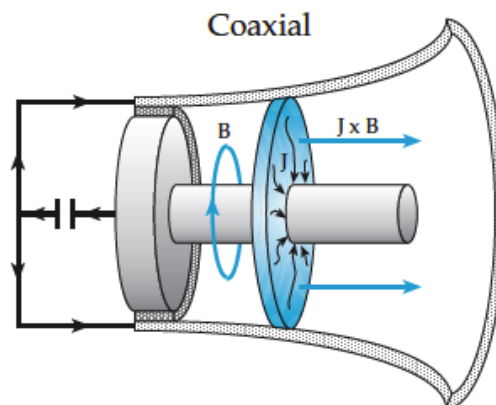


Figure 2-5 - Coaxial PPT with divergent outer electrode [19].

For what concerns the linear (or Z-Pinch) PPTs and the inverse-pinch PPTs, design and operation of this kind of thrusters are conceptual very simple: two disc-shaped electrodes are separated by insulating walls and linked to a capacitor or a more generic energy-storing device (Figure 2-6). As the coaxial electrode configuration,

an azimuthal magnetic field is generated, whose flux is completely confined inside the thruster. In this kind of PPTs, the interaction between the current and the self-induced magnetic field accelerates the arc in the radial direction: the plasma is “pinched” towards the centre of the thruster [32], [33].

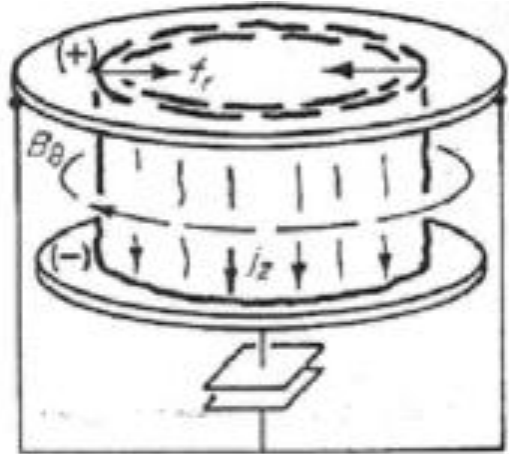


Figure 2-6 – Z-pinch PPT concept [20].

Once an orifice in one of the electrodes is introduced, the propellant, which is initially radially accelerated, encounters a strong axial pressure gradient. Thus the plasma is expelled in this direction, generating thrust. The configuration is called “linear” or “Z-pinch” if the arc is accelerated toward the centre of the thruster. Otherwise when the arc is accelerated from the thruster axis towards the end of the thruster itself, the configuration is called “inverse pinch” (Figure 2-7).

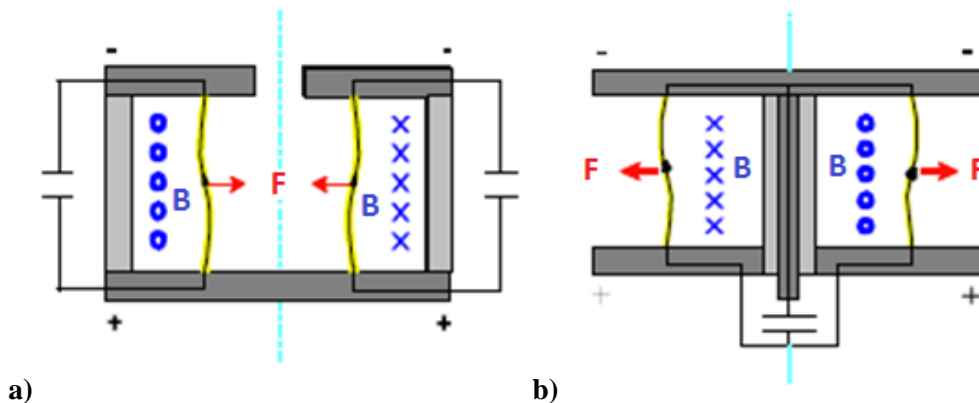


Figure 2-7 - PPT working principles: a) Z-pinch, b) Inverse pinch.

2.1.2.2. Classification by propellant feeding system

The propellant feeding system classification criterion leads to the three possible PPTs classes:

- Solid propellant, also known as Ablative PPTs (A-PPTs),
- Gas-fed PPTs (GF-PPTs),
- Liquid propellant PPTs (LP-PPTs).

Solid propellant PPTs are extremely versatile, reliable and have accumulated a significant flight experience in the last fifty years. They have some characteristics that make them particularly attractive compared to the other solutions (e.g. cold-gas thrusters) [40]. A-PPTs do not require valves, tanks and moving parts and this means ease of integration on a spacecraft. Moreover the propellant is stable, easy to storage and it is not characterized by any leak, even during long period of inactivity. Fluid propellant PPTs (both GF-PPTs and LP-PPTs) have some advantages that may make them preferable to the A-PPTs [19], [40]. Their main advantage is the better throttling capability, because during each shot the propellant mass is injected in the discharge chamber by suitable valves. Therefore, the mass bit is independent on the discharge current, which leads to a wider range of achievable specific impulses. Moreover the performances of these PPTs are more repeatable due to the absence of propellant ablation irregularities which may cause shot to shot variations [40]. At last, as mentioned in §2.1.1, the discharge ignition can be achieved at lower voltages. However these thrusters require pipes and tanks to store the propellant, which is usually xenon, argon or water vapour for the GF-PPTs [19], [41] and water for the LP-PPTs [36], [37], [38]. Finally, it is necessary to use fast operating and reliable valves to limit the waste of propellant between two consecutive shots and that have to be designed along with the thruster itself.

2.2. Solid propellant PPTs

In the next section a detailed review of the solid propellant A-PPTs is presented, pointing out the typical performances reported in the literature and the major problems that affect their lifetime.

2.2.1. PPTs performance review

Ablative PPTs (forward from this point simply named as PPTs) use the energy provided by the discharge between the electrodes, which is initially stored into the main capacitor bank, to ablate the surface of one or more solid propellant bars. The propellant particles are then dissociated and ionized, thus forming a thin plasma sheet accelerated by the Lorentz force.

The position and the geometry of the propellant bars is used to divide the PPTs into two groups [1]: breech-fed PPTs, constituted by PPTs having a single propellant bar at the thruster breech (Figure 2-8) and side-fed PPTs, constituted by the PPTs having two or more propellant bars advancing from a direction perpendicular to the plasma flow and thrust direction, in a position close to the thruster breech where the discharge is initially focused. Side-fed PPTs can be also divided into two sub-groups: the variant characterized by the surfaces of the propellant bars exposed to the main discharge parallel to the thrust vector (Figure 2-9) and the variant characterized by the surfaces of propellant bars that form an angle with the thrust vector (Figure 2-10). The former configuration is called side-fed, whereas the second one is also known as V-shape configuration.

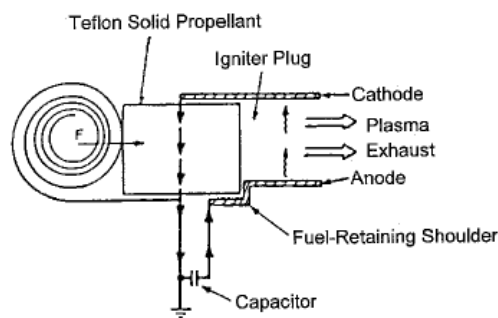


Figure 2-8 – Breech-fed PPT [1].

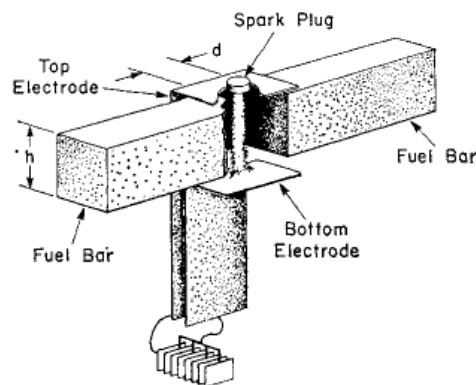


Figure 2-9 – Side-fed PPT [39].

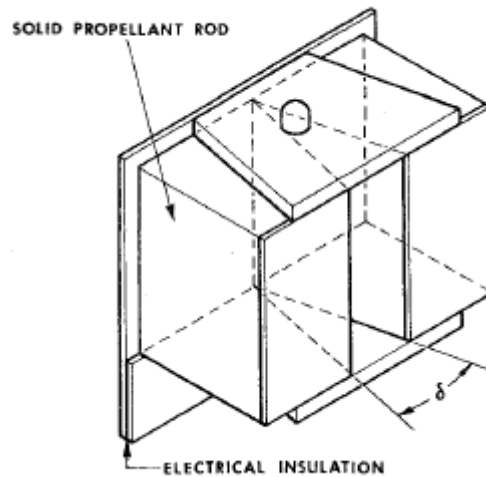


Figure 2-10 – V-fed PPT [42].

It is clear that the position of the propellant bars strongly affects the PPT operation. In the breech-fed thrusters the propellant can be ablated only at the very beginning of the discharge, when the current sheet is close to the breech, whereas in the side-fed or V-fed PPTs the discharge keeps ablating the propellant bar for some time while being accelerated downstream and the exposed propellant surfaces are a relevant part of the PPT lateral walls.

Ablative PPTs are characterised by a quite high specific impulse I_{sp} (between 300 s and 2000 s) [1], operating in a mean power range of 1-300 W [43]. More inherent to the miniaturized satellites applications, low power ablative PPTs (of the order of few W) have been successfully designed and even flown in the past [44], [45], [46], [47], [48], [49]. The impulse bit (I_{bit}), i.e. the impulse provided by the thruster per shot, has been found to be directly proportional to the discharge energy (E_0) [1], [12], [13], [20], [39], [42].

A very useful correlation found by Gessini and Paccani [43] for a PPT preliminary design is the one between the I_{sp} and the ratio E_0/A , where A is the area of the propellant exposed to the main discharge. The correlations depend on the feeding configuration and the expressions are reported below.

$$I_{sp}|_{\text{breech-fed}} = 247 \left(\frac{E_0}{A} \right)^{0.87} \quad (2)$$

$$I_{sp}|_{\text{side-fed}} = 504 \left(\frac{E_0}{A} \right)^{0.40} \quad (3)$$

Previous experimental test campaigns on PPTs proved that the gasdynamic contribution to thrust can be a very significant fraction of the total thrust (up to 25% - 50%) [42], [50], [4].

The propellant bars are made of a dielectric material, usually polytetrafluoroethylene (PTFE): this material proved to be the most suitable for this application. Tests have been performed using polyethylene, acrylic plastics [27] and other thermoplastic materials (such as Celcon, Halar, Halon and Tefzel) as propellants [1], [42]. However the performance does not increase. Only carbon impregnated Teflon causes a slight improvement in the performance, compared to pure Teflon, while porous Teflon proved to be ineffective [50].

Moreover, the mass bit (m_{bit}), i.e. the propellant mass ablated per shot, has been also found to be proportional to the discharge energy. The mass bit to the stored energy ratio usually assumes values in the 1-10 $\mu\text{g}/\text{J}$ range [1], [42], [4].

The most important flaw of the PPTs is their overall efficiency (η_{th}), i.e. the ratio of the propellant axial kinetic energy to the energy stored in the capacitor, that is usually very low, in a range between 1 and 35 % [35]. This is particularly true for low energy thrusters with the exception of some very advanced PPTs developed by the research Institute of Applied Mechanics and Electrodynamics of the Moscow Aviation Institute (RIAME MAI) [27], [28], as shown in Figure 2-11.

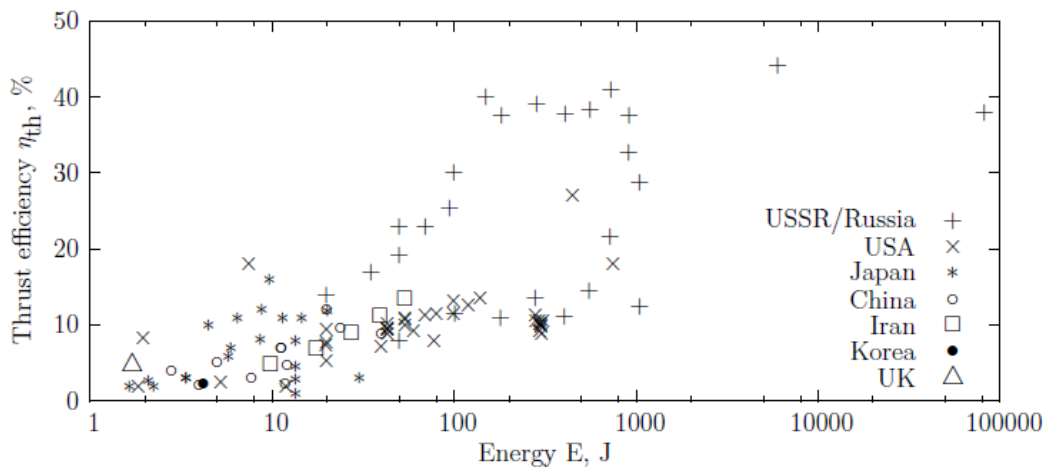


Figure 2-11 - Thrust efficiency against stored energy for different PPT [35].

One of the most important causes for the low efficiency levels is the bad utilization of the propellant, mainly due to a process called late time ablation (LTA). It happens when the decomposition of the propellant bar surface does not terminate at the same time of the discharge (usually few μs) and lasts up to 300 μs [51], [52], [53], [54], [55], [56], [57]. It means that some of the energy is wasted ablating propellant that is not electromagnetically accelerated and slowly leaks out of the thruster, hence decreasing the I_{sp} and the η_{th} .

Table 2-2 summarizes the most important PPT characteristics discussed above.

Table 2-2 – Typical PPT range of characteristics

Parameter	Value
E_0	1 - 100 J
I_{bit}	10 - 1000 μ Ns
I_{bit}/E_0	~16 μ Ns/J (breach-fed) ~23 μ Ns/J (side-fed)
m_{bit}/E_0	1 - 10 μ g/J
I_{sp}	300 - 2000 s
η_{th}	1 - 30 %
Propellant material	PTFE

2.2.2. Lifetime limiting factors

The carbonization of the discharge chamber is one of the most important phenomena that characterize all the ablative PPTs and it is conventionally indicated as the main life limiting mechanism for those kinds of thrusters [1], [20]. Its main effect is the deposition of a thin layer of carbon on the discharge chamber walls that could eventually create a conducting path between the two electrodes, which finally shorts the electrodes causing a definitive thruster failure. The carbonization is due to the expansion of the plume generated by the main discharge that hits the discharge chamber inner surfaces. During this process, carbon that comes from the PTFE propellant bars is deposited.

Moreover, the optimization of the spark plug system represents another important issue to be solved to increase the PPT life and the reliability of the propulsion system. The spark plug has to be reliable and to work during the whole PPT lifetime. Indeed a failure in the trigger system may be fatal for the whole propulsion system. In this section the most relevant studies and results about carbonization and spark plug reliability are presented in detail.

2.2.2.1. Carbonization issue

PPTs were designed and successfully tested at RIAME MAI from 1975 to 1989. During that period, studies were oriented to the development of innovative thruster concepts, selection of new designs and technological solutions to increase the reliability of the thrusters, hence reducing the effects of the carbonization [29], [30], [31], [58].

RIAME MAI's PPT differs from previous PPT designs by using an end insulator which has a concave cylindrical form, forming a "forechamber" or pre-combustion chamber. According to [29], the depth of this forechamber is approximately $3/2$ of the channel width. Moreover, as shown in Figure 2-12, the spark plug is mounted near the rear surface of the forechamber normal to the cathode axis.

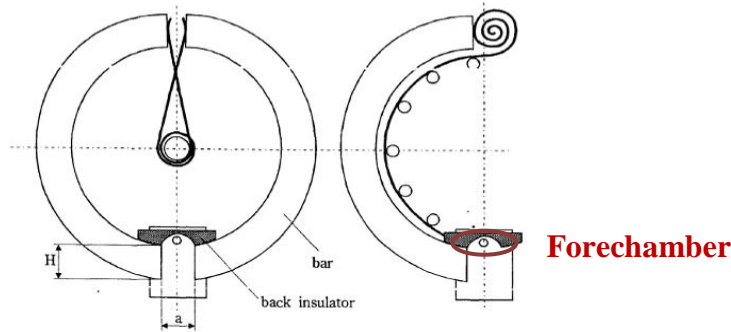


Figure 2-12 - Main discharge chamber and "forechamber" proposed by RIAME MAI [29].

Additionally grooves were included in the design of the walls to reduce the chance of electrode short-circuiting due to carbonization. It is reported [58] that two circular grooves with the width of 1.5 mm and depth of 3 mm were included on the outer cylindrical surfaces of the propellant bars to eliminate electrical self-breakdowns along the outer surface in the electrodes area. The final PPT arrangement is shown in Figure 2-13.

The results of the tests conducted at RIAME MAI indicated [29], [30], [31]:

- good uniformity of PTFE evaporation from the propellant working surfaces;
- carbon film growth stopped after about 10^4 shots (at the forechamber walls);
- absence of electrode erosion effects inside the channel. However, the electrodes were covered by a dense carbon film;
- weak cathode erosion at the channel exit.



Figure 2-13 – RIAME MAI PPT arrangement [29]. Note the grooves on the lateral walls.

In Japan the Tokyo Metropolitan Institute of Technology (TMIT) developed a breech-fed PPT for the μ -Lab Sat II [47]. From the beginning of the thruster

characterization, carbonization was observed and the thruster failed to work after about 110,000 discharge pulses. By lowering the discharge area (from 5 cm^2 to 0.5 cm^2) and increasing the energy density (from 0.5 J/cm^2 to 7.2 J/cm^2), the carbonization and non-uniform PTFE ablation problem were solved as reported in [48] and shown in Figure 2-14.

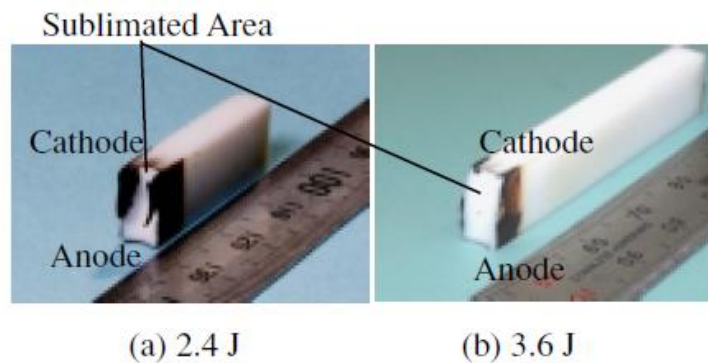


Figure 2-14 - Propellant bars sublimation condition after 100,000 shots at different E_0 [48].

In England the University of Southampton (UoS) developed a side-fed PPT called PPTCUP-BB [4]. This thruster was affected by a relevant carbon deposition on the discharge chamber walls, especially on the edges, after only 1000 shots. Different authors in their studies [39], [59] affirm that the energy level (2.3 J) and the energy over propellant area ratio (2.13 J/cm^2) selected for the PPTCUP-BB test campaign should assure the thruster not to be affected by severe carbonization of the propellant and the discharge chamber walls. Due to this inconsistency, it was decided to verify the total amount of energy stored in the capacitor bank. It was found that the capacitors were affected by a significant capacitance de-rating at high voltages and consequently the actual initial stored energy was about 20% smaller than the expected value of 2.3 J.

The experiences from TMIT and UoS suggest that increasing the initial energy and/or the energy over propellant area ratio limits the effect of the carbonization.

2.2.2.2. Spark plug system

The spark plug is one of the most critical components in a PPT since it has the function of triggering the main discharge. The voltage needed to ignite the discharge between the spark plug and the ground electrodes depends on the breakdown electric field of the insulator used to separate the two electrodes.

In the PPTCUP designed and developed by the UoS, PTFE was chosen as insulator in the spark plug system and the voltage need to trigger the spark plug was in the range between 6 kV and 9 kV [4], [3].

In the ADD SIMP-LEX PPT designed and developed by the University of Stuttgart, the main discharge was triggered by a Unison 9044635-1 semiconductor spark plug

[35], able to operate in a range between 1 and 10 kV. However, the dimensions of this kind of semiconductor spark plug (of the order of several cm as shown in Figure 2-15) are way too big for the miniaturized satellite applications.

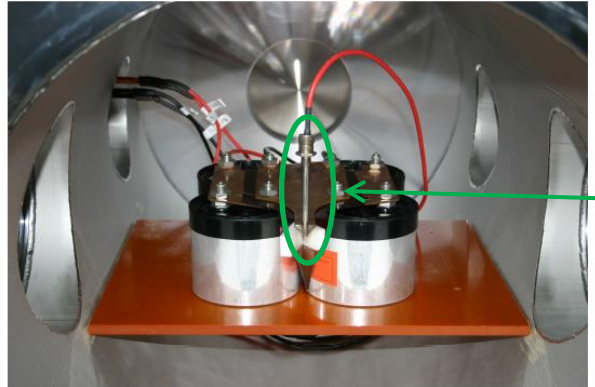


Figure 2-15 – ADD SIMP-LEX [35].

It is clear that many benefits would be obtained from a reduction of the spark plug breakdown voltage (ideally with a voltage equal or lower to the one at which the main capacitor bank is charged) in term of:

- lower overvoltage on the capacitor bank during the trigger discharge, that could reduce the possibility of failures or damages of the single capacitors;
- lighter and more reliable control electronics, i.e. only one high voltage power supply could be used to charge the main capacitor bank and to trigger discharge;
- better reliability of the entire propulsion system, which is essential to increase the lifetime.

The most common technique for lowering the breakdown voltage, hence improving the spark plug performance, is to coat the insulator with a thin layer of a different material, as shown in Figure 2-16.

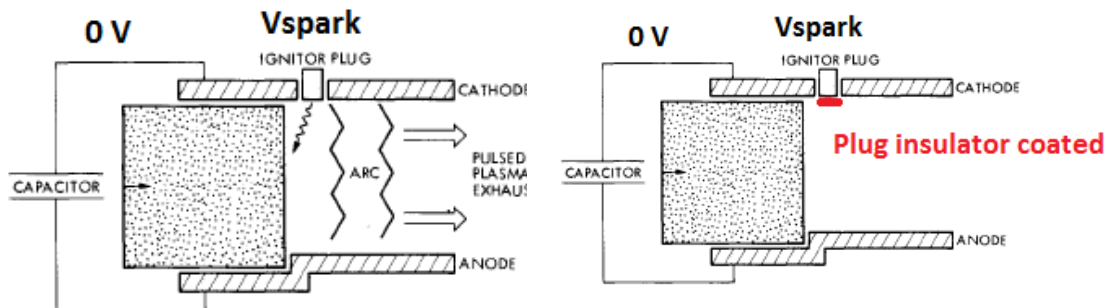


Figure 2-16 – Spark plug coating concept.

Boxman et al. [60] affirms that inorganic ceramics coatings could improve the flashover and suggests using a layer of Titanium hydride, because it easily releases

gas and allows triggering at lower power. On the other hand, in the late 70's, Miller et al. [61] performed some tests on vacuum diodes made of Alumina coated with Mn-Ti alloy (7:1 ratio). The results demonstrated that the coating decreases the alumina resistivity and that the combination of material allows the coating to penetrate uniformly inside the insulator, increasing the expected lifetime, because the insulator is more insensitive to be damaged by abrasion or electrical breakdown.

Despite this possible choice of material to deposit (inorganic ceramics), many of the PPTs tested in the past have used semiconductor spark plugs that have been reported to work with voltages as low as 1kV, as affirmed by different authors in their studies [8], [19], [62], [63].

Unfortunately in the literature the semiconductor used in these spark plugs is never clearly identified nor is the company that was manufacturing them. Nevertheless, Vondra et al. [8] affirmed that to obtain a discharge in vacuum the semiconductor it was necessary to liberate electrons as results of the strong electric fields present and that the spark could be generated with an applied voltage of about 700 V. As shown in Figure 2-17, the spark plug was about 25 mm long, hence, too big for PPT for miniaturized satellite applications. It was made by the Bendix Corporation and consisted of an outer electrode of Inconel separated by a concentric ring of semiconductor material (the author did not specify the material) from the inner electrode, also made of Inconel.

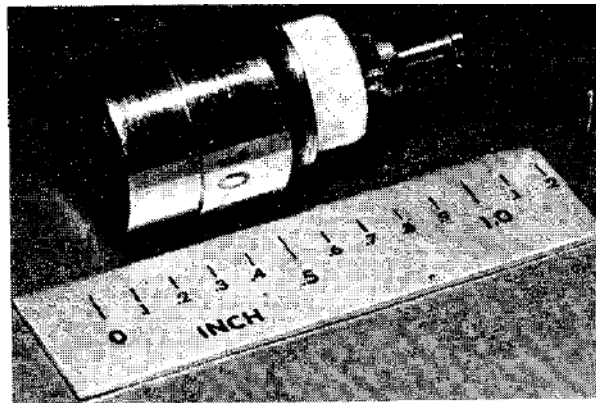


Figure 2-17 - Example of spark plug made by the Bendix Corporation [8].

These kinds of spark plugs were successfully used up to the year 2001 [19]. Unfortunately between 1970 and 1990 the Bendix Corporation went through a series of mergers, sales and changes with partners or buyers [64] up to the point where it is now impossible to find out how those spark plugs were made or (even more unlikely) get some spark plugs manufactured.

In [63] a low-voltage or *triggerless* vacuum arc initiation is described. It consists of the generation of a low-voltage and high current discharge between two electrodes and it is characterized by an inter-electrode metal plasma. This kind of plasma is generated from a layer of conductive material, which is usually a metal, deposited on the insulator between the electrodes. The mechanism of plasma production is based

on an explosive destruction of the layer-cathode interface caused by the Joule heating. The thin conductive layer produces high but finite impedance between the two electrodes (in theory, using a perfect insulator the impedance can be assumed infinite). Once a relatively low voltage of the order of some hundreds of volts is applied between the electrodes, breakdown occurs in the small gaps or flaws of the thin metal film. These small discharges produce enough metal vapour to initiate the main discharge [65].

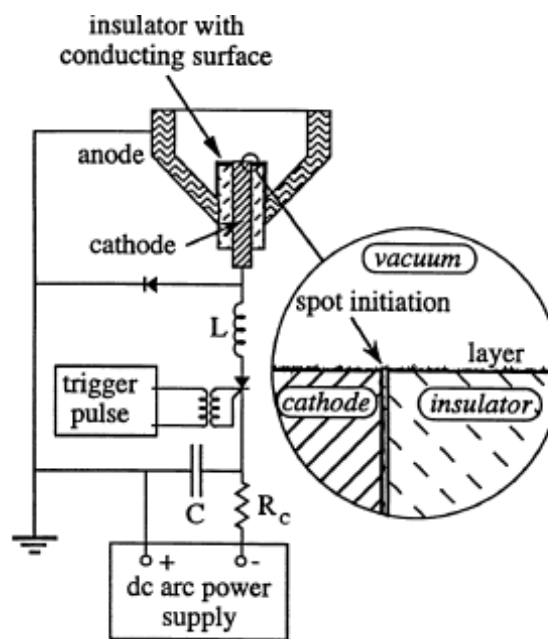


Figure 2-18 – Scheme of a *triggerless* vacuum arc [63].

This solution is commonly used to generate the main discharge of another kind of pulse thrusters, named Vacuum Arc Thruster (VAT) [66]. In theory, it can be also applied to the PPT spark plugs, coating the spark plug insulator with a thin layer of metal, and benefits could potentially ensue. Indeed, this coating should allow initiating the spark plug discharge at lower voltages thanks to the *triggerless* process and it is intrinsically scalable and hence applicable to small spark plug insulators that are suitable for PPTs for miniaturized satellite. However, since in a VAT the propellant is typically the cathode [65], [66], [67], the metal vapour and droplets eroded from the electrode replace the thin conductive layer on the insulator [65] hence assuring that this triggering system is able to perform more than one million shots [63].

2.2.3. Spark plug insulator

To increase the lifetime and optimize the performance of a PPT for microsatellite applications, it is necessary to find the best spark plug insulator configuration that can withstand the PPT lifetime requirements and can reduce the spark plug breakdown voltage.

These two requirements define the way the choice of best configuration should be carried out. To match the lifetime requirement is an absolute because a failure in the spark plug system causes the failure of the whole propulsion system; indeed it represents the first criterion of choice of the spark plug configuration.

The second requirement, i.e. the reduction of the spark plug breakdown, is the figure of merit of a certain spark plug configuration, which already proved its lifetime. The less the breakdown voltage is, the better that spark plug configuration is.

Considering the previous works on spark plugs reported in §2.2.2.2, there are three possible solutions that can be adopted to reduce the breakdown voltage of a spark plug:

- To deposit a semiconductor layer [1], [8], [35], [29], [62];
- To deposit inorganic ceramics [60], [61].
- To deposit a metal [59], [63].

Among these options it has been decided to focus the research mainly on the spark plug insulators coated with a layer of a semiconductor or a layer of metal.

The first choice is justified by the fact that most of the examples of PPT coated spark plugs found in the relevant literature have used semiconductors material. The latter is justified by the fact that spark plug insulators coated by metal have been successfully used in other miniaturized thrusters (i.e. VATs) and proved to withstand more than one million shots [63], which is the same order of magnitude of the number of shot that a PPT has to perform during its lifetime [68]. On the other hand, the deposition of inorganic ceramics has been discarded because it has never been used to produce any spark plug insulators used to trigger the PPT main discharge.

2.2.3.1. Semiconductor coating selection

Due to the lack of information in the PPT relevant literature, papers from other disciplines, e.g. electronics and solid state physics, have been read and studied to choose the best semiconductor to deposit on a spark plug insulator.

In nature there are different kinds of semiconductor materials. They can be elements, e.g. germanium (Ge), silicon (Si), carbon (C), tellurium (Te) and selenium (Se), or they can be compounds, e.g. the indium compounds (InSb, InAs and InP), the gallium compounds (GaSb, GaAs, and GaP) and the lead compounds (PbS, PbSe and PbTe) [69].

Another important aspect that have to be taken into account is the technique and hence the tool to use for the deposition. Considering the typical dimensions of the

spark plug insulator surface ($\approx 1 \text{ mm}^2$ [68], [70]) where the semiconductor should be deposited, it is possible to use the RF glow discharge method that guarantees a homogenous deposition of the material. The RF glow discharge is a plasma-enhanced chemical vapour deposition (PECVD) technique [71]. This process is used to deposit thin films from the interaction between a plasma plume generated by reacting gases, which contain the semiconductor to deposit, and a solid state on a substrate that is the spark plug insulator rod itself in our case. The plasma is created by RF frequency between two electrodes, the space between which is filled with the reacting gases. Note that this deposition technique is very common to coat substrates with amorphous semiconductor thin films, which are widely used in variety of application such as thin film transistors, solar cells and imaging devices [72], [73].

The deposition machine that has been used in this project is in the clean room of the Electronic and Computer Science Faculty in the UoS. This reduced the costs of the deposition process and at the same time guaranteed an excellent sample treatment, having the clean room and the machine itself an elevate standard of quality [74]. This tool can be used to deposit a layer that has a thickness of the order of some micrometres hence matching the dimensions suggested in [59], [63].

Considering the capability of this machine, only Ge, Si and C can be deposited in their amorphous state. Among these three options, C cannot be selected because its deposition in the graphite form requires a very high temperature (more than 1200 K, as reported in [75]) that could melt the spark plug insulator.

On the other hand, the deposition of the Ge and the Si can be done at lower temperature ($< 600 \text{ K}$). Moreover, these two materials have been deeply studied since the early 60s for the development of devices such as transistors, solar panels and amplifiers [72], [73].

Samples are produced using a mixture of germane (GeH_4) or silane (SiH_4), diluted in hydrogen (H_2) [71], [73]. Therefore, using the PECVD technique, hydrogenated amorphous germanium (a-Ge:H) and silicon (a-Si:H) can be deposited on the PPT spark plug insulator.

Mechanical and electrical properties of thin semiconductor films (i.e. films with a thickness $< 10 \text{ }\mu\text{m}$) have been deeply investigated in the past for their use in miniaturized electronic devices. For the a-Ge:H layers, interesting results in terms of thermal expansion coefficient and elastic modulus are reported in [72], [76] and [77]; whereas for the a-Si:H layers, data can be found in [77] and [78]. However, considering the objective of this research, the study was mainly focused on the electrical characteristics of the hydrogenated amorphous semiconductor layers. As reported in the relevant literature ([76], [79] and [80] for the germanium layers and [77], [78] and [81] for the silicon layers), the amorphous-state semiconductors are characterized by an electrical resistivity significantly influenced by the operating temperature and by the thermal history of the samples. Figure 2-19 shows how the resistivity of an a-Si:H, measured in vacuum, changes with the operative temperature

(as expected it decreases if the temperature increases) and for the effects of the annealing. Note that from the diagram the effect of the final admitting of air is very small if compare to the annealing effects.

Another important aspect, which is related to the possible application of these layers in the PPT spark plugs, is little voltage frequency dependence of the amorphous resistivity. Figure 2-24 shows that the AC resistivity of an a:Ge-H decreases with the frequency above a minimum frequency [79]. It is clear that this is an important property to take into account for pulsed discharge applications.

At last, it has to be noticed that if the temperature is high enough, a transformation from an amorphous to a polycrystalline state occurs and the electrical properties may significantly change. During this transformation, randomly distributed nucleation centres appear on the layer and then grow (Figure 2-21). The transaction temperature for the a:Ge:H is about 720 K, whereas for the a:Si:H it is about 900 K [78], [79].

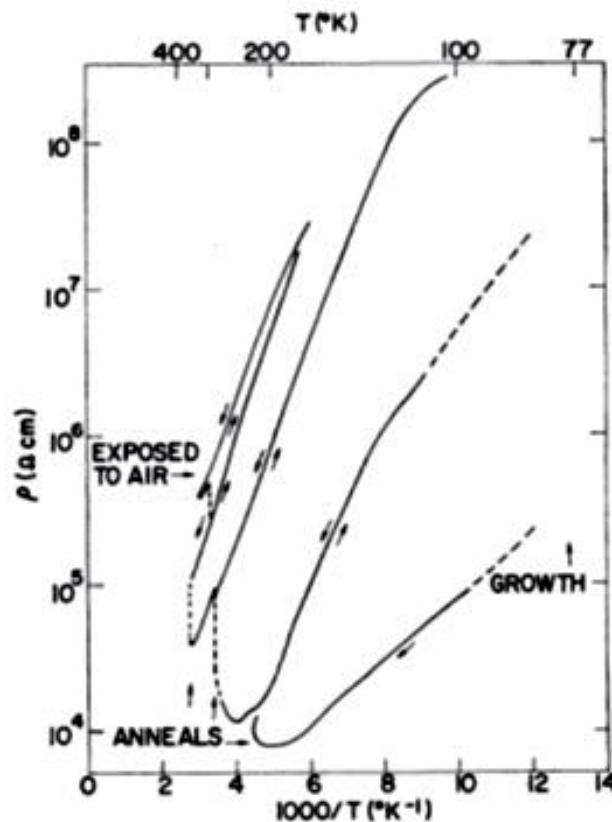


Figure 2-19 – Resistivity of an a-Si:H layer grown and measured in vacuum [78].

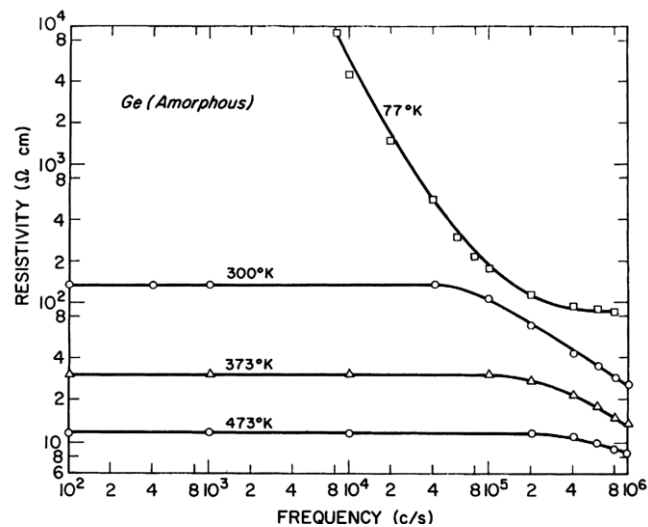


Figure 2-20 – AC resistivity of an a-Ge:H layer as function of the voltage frequency [79].

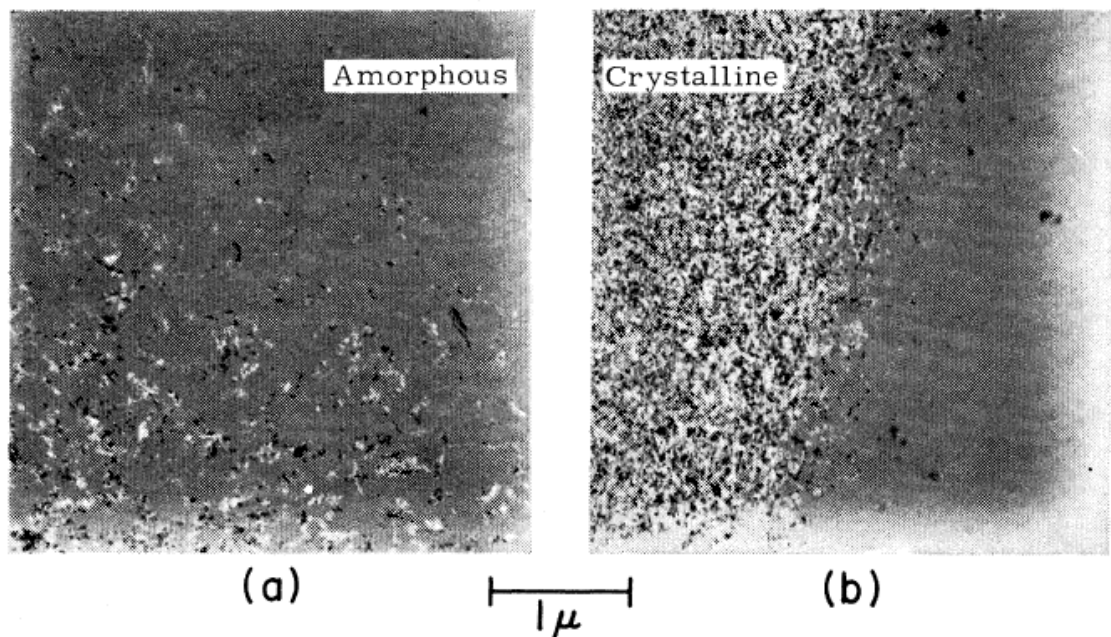


Figure 2-21 – Amorphous-crystalline transaction (Ge layer). Note the growth of the nucleation centres [79]

2.2.3.2. Metal coating selection

Spark plug insulators coated by metal have been successfully used in the VATs showing a lifetime similar to the one required for PPT applications. To trigger the VAT main discharge, the thin metal layer has to have an equivalent resistance in the range between 1 and 1000 Ω [59], [63], [65], [66], [67], [82]. For what concerns the metal coating in PPT applications, this defines the range of metal layer thickness, once the geometry of the spark plug insulator and the metal to deposit are known.

The deposition technique of a thin metal layer is based on the thermal evaporation of the metal to deposit. In principle, the thermal evaporation technique is a simple process in which condensed or powder source material is vaporized at an elevated temperature. Then its vapour phase condenses under suitable environmental conditions to form the final product [83].

As for the tool chosen for the semiconductor coating (§2.2.3.1), the deposition machine that have been used in this project is in the clean room of the Electronic and Computer Science Faculty of the UoS.

Considering the capability of this tool, titanium (Ti), aluminium (Al) and gold (Au) can be chosen. As reported in [63], low-melting point materials (e.g. Pb) are characterized by a large droplet erosion rate and the droplets tend to produce a conducting film on the insulator, thus shorting the electrodes. For this reason, Al has been discarded because it has the lowest melting temperature among the three available materials (about 900 K against about 1400 K for gold and almost 2000 K for titanium).

2.2.4. Electromagnetic noise

Even if all the problems related to the PPT lifetime were to be solved, a potential issue to be addressed for flight opportunities is the electromagnetic compatibility (EMC) of the PPT with the spacecraft. As mentioned in §2.1, PPTs have had a successful flight history, but it has been difficult for the spacecraft integrators to evaluate the real risk of potential electromagnetic interference (EMI).

The Zond-2 mission (URSS, satellite launched in 1964) was considered a success and the fact that no mention was made about EMI indicates that there were not significant EMI issues.

More interesting results were found during the LES-6 and LES-7/8 development [84], [85], [86] (USA, developed between 1960s and early 1970s), because the first EMI practical acceptance criteria were defined. The acceptable noise pulse should be less than the receiver saturation level and the pulse duration less than a selected value to avoid interruptions in the communication link [84].

Figure 2-22 shows another interesting aspect that was found during the system qualification [85]. The radiation intensity departs from zero about 300 ns before the main discharge and reaches the peak about 100 ns before the main discharge starts. This indicates that the radiation is not generated by the main discharge.

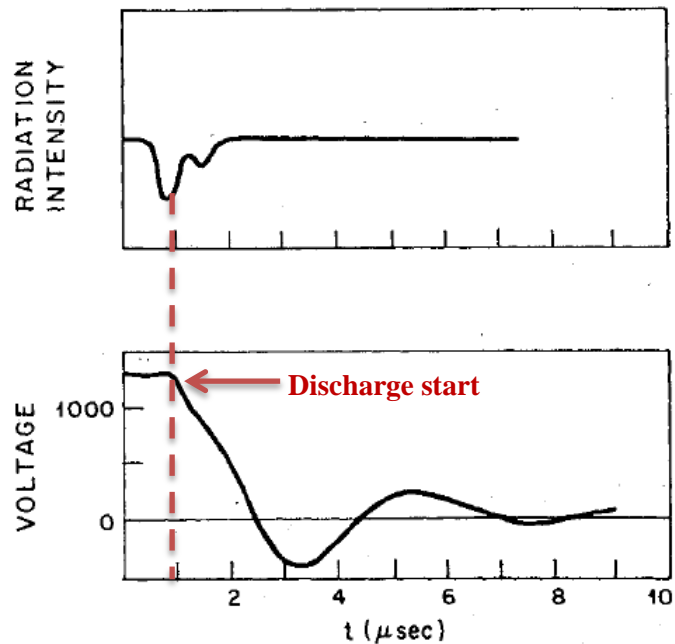


Figure 2-22 – Radiated signal (top) and capacitor voltage discharge (bottom) [85].

In the recent past (1995-2000), the EO-1 PPT has been developed, built and launched in November 2000 [87]. The unit underwent an extensive ground testing associated with EMI. Tests were performed according to the MIL-STD-461C and MIL-STD-462C and included conducted and radiated emissions. The unit was often compliant with the conducted emission limits or above the limit by a maximum value of 15 dB. Similar results have been found for the radiated magnetic field [87]. The most interesting results were found for the radiated electric field. The emissions radiated by the first version of PPT always exceeded the limits (the maximum difference is about 80 dB at 1 MHz) that were already increased by 10 dB above the one suggested in the MIL-STD-461C. To reduce such level of emissions, the unit was enclosed in six-sided aluminium cover box and the test repeated. Using the shielding box, the level of radiated electric field exceeded the limit only between about 3 and 30 MHz and by a maximum of 20 dB. Figure 2-23 shows the comparison of the test results obtained with and without the shielding box [88].

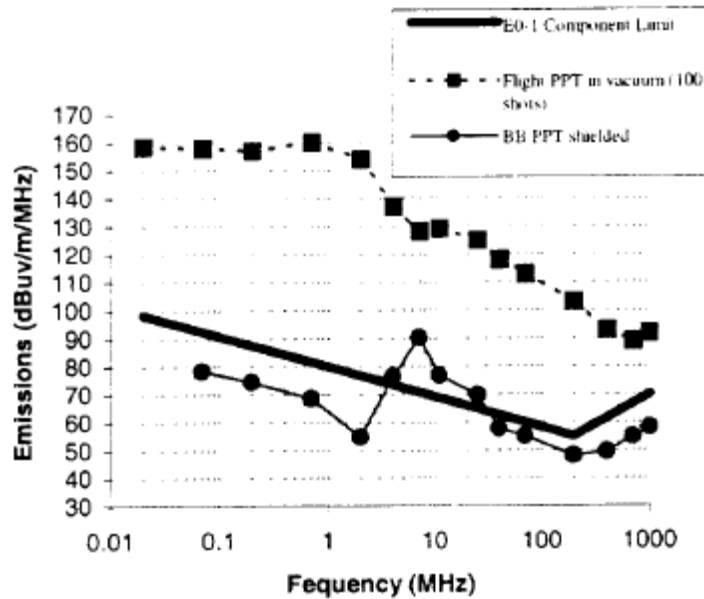


Figure 2-23 – EO-1 PPT radiate electric field test results [88]. The solid line is the limit set for the unit, the square and the circle markers indicate the results obtained respectively without and with the additional shield envelope

In 2005, the University of Washington (USA) developed a PPT propulsion system for the Dawgstar satellite. The system underwent an EMC characterization test; however only the coupling of the radiated noise to the flight model GPS patch (center frequency = 1.58 GHz) and to the cross-link antennas (center frequency = 2.01 GHz) were measured [44].

Given these past experiences, it can be affirmed that the short and high intensity pulses that characterize a PPT do not conform to the standard EMI evaluation criteria (e.g. MIL-STD-461C). This is mainly due to the fact that no good way has been found to relate measurements of large electric and magnetic fields for extremely short duty cycles to the risk of possible failures of the nearby circuits [87], [88]. Therefore, difference approaches were considered for the EMI evaluation. The thruster should not interfere with the communications and only the emissions in band of the frequencies used for the communication link are investigated [44], [85]. Finally, it has been found that to shield a PPT with a metal cover significantly reduces the radiated emission [88].

2.3. Performance models

In the relevant literature, it is generally accepted that the discharge potential evolution of a PPT can be described in first approximation with a circuit model wherein the plasma sheet is represented by discrete and time-varying elements of an RLC series circuit [19], [20], [35], [89]. As shown in Figure 2-24, this circuit model

comprises other constant elements that represent the other components of the PPT, i.e. the capacitor bank the electrodes and the line in between them.

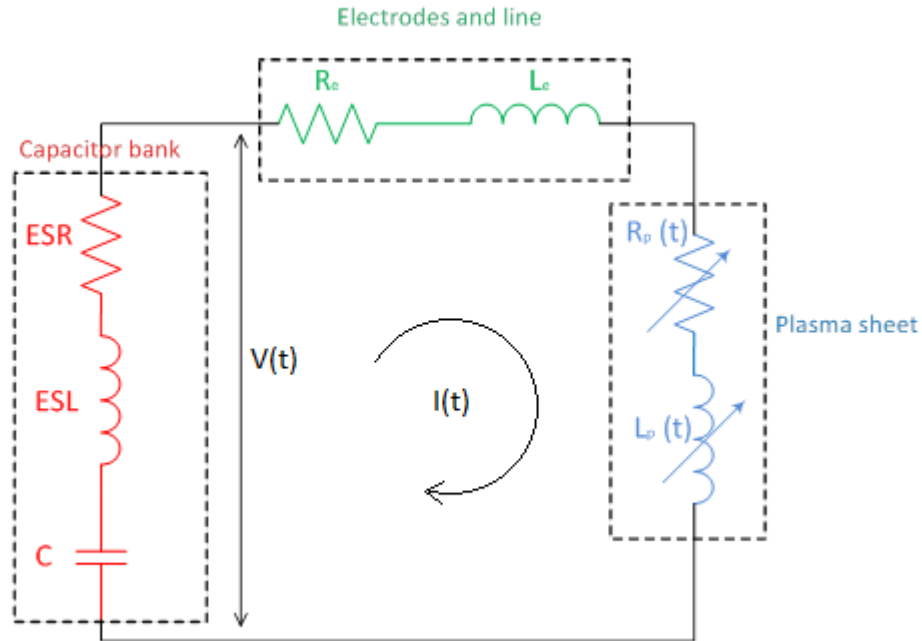


Figure 2-24 – PPT RLC circuit model

The capacitor bank is modeled with a constant capacitive element (C), in series with an inductive and a resistive constant element, named equivalent series inductance (ESL) and resistance (ESR). The electrodes and the transmission are represented with an inductive and a resistive constant element (L_e and R_e). The time variance of the plasma parameters R_p and L_p is introduced to model the changing inductance and resistance of the discharge circuit as the current sheet propagates down the electrodes, accelerated by the Lorentz force. The equation describing the discharge potential is then coupled to the momentum equation of the plasma sheet, thus reflecting the interaction between dynamic and electric characteristics of the discharge. The discharge dynamics of a PPT can be represented by a simultaneous system of the circuit discharge equation and the plasma sheet momentum equation. In this section the two equations will be derived and the system presented, together with some important parameter definitions which are useful for the characterization of the PPT performances. Note that in Figure 2-24 it is also introduced the definition of discharge voltage $V(t)$ and current $I(t)$, usually measured during the PPT operation.

2.3.1. Conservation of charge equation

Applying Kirchhoff's second law to the circuit in Figure 2-24, $V(t)$ can be expressed as:

$$V(t) = [L_e + L_p(t)] \cdot \frac{dI(t)}{dt} + \left[R_e + R_p(t) + \frac{dL_p(t)}{dt} \right] \cdot I(t) \quad (4)$$

or alternatively as:

$$V(t) = V_0 - \frac{1}{C} \cdot \int_0^t I(\tau) d\tau - ESR \cdot I(t) - ESL \cdot \frac{dI(t)}{dt} \quad (5)$$

where V_0 is the initial voltage applied to the capacitor bank.

Considering the circuit in Figure 2-24, it is possible to define the following parameters without loss of generality:

$$R(t) = ESR + R_e + R_p(t) \quad (6)$$

$$L(t) = ESL + L_e + L_p(t) \quad (7)$$

The new equivalent circuit is shown in Figure 2-25.

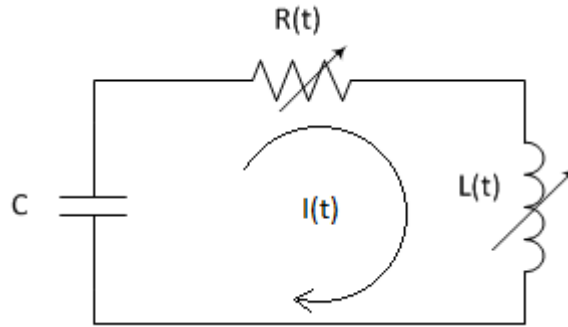


Figure 2-25 – PPT equivalent RCL circuit

As mentioned above, R_p and L_p have been introduced to take into account the variation of the circuit inductance and resistance due to the acceleration of the plasma sheet downstream.

As shown in Figure 2-26, if $x(t)$ is the plasma sheet position along the electrodes in a simplified 1-D geometry, equations (6) and (7) can be redefined as follows:

$$R(t) = R[x(t)] = ESR + R_e + R_p(t) = ESR + R_e + R_p[x(t)] \quad (8)$$

$$L(t) = L[x(t)] = ESL + L_e + L_p(t) = ESL + L_e + L_p[x(t)] \quad (9)$$

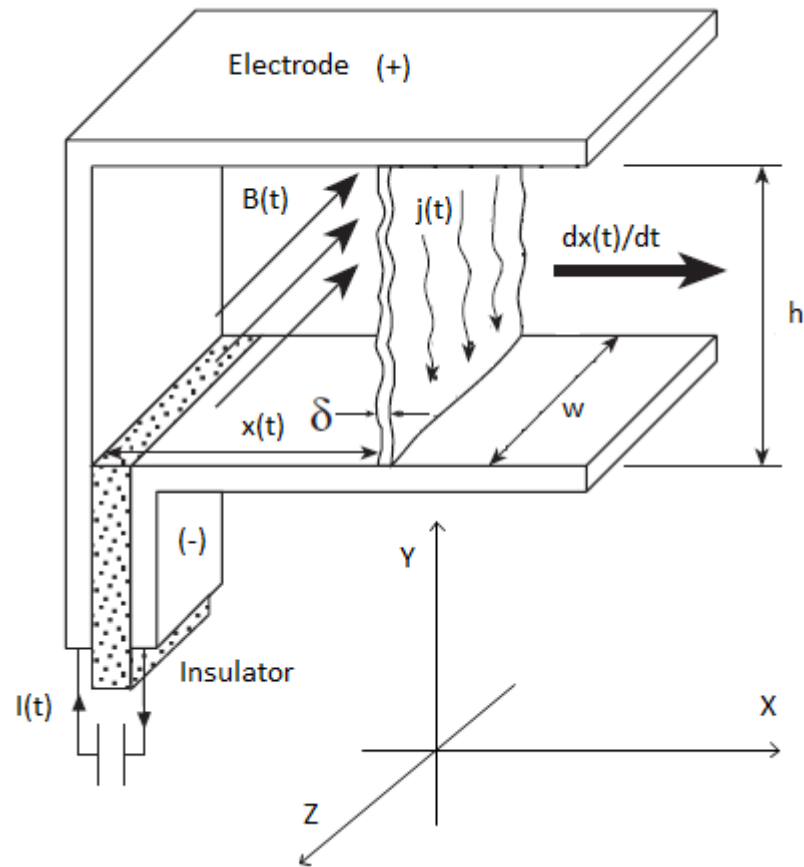


Figure 2-26 - Concept of the propagation of the current sheet in a parallel plate electrode PPT

Applying Kirchhoff's second law to the circuit shown in Figure 2-25, it can be obtained:

$$V_0 - \frac{1}{C} \cdot \int_0^t I(\tau) d\tau - R(t) \cdot I(t) - L(t) \cdot \frac{dI(t)}{dt} - \frac{dL(t)}{dt} \cdot I(t) = 0 \quad (10)$$

Thus, differentiating equation (10) and collecting $I(t)$ and its time derivatives:

$$L(t) \cdot \frac{d^2 I(t)}{dt^2} + \left[R(t) + 2 \cdot \frac{dL(t)}{dt} \right] \cdot \frac{dI(t)}{dt} + \left[\frac{dR(t)}{dt} + \frac{d^2 L(t)}{dt^2} + \frac{1}{C} \right] \cdot I(t) = 0 \quad (11)$$

Taking into account the function composition described in equations (8) and (9), the derivatives of R and L can be expressed as:

$$\left\{ \begin{array}{l} \frac{dR(t)}{dt} = R'(x) \frac{dx(t)}{dt} \\ \frac{dL(t)}{dt} = L'(x) \frac{dx(t)}{dt} \\ \frac{d^2L(t)}{dt^2} = L'(x) \frac{d^2x(t)}{dt^2} + L''(x) \left(\frac{dx(t)}{dt} \right)^2 \end{array} \right. \quad (12)$$

where the differentiation along the direction of motion $x(t)$ has been indicated with an apex:

$$\left\{ \begin{array}{l} R'(x) = \frac{dR(x)}{dx} \\ L'(x) = \frac{dL(x)}{dx} \\ L''(x) = \frac{d^2L(x)}{dx^2} \end{array} \right. \quad (13)$$

Combining equations (11) and (12), it can be obtained:

$$\begin{aligned} L(x) \cdot \frac{d^2I(t)}{dt^2} + \left[R(x) + 2 \cdot L'(x) \cdot \frac{dx(t)}{dt} \right] \cdot \frac{dI(t)}{dt} + \\ \left[R'(x) \cdot \frac{dx(t)}{dt} + L'(x) \cdot \frac{d^2x(t)}{dt^2} + L''(x) \cdot \left(\frac{dx(t)}{dt} \right)^2 + \frac{1}{C} \right] \cdot I(t) \\ = 0 \end{aligned} \quad (14)$$

Equation (14) can be simplified assuming that the resistance $R(x)$ and the inductance variation per unit length $L'(x)$ are constant throughout the discharge. This assumption is generally accepted in the relevant literature and it is supported by experimental evidence for general PPT configurations [19], [20], [3], [89], [90]. Hence assuming:

$$\begin{cases} R'(x) = 0 \\ L''(x) = 0 \end{cases} \quad (15)$$

The circuit inductance can be expressed as:

$$L(x) = L_0 + L' \cdot x(t) \quad (16)$$

At last, combining equations (14), (15) and (16), it can be obtained:

$$\begin{aligned} [L_0 + L' \cdot x(t)] \cdot \frac{d^2I(t)}{dt^2} + \left[R + 2L' \cdot \frac{dx(t)}{dt} \right] \cdot \frac{dI(t)}{dt} + \\ + \left[L' \cdot \frac{d^2x(t)}{dt^2} + \frac{1}{C} \right] \cdot I(t) = 0 \end{aligned} \quad (17)$$

In equation (17) the coupling between the electrical discharge and the plasma sheet dynamics is more explicit, as both the sheet velocity $(dx(t)/dt)$ and acceleration $(d^2x(t)/dt^2)$ appear in the equation coefficients. Therefore, to determine the discharge

current waveform, it is necessary to study also the dynamic evolution of the plasma sheet.

2.3.2. Conservation of momentum equation

In order to keep the model as simple as possible, it is generally assumed that all the thrust is produced by electromagnetic acceleration of the propellant, hence neglecting the electro-thermal component of thrust [19], [20], [3], [89].

It means that under this assumption the neutral plasma generated from the propellant ablation is subject only to the electromagnetic force, i.e. Lorentz force. Hence, the conservation of momentum can be expressed as:

$$\frac{d}{dt}(m(t) \cdot \mathbf{v}(t)) = \int_{V(t)} (\mathbf{j}(t) \times \mathbf{B}(t)) dV \quad (18)$$

where m and \mathbf{v} are the propellant mass and velocity of the plasma. The second term of equation 17 is the integral form of the Lorentz force (equation (1)). This force acts on every charged particles of the current sheet and, therefore, the integration domain is the volume V occupied by the plasma sheet. In general, equation (18) cannot be easily solved in closed form, because it requires the knowledge of the plasma sheet shape and of the current density and magnetic field distributions, which are all rapidly varying in time. Moreover, the solution would depend on the thruster particular geometry.

Nevertheless, it can be shown that an approximate 1-D solution of equation (18) valid for PPT with parallel plate electrodes (as shown in Figure 2-26) can be found with the following assumptions:

- The current sheet can only travel parallel to the thruster axis along the electrodes (\hat{X} axis in Figure 2-26) and it is always perpendicular to it (sheet parallel to the plane $\hat{Y}\hat{Z}$ in the same figure)
- The current sheet thickness δ is constant and small compared to the electrodes dimensions.
- The electrode width w is much larger than the electrode separation distance h .

The latter assumption is necessary to neglect the magnetic field distortions due to edge effects. Therefore the magnetic field and the current density vectors are perpendicular and the Lorentz force is always parallel to the \hat{X} axis. Note that for the second assumption the current density \mathbf{j} is constant in the integration domain if w is constant and the magnetic field \mathbf{B} is constant along the \hat{Y} axis direction in the integration volume.

Taking into account all these assumptions, equation (18) can be simplified as follows [1], [18], [19], [20]:

$$\frac{d}{dt} \left(m(t) \cdot \frac{dx(t)}{dt} \right) = \frac{1}{2} L' \cdot I^2(t) \quad (19)$$

where L' is the inductance per unit of length defined in equation (13) and $x(t)$ is the position of the sheet along the electrodes (see Figure 2-26).

Moreover, for the third assumption if the electrode aspect ratio $h/w \ll 1$, L' is constant and defined as follows [20]:

$$L' = \mu_0 \cdot \frac{h}{w} \quad (20)$$

Unfortunately the condition $h/w \ll 1$ is not often valid, because typically h and w have comparable dimensions [1], [4], [14], [30], [39].

However, for PPT typical electrodes aspect ratio (i.e. between 1 and 5), different author have tried to find the relation between the inductance per unit-of length and the geometry of the electrodes. Burton proposes an empirical equation that describes the inductance of rectangular electrodes of length d_{el} , and thickness τ [1]:

$$L = 0.4 \cdot d_{el} \left(\ln \left(\frac{h}{w + \tau} \right) + \frac{3}{2} - \frac{h}{d_{el}} + 0.22 \cdot \frac{w + \tau}{d_{el}} \right) \quad [\mu H] \quad (21)$$

Hence, the inductance variation per unit length can be calculated as:

$$L' = 0.6 + 0.4 \ln \left(\frac{h}{w + \tau} \right) \quad \left[\frac{\mu H}{m} \right] \quad (22)$$

Finally, according to another approach using a mapping technique developed by Kohlberg and Coburn [91], different values of L' have been found as function of the electrode aspect ratio.

The comparison of the L' calculated using equation (20) and (22) and taken from [91] is shown in Figure 2-27 for different values of h/w .

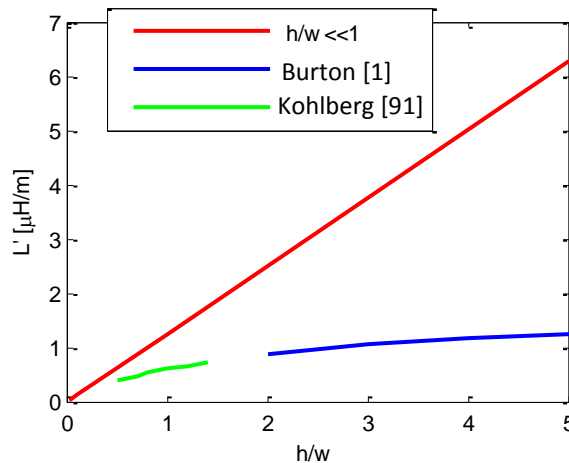


Figure 2-27 – Comparison of L' for different h/w values ($d_{el} = 10$ mm, $\tau = 2$ mm)

Since a typical PPT single shot lasts fractions of a millisecond (usually in the 1 – 100 μ s range [1]), it is common practice to consider the impulse delivered during a

single pulse, i.e. the impulse bit (I_{bit}) rather than the instantaneous thrust (T). The I_{bit} is defined as the time integral of the instantaneous thrust over the thruster pulse duration (t_d). Hence, for equation (19):

$$I_{bit} = \int_0^{t_d} T dt = \int_0^{t_d} \frac{d}{dt} \left(m(t) \cdot \frac{dx(t)}{dt} \right) dt = m_{bit} u_e \quad (23)$$

where m_{bit} is the propellant mass accelerated during a single shot and u_e is the propellant exhaust mean velocity. Using the right hand side of equation (19), I_{bit} can be written:

$$I_{bit} = \frac{1}{2} L' \int_0^{t_d} I^2 dt = \frac{1}{2} L' \psi \quad (24)$$

The impulse bit scales linearly with the integral of the discharge current squared that in the relevant literature is called current parameter ψ , obviously defined as:

$$\psi = \int_0^{t_d} I^2 dt \quad (25)$$

2.3.3. Energy distributions and efficiencies

To provide a proper description of the energy distribution during the discharge, the instantaneous power $P(t)$ transfer from the capacitor to the discharge circuit can be evaluated as follows:

$$P(t) = V_c(t) \cdot I(t) \quad (26)$$

where $V_c(t)$ is the voltage drop across the capacitor bank.

For equation (10), the voltage $V_c(t)$ can be expressed as:

$$V_c(t) = R \cdot I(t) + \frac{d}{dt} (L(t) \cdot I(t)) \quad (27)$$

Hence, combining equation (26) and (27) and using the expressions in equation (12):

$$\begin{aligned} P(t) &= R \cdot I^2(t) + I(t) \cdot \frac{d}{dt} (L(t) \cdot I(t)) = \\ &= R \cdot I^2(t) + \frac{d}{dt} \left(\frac{1}{2} \cdot L(t) \cdot I^2(t) \right) + \frac{1}{2} \cdot \frac{dL}{dt} \cdot I^2(t) \\ &= R \cdot I^2(t) + \frac{d}{dt} \left(\frac{1}{2} \cdot L(t) \cdot I^2(t) \right) + \frac{1}{2} \cdot L' \cdot \frac{dx(t)}{dt} \\ &\quad \cdot I^2(t) \end{aligned} \quad (28)$$

The elements R and L , which appear in equations (27) and (28), are respectively given by equations (7) and (8).

The first term in the last member of the equation (28) represents the power that goes into ohmic heating of capacitors, electrodes and plasma sheet that includes the thermal radiation and the power used to ablate and ionize the propellant. The second term is the power associated with the variation of the magnetic field. It is positive when the current and magnetic fields are increasing or negative when the current is decreasing and the magnetic field gives back power to the capacitor and/or the rest of the discharge. The last term can be rearranged using equation (19) as follows:

$$\begin{aligned} \frac{1}{2} \cdot L' \cdot \frac{dx(t)}{dt} \cdot I^2(t) &= \frac{dx(t)}{dt} \cdot \frac{d}{dt} \left(m(t) \cdot \frac{dx(t)}{dt} \right) \\ &= \frac{d}{dt} \left(\frac{1}{2} \cdot m(t) \cdot \left(\frac{dx(t)}{dt} \right)^2 \right) + \frac{1}{2} \cdot \left(\frac{dx(t)}{dt} \right)^2 \\ &\quad \cdot \frac{dm}{dt} \end{aligned} \quad (29)$$

The first term in the last member of the equation (29) is the power used to change the kinetic energy of the current sheet, i.e. the power that goes into thrust production. The second term is related to the power required for the accumulation of the propellant mass during the discharge [19].

Integrating equation (28) over the duration of the pulse and taking into account the terms of equation (29) yields the distribution of the energy:

$$\begin{aligned} E_0 &= \int_0^{t_d} P(t) dt \\ &= \frac{1}{2} \cdot m_{bit} \cdot u_e^2 \\ &\quad + \int_0^{t_d} \left[R \cdot I^2(t) + \frac{1}{2} \cdot \left(\frac{dx(t)}{dt} \right)^2 \cdot \frac{dm}{dt} \right] dt \end{aligned} \quad (30)$$

where $I(t)$ is assumed to be zero at the beginning and end of the discharge so that any power going into changing the magnetic field is later recovered. The initial energy stored in the capacitor bank E_0 is simply expressed as:

$$E_0 = \frac{1}{2} \cdot C \cdot V_0^2 \quad (31)$$

Equation (30) shows that E_0 is divided between the directed kinetic energy (i.e. the first term of the last member) and two terms that include the resistive loss and the dynamic loss due to the inelastic process of accumulating propellant mass during the discharge.

Hence, considering equation (23), the thruster efficiency η_{th} can be defined as the ratio of the propellant axial kinetic energy to the energy stored in the capacitor [14], [19], [20], [34], [4], [3]:

$$\eta_{th} = \frac{\text{directed kinetic energy}}{\text{initial stored energy}} = \frac{\frac{1}{2} \cdot m_{bit} \cdot u_e^2}{E_0} = \frac{I_{bit}^2}{2 \cdot E_0 \cdot m_{bit}} \quad (32)$$

2.3.4. Constant element PPT discharge model

The simplest model to use to predict the PPT discharge is based on the assumption of keeping the circuit parameters constant for the length of the current pulse, hence decoupling the discharge equations (17) and (19).

Considering the hypotheses introduced in §2.3.1 and observing equation (17), it can be noticed that in order to have only constant electrical parameters the assumption to be made is that the value of L' , its products with x and its derivatives are much smaller than the magnitude of the remaining parameters that appear in equation (17). In the relevant literature it has been shown that this approximation does not produce substantial deviations or errors in the potential drop and current distribution [20], [34], [4], [3]. Even if it is not able to predict the dynamics of the discharge, this simple model can be used to obtain approximate analytic solutions that provide a qualitative description of the waveforms of the current and of the voltage across the electrodes during the discharge pulse.

The equivalent circuit shown in Figure 2-25 becomes a simple RLC circuit that can be described by:

$$L \frac{d^2 I(t)}{dt^2} + R \frac{dI(t)}{dt} + \frac{1}{C} \cdot I(t) = 0 \quad (33)$$

Equation (33) is derived from equation (17) imposing $L' = 0$.

The initial conditions of equation (33) are:

$$\begin{cases} I(0) = 0 \\ \frac{dI(0)}{dt} = \frac{V_0}{L} \end{cases} \quad (34)$$

Equation (33) can be rearranged as follows:

$$\frac{d^2 I(t)}{dt^2} + 2\zeta\omega_0 \frac{dI(t)}{dt} + \omega_0^2 I(t) = 0 \quad (35)$$

where ω_0 and ζ represent respectively the natural frequency and the damping ratio of the system and are defined as:

$$\omega_0 = \frac{1}{\sqrt{LC}} \quad (36)$$

$$\zeta = \frac{1}{2} R \sqrt{\frac{C}{L}} \quad (37)$$

Equation (35) is the equation of the harmonic oscillator, whose analytic solution is straightforward and it strongly depends on the value assumed by the damping ratio. The current waveform is over-damped if $\zeta > 1$, critically damped if $\zeta = 1$ or under-damped if $\zeta < 1$.

From the knowledge of $I(t)$, the voltage drop across the capacitor bank can be calculated as:

$$V(t) = V_0 - \frac{1}{C} \int_0^{\infty} I(t) dt \quad (38)$$

Figure 2-28 and Figure 2-29 show the current and voltage waveforms as a function of the non-dimensional time $\omega_0 t$. Current and voltage have been non-dimensionalized with respect to the factor $V_0/(\omega_0 L)$ and the initial voltage V_0 .

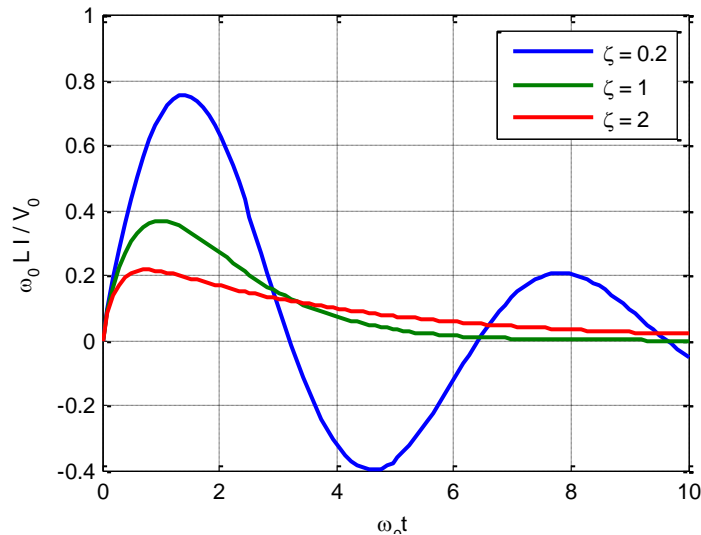


Figure 2-28 - Non-dimensional discharge current (constant element model)

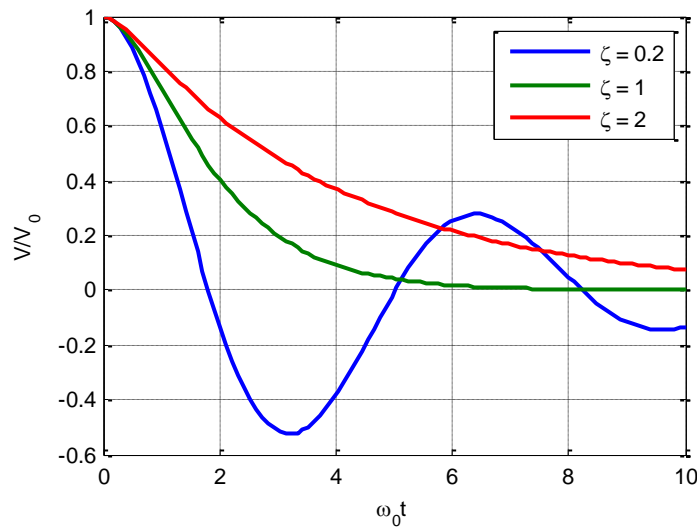


Figure 2-29 - Non-dimensional discharge voltage (constant element model)

It must be noticed that, despite few cases [27], [28] where discharge waveforms very close to the critically damped condition have been reported, PPTs are usually characterised by under-damped discharges. It is caused by the typical values of the C/L ratio (of the order of $10^2 \Omega^{-2}$) and R (of the order of $10 \text{ m}\Omega$) that affect the value of the damping ratio (equation (37)).

Bearing in mind that only PPTs suitable and practicable for miniaturized satellite applications (as discussed in §2.1.2.2) are of interest, it is worth to report the under-damped solution of the equation (35):

$$I(t) = \frac{V_0}{L\omega_0\sqrt{1-\zeta^2}} e^{-\omega_0\zeta t} \sin(\sqrt{1-\zeta^2}\omega_0 t) \quad (39)$$

Moreover for equation (38):

$$V(t) = V_0 \frac{\zeta}{\sqrt{1-\zeta^2}} e^{-\omega_0\zeta t} \sin(\sqrt{1-\zeta^2}\omega_0 t) + V_0 e^{-\omega_0\zeta t} \cos(\sqrt{1-\zeta^2}\omega_0 t) \quad (40)$$

At last, the system energy expression can be derived from the circuit equation (38) and taking into account that in a constant element RLC circuit all the energy employed to change the magnetic field is recovered before the end of the discharge:

$$E = \int_0^{t_d} V(\tau)I(\tau)d\tau = R\psi \quad (41)$$

where the current parameter ψ has been defined once again as the time integral of the current squared over the discharge duration. Therefore, from equations (41) and from the definition of ζ given in equation (37), the current parameter ψ can be expressed as:

$$\psi = \frac{E}{R} = \frac{E}{2\zeta} \sqrt{\frac{C}{L}} \quad (42)$$

2.3.5. Variable element PPT discharge model

Merging the results found in §2.3.1 and §2.3.2, the discharge dynamics of a PPT can be represented as follows:

$$\begin{cases} [L_0 + L' \cdot x(t)] \cdot \frac{d^2 I(t)}{dt^2} + \left[R + 2L' \cdot \frac{dx(t)}{dt} \right] \cdot \frac{dI(t)}{dt} + \left[L' \cdot \frac{d^2 x(t)}{dt^2} + \frac{1}{C} \right] \cdot I(t) = 0 \\ \frac{d}{dt} \left(m(t) \cdot \frac{dx(t)}{dt} \right) = \frac{1}{2} L' \cdot I^2(t) \end{cases} \quad (43)$$

where the first equation is electric charge conservation (equation (17)) and the second equation is the plasma sheet momentum conservation (equation (19)).

In the relevant literature, two possible models are usually derived from the equation (43) according to the assumption that can be made on the ablated propellant mass $m(t)$.

The first model is called *snowplow* model. It is based on the assumption that the mass overtaken by the current sheet is accumulated within it and consequently advances along with it. In other words, the current sheet, originated at the thruster breech, acts like an impermeable sheet, hence sweeping and adsorbing all the gas that it encounters while it propagates down the electrode as it is accelerated by the Lorentz force [19], [20]. Under these hypothesis, $m(t)$ increase during the discharge, hence:

$$\left. \frac{dm(t)}{dt} \right|_{\text{snowplow}} > 0 \quad (44)$$

This model is well accepted in the gas-fed literature [19], mainly because the discharge chamber is completely filled by the propellant before the discharge is initiated. Then, once the current sheet is originated and accelerated by the Lorentz force, it pushes and overtakes all the mass inside the chamber like a piston.

Taking into account equation (44), equation system (43) can be rearranged and the *snowplow* model discharge dynamics obtained (the dependency on time has been omitted for notation simplicity):

$$\begin{cases} [L_0 + L' \cdot x] \cdot \frac{d^2 I}{dt^2} + \left[R + 2L' \cdot \frac{dx}{dt} \right] \cdot \frac{dI}{dt} + \left[L' \cdot \frac{d^2 x}{dt^2} + \frac{1}{C} \right] \cdot I = 0 \\ \frac{d^2 x}{dt^2} = \frac{1}{m} \left[\frac{1}{2} L' \cdot I^2 - \dot{m} \frac{dx}{dt} \right] \\ \frac{dm}{dt} = \dot{m} \end{cases} \quad (45)$$

The last term of the second equation represents the “drag” effect induced by the accumulation and acceleration of mass initially at rest by the current sheet. The mass accumulation process is usually regarded as a loss, which reduces the propellant acceleration and its final velocity, as shown in equation (30) [19], [20].

To solve the system of equation (45), the knowledge of the mass rate $\dot{m}(t)$ during the discharge process is required. It is clear that $\dot{m}(t)$ depends on the heat exchange between the propellant bar and the plasma sheet. The most important factors that influence the heat exchange are the propellant bars and the discharge chamber geometries, the relative position of the current sheet and propellant bars and the plasma characteristics [92]. Therefore, in the most general case, the solution of equation (45) is not trivial.

In order to have a complete description of the discharge dynamics, it is necessary to define the initial conditions. As no current flows at $t = 0$, the plasma sheet is generated at the thruster breech ($x = 0$) with no initial velocity and the initial mass $m = 0$, the five initial conditions for the differential system of equation (45) are:

$$\begin{cases} x(0) = 0 \\ \frac{dx(0)}{dt} = 0 \\ I(0) = 0 \\ \frac{dI(0)}{dt} = \frac{V_0}{L_0} \\ m(0) = 0 \end{cases} \quad (46)$$

An example of solution of the *snowplow* model discharge dynamics is shown in Figure 2-30. The results are obtained using the electric parameters found during the PPTCUP test campaign [4], [3] and assuming a mass rate \dot{m} constant and equal to the ratio between the m_{bit} and the discharge time t_d .

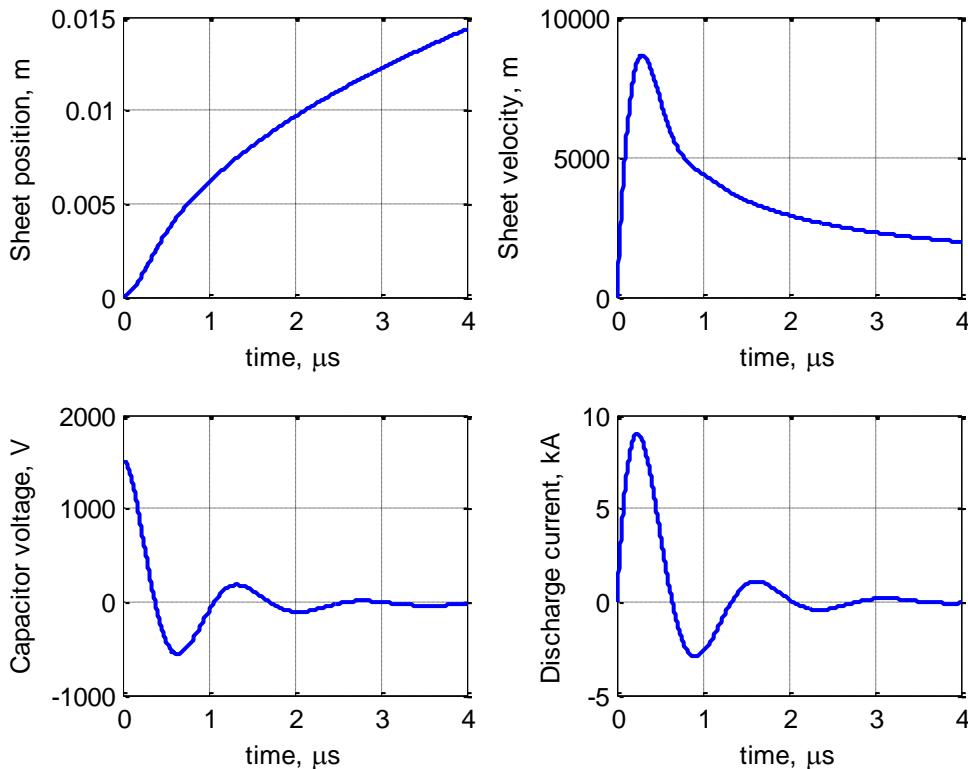


Figure 2-30 - Snowplow model typical results. $E_0 = 2\text{J}$, $R = 70\text{ m}\Omega$, $L = 20\text{ nH}$, $\dot{m} = 3.3\text{ g/s}$, $C = 1.7\text{ }\mu\text{F}$.

The second model is called *slug* model and it can be derived from the *snowplow* model simply assuming:

$$\left. \frac{dm(t)}{dt} \right|_{slug} = 0 \quad (47)$$

$$m(t)|_{slug} = m_{bit} \quad (48)$$

Therefore, the *slug* model is based on the assumption that the entire mass of gas to be accelerated is originated in the initial breakdown event at the minimum inductance configuration. Thereafter no more mass is accumulated or lost as the current sheet is accelerated by the Lorentz force [20], [90]. Historically, this model was developed for the modelling of the *electromagnetic cannons* or *rail guns*, where in a solid conducting element is accelerated along parallel rails [91], [93].

The *slug* model is usually the accepted model for PPTs, in particular breech-fed PPTs, where the propellant mass is assumed to be ablated and included within the current sheet during the early stages of the discharge evolution [20], [90], [94]. Therefore, the whole amount of propellant (m_{bit}) is created at the very beginning of the discharge and accelerated down the electrodes like a bullet in a gun.

Combining equations (43), (47) and (48), the *slug* model discharge dynamics can be obtained (the dependency on time has been omitted for notation simplicity):

$$\begin{cases} [L_0 + L' \cdot x] \cdot \frac{d^2 I}{dt^2} + \left[R + 2L' \cdot \frac{dx}{dt} \right] \cdot \frac{dI}{dt} + \left[L' \cdot \frac{d^2 x}{dt^2} + \frac{1}{C} \right] \cdot I = 0 \\ m_{bit} \frac{d^2 x}{dt^2} = \frac{1}{2} L' \cdot I^2 \end{cases} \quad (49)$$

In order to have a complete description of the discharge dynamics, it is necessary to define the initial conditions. Since no current flows at $t = 0$ and the plasma sheet is generated at the thruster breech ($x = 0$) with no initial velocity, the four initial conditions for the differential system of equation (49) are:

$$\begin{cases} x(0) = 0 \\ \frac{dx(0)}{dt} = 0 \\ I(0) = 0 \\ \frac{dI(0)}{dt} = \frac{V_0}{L_0} \end{cases} \quad (50)$$

An example of solution of the *slug* model discharge dynamics, obtained using the electric parameters and the m_{bit} found during the PPTCUP test campaign [4], [3], is shown in Figure 2-31.

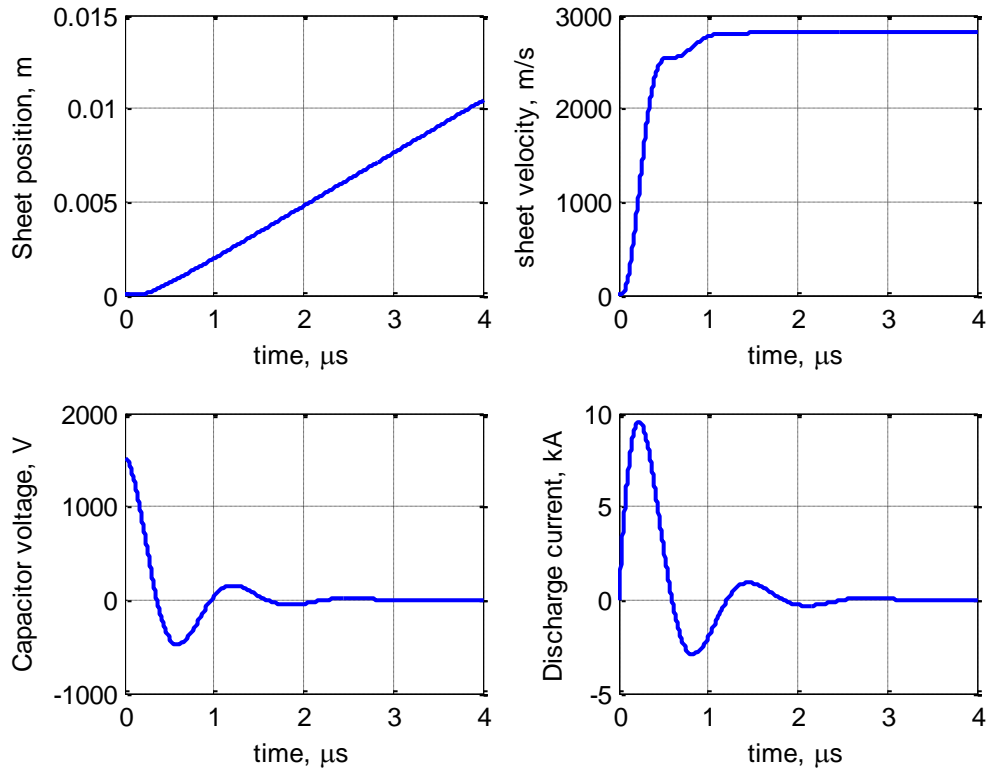


Figure 2-31 - Slug model typical results. $E_0 = 2\text{J}$, $R = 70\text{ m}\Omega$, $L = 20\text{ nH}$, $m_{bit} = 5\text{ }\mu\text{g}$, $C = 1.7\text{ }\mu\text{F}$.

The energy distributions and the efficiency predicted by the *slug* model, combining equation (30) and equation (47), give:

$$E_0 = \int_0^{t_d} P(t)dt = \frac{1}{2} \cdot m_{bit} \cdot u_e^2 + R \cdot \int_0^{t_d} I^2(t)dt \quad (51)$$

For the definition of the current parameter, equation (51) can be usefully rearranged as follows:

$$\int_0^{t_d} I^2(t)dt = \psi = \frac{E_0 - \frac{1}{2} \cdot m_{bit} \cdot u_e^2}{R} \quad (52)$$

Equation (51) shows that E_0 is divided between the directed kinetic energy (i.e. the first term of the last member) and one loss term due to the ohmic losses.

Moreover, noticing that second equation in the system (49) can be written as follows:

$$u_e = \frac{L'}{2m_{bit}} \int_0^{t_d} I^2(t)dt \quad (53)$$

And combining equation (30) and (53), η_{th} can be expressed:

$$\eta_{th} = \frac{\frac{1}{2} \cdot m_{bit} \cdot u_e^2}{E_0} = \frac{1}{8m_{bit}E_0} L'^2 \left(\int_0^{t_d} I^2(t) dt \right)^2 \quad (54)$$

Finally, using the expression found in equation (52), equation (51) becomes [14]:

$$\eta_{th} = 1 + \frac{1}{2K} - \sqrt{\left(1 + \frac{1}{2K}\right)^2 - 1} \quad (55)$$

where the efficiency parameter K is defined as follows:

$$K = \frac{E_0}{8 \cdot m_{bit} \cdot R^2} L'^2 \quad (56)$$

The dependency of η_{th} on the efficiency parameter K is shown in Figure 2-32.

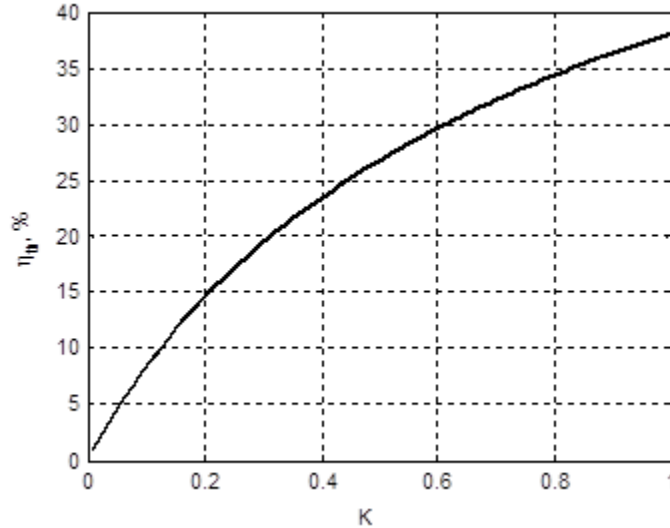


Figure 2-32 - Thruster efficiency against efficiency parameter K .

In conclusion, according to the slug model, the thruster efficiency can be increased with:

- Greater initial energy E_0 . This result is well known in the relevant literature, as summarized in Figure 2-11.
- Greater inductance per unit of length L' that can be achieved changing the electrodes and the discharge chamber geometries, as shown in [94] and [95].
- Smaller mass bit, as shown in [94].
- Smaller resistance, i.e. smaller ohmic losses, according to equations (30) and (42).

Chapter 3. Experimental set-up

To study the factors that affect the lifetime of PPTs for miniaturized satellites applications and to optimize their performance, an innovative side-fed PPT has been designed and extensively tested with the aim of flight-qualifying for the first time a PPT for Cubesat applications.

Starting from the PPTCUP-BB design [4], the PPTCUP qualification model (PPTCUP-QM) has been designed, developed and tested to achieve to purposes of this study. The design of the PPTCUP discharge chamber has required an intermediate step to demonstrate the thruster lifetime. For this reason, an engineering model discharge chamber (PPTCUP-EM) was manufactured and tested before the development of the PPTCUP-QM.

In addition to that, a parallel study on the PPT spark plugs was carried out, because as reported in §2.2.2.2, the spark plug is one of the most critical components of a PPT because it influences both the thruster lifetime and the overall system mass. In the next sections, an overview of instrumentation, the test set-ups and the measurement techniques used to perform the tests and to acquire and process the data is reported in §3.1 and §3.2.

Then, the PPTCUP-EM and PPTCUP-QM designs are reported pointing out the most important design innovations (§3.3 and §3.4). These changes have been made taking into account the previous PPTCUP-BB test results and the lifetime limiting factors and their possible solutions suggested in the relevant literature (§2.2.2). Finally, section §3.5 is dedicated to the description of the different kind of spark plug samples that have been produced and the reasons they have been tested.

3.1. Experimental apparatus

3.1.1. Vacuum facility

All the PPTCUP-EM and NanoPPT tests and most of the tests carried out on the PPTCUP-QM have been performed using the vacuum chamber at the Mars Space Ltd premises. The L-shape stainless steel vacuum chamber shown in Figure 3-1 has 6 KF flanges located on the central main port on the front surface and a DB25 F/T on one of the lateral KF flange. Viewports are mounted on the upper flange, on one of the lateral CF flanges and in the centre of the main port. The main port has another central viewport. Two CF flanges are connected to an “up to air” valve and to a T-pipe, which is connected to the vacuum pump and to the pressure gauge.

The vacuum chamber is provided with a pumping system composed of the following parts:

A Low Vacuum Pumping System which consists of an Edwards two stage 80 m³/h rotary vane pump, used to bring the chamber pressure down to 5x10⁻² mbar. This pump is also used as backing pump for the High Vacuum Pumping System.

- A High Vacuum Pumping System which includes a turbomolecular pumping system, which can bring the chamber pressure a base pressure of about 1·10⁻⁶ mbar. It consists of:
- A Pfeiffer Balzers TPH 2200 turbomolecular pump with a capacity of 2200 l/s. The turbomolecular pump is connected to the lower base flange of the vacuum chamber.
- A Pfeiffer Balzers TCP 5000 Controller.



Figure 3-1 - Vacuum facility at Mars Space Ltd premises.

The EMC characterization of the PPTCUP-QM was performed using the bell jar shown in Figure 3-2 to run the test under vacuum condition.

The bell jar has one KF flange located on the central main port on the top surface. A 4-ways cross is mounted on this flange to ensure that a pressure gauge, an “up to air” valve and an electrical F/T can be used during the test. The vacuum vessel is pumped by a Pfeiffer TPH 520M turbo pump with an MD4TC Vacuubrand membrane pump used as a backing pump achieving a base pressure of about $8E-6$ mbar and an operating pressure of about $2E-5$ mbar.

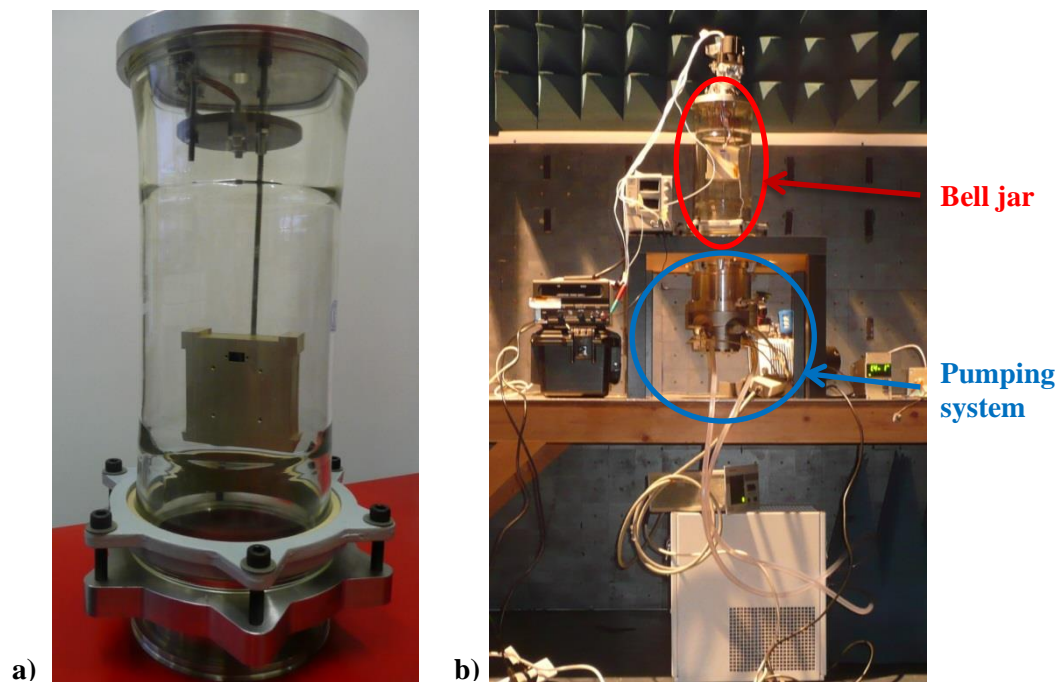


Figure 3-2 – EMC test vacuum facility a) bell jar with the PPTCUP-QM box, b) bell jar and pumping system.

3.1.2. Electrical set-up

During the experimental tests carried out for this study, the PPTs have been fired and monitored using suitable electrical ground support equipment (GSEs) specifically designed for the performed tests.

As described in ANNEX A, the electronics boards developed by Clyde Space that have been used to fire the PPTCUP-EM and QM and the NanoPPT require two dedicated power lines. The electrical schematic of the GSE developed to communicate and control the boards is shown in Figure 3-3. It consists of one PSD30/3B and one EA-PS 2032-050 single output power supplies that feed the PPT conditioning electronics, one LT30/1 double output channel power supply connected to the thrust balance displacement sensor and a DPO3014 oscilloscope. A working station is used to command the unit and to monitor its telemetry. Data will flow from

and to the electronics using an Aardvark I²C/SPI interface. A N2891A differential probe is used to acquire the capacitor voltage signal. A dedicated input channel of the LT30/1 power supply is used to acquire the DB63 optical sensor output signal when the *Ibit* measurements have to be performed.

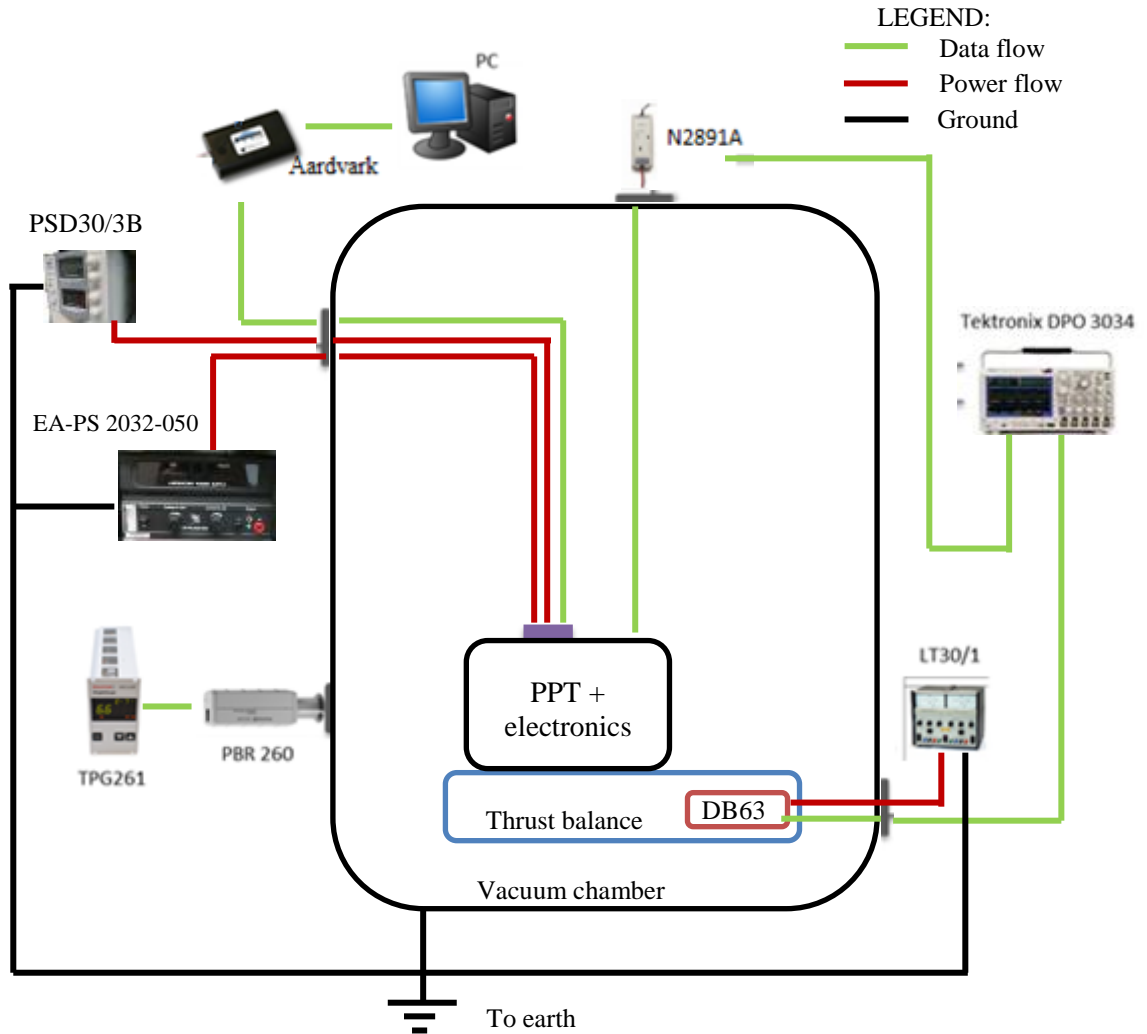


Figure 3-3 – Electrical set-up used for the testing of PPTCUP and NanoPPT driven by their electronic boards

The electronic boards need two dedicated lines: one for the digital circuit and one for the power. The low voltage (LV) ground (i.e. the reference ground of the board and of the power supply units) is connected to the earth ground; whereas the HV reference potential (i.e. the reference potential for the electrodes and spark plug potential) is left floating and insulated from the LV ground using optocouplers. The intellectual properties of the electronic boards shown in Figure 3-3 belong to Clyde Space Ltd and any further details, including the electrical line diagram, cannot be provided.

During the first phases of the PPTCUP-EM testing, the thruster was fired without a dedicated electronics board. However, it was fed by a dedicated GSE, which was specifically designed to charge the PPTCUP-EM main capacitors, to trigger the main discharge and to provide synchronization between these processes. This GSE, which will be called GSE-2 from here on to distinguish it from the GSE shown in Figure 3-3, consists of a NI-USB 6008 and a NI-USB 6211 national instrument data acquisition (NI-DAQ) devices, a DPO3014 oscilloscope and a LT30/1 double output channel power supply. The NI-DAQ boards are connected to a personal computer and used to control the high voltage power supplies (HV-PSs) whose power is provided by the LT30/1 PS.

The 2AA12-P4 HV-PS from UltraVolt is used to charge the main capacitor bank, whereas 15A12-P4 HV-PS from UltraVolt is used to connect the spark plug capacitor bank. To trigger the main discharge, a high voltage relay switch has been included on the spark plug circuit (see Figure 3-4). The switch can be enabled and disabled using the remotely controlled TGP-1100 pulse generator. The GSE-2 complete schematic is shown in Figure 3-6.

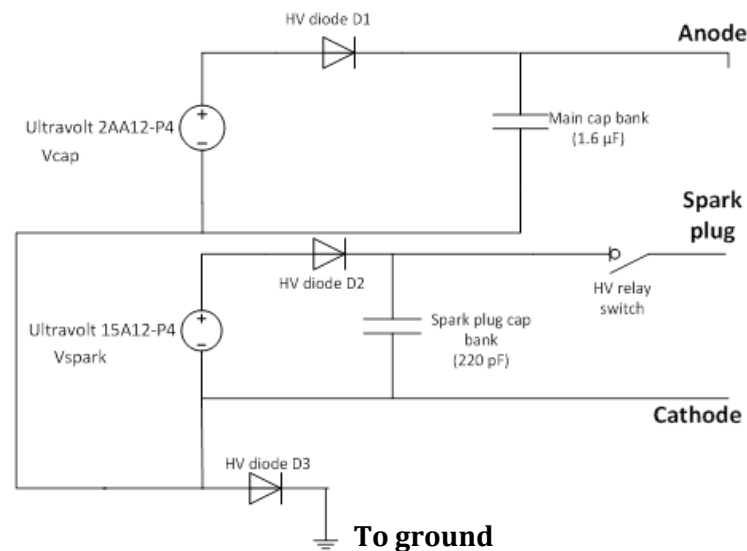


Figure 3-4 – GSE-2 electrical circuit.

Comparing the GSE and GSE-2 grounding schemes, it can be noticed that another significant difference between the two GSEs is the voltage reference of the PPT discharge chamber. In the GSE-2, all the potential references (i.e. cathode, electrical power circuit and vacuum chamber) have to be connected together to ground because of the internal grounding scheme of the UltraVolt power supplies.

In the GSE-2, the charging voltage of the main capacitor bank and of the spark plug capacitor bank can be regulated using a purpose built Labview™ program, which drives the two DC-DC converters through the NI-DAQ boards.

Finally, in both the GSEs a Labview™ program has been used to automatically record all the data acquired by the digital scope, i.e. the signals read by the voltage and current probes and the raw signal from the thrust balance [96].

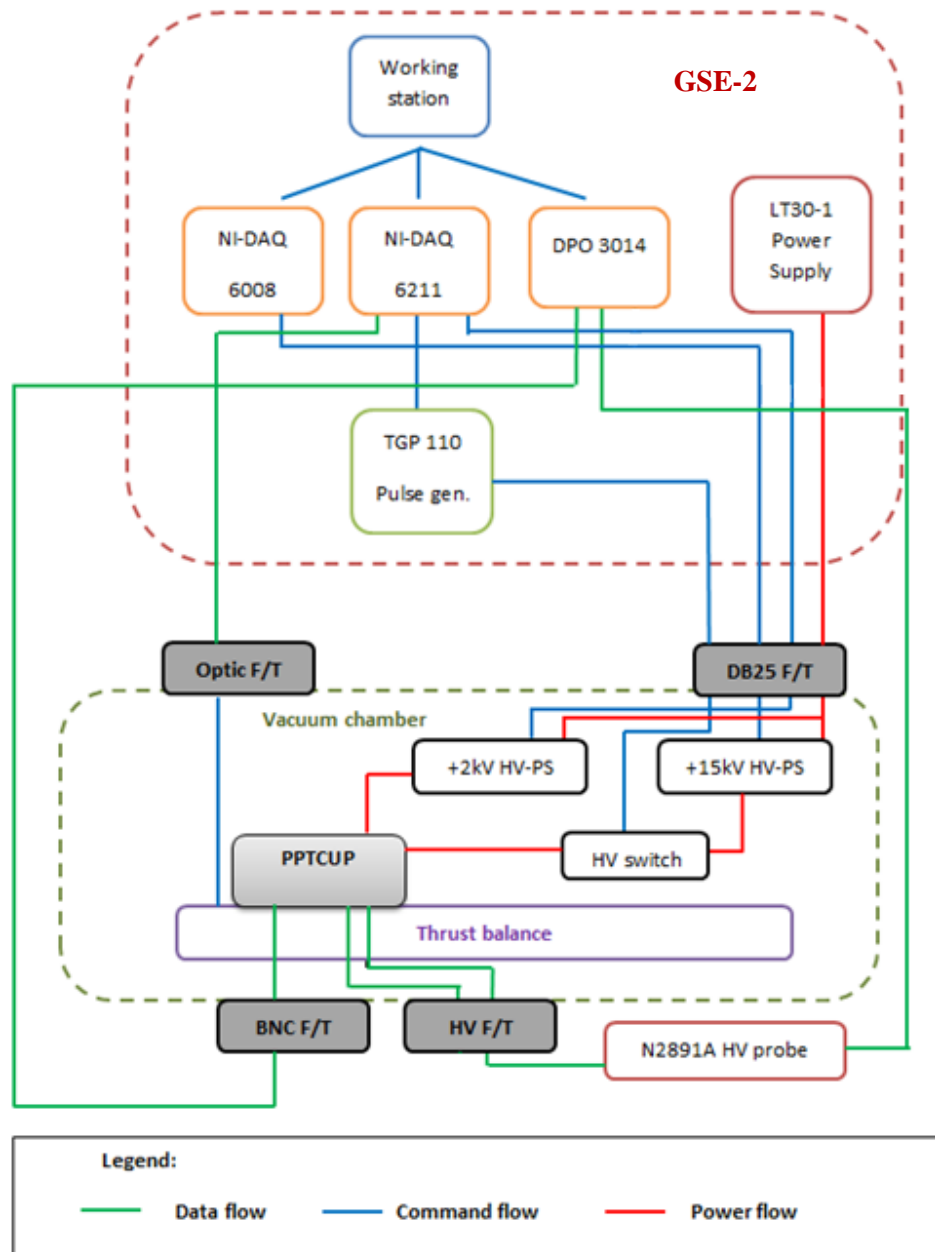


Figure 3-5 – GSE-2 electrical set-up used.

3.2. Diagnostics

3.2.1. PPT electrical characterization

During the experimental tests, the capacitor voltage discharge waveforms have been monitored and often acquired using a HV differential probe that is the only suitable probe that can be used in all the set-ups described in §3.1 because of the different grounding schemes.

The acquired discharge voltage waveforms can be fitted with equation (40) using the constant element discharge model described in §2.3.4. The voltage fitting allows finding the values of R and L that characterize that particular shot. Once these optimal values have been found and noticing that C is known ($C = 1.6 \mu\text{F}$), it is possible to infer the current I flown across the electrodes during the discharge using equation (39) and then the current parameter ψ with equation (25).

3.2.2. Mass bit consumption measurement

The PPTCUP mass bit consumption has been measured using a Mettler-Toledo XP205 high precision scale with an accuracy of $\pm 5 \mu\text{g}$ (Figure 3-6). The averaged m_{bit} consumption has been derived by weighing the whole thruster before and after a sequence of at least 1,000 shots, then subtracting those two values and dividing by the number of performed shot. Therefore, a significant amount of propellant was ablated away from the bars during the whole sequence of shots, allowing the evaluation of their mass loss simply through a scale. Since the typical m_{bit} values for low energy PPTs vary between $3 \mu\text{g}$ and $20 \mu\text{g}$ [1], [9], the effect of a single shot would have been otherwise impossible to measure. Nevertheless, the high precision scale balance combined with the 1,000 shots sequences allows measurement of the averaged m_{bit} with an uncertainty smaller than $\pm 1 \%$. This procedure was repeated during the testing when the m_{bit} measurement was due.



Figure 3-6 – Mettler-Toledo XP205 high precision scale.

3.2.3. Impulse bit measurements

To measure the I_{bit} , the torsional micro-thrust balance developed and fully characterized for the current study has been used. The balance consists of a horizontal pendulum arrangement with the thruster mounted on one end of the arm and a counterbalance on the other (Figure 3-7). The balance is symmetrical with respect to the arm rotation axis with the counterweight and the thruster positioned at the same distance from the central rotating pivot. This will eliminate the error due to gravity effects. All the parts are made out of 6068-T6 aluminium alloy except for the centre pillar that is made out of 302 grade stainless steel. The pillar is mounted through the centre of rotation and in between the two pivots going through the whole of the arm. The balance arm has a rectangular section (50 x 75 mm) and an overall length of 550 mm. Two stainless steel flexural pivots from Riverhawk Co. (5016-600 model) have been chosen for this balance. They are used to constrain the arm so it only has one degree of freedom. The displacement of the balance arm around the axis of rotation is measured with a fibre optic linear displacement sensor.

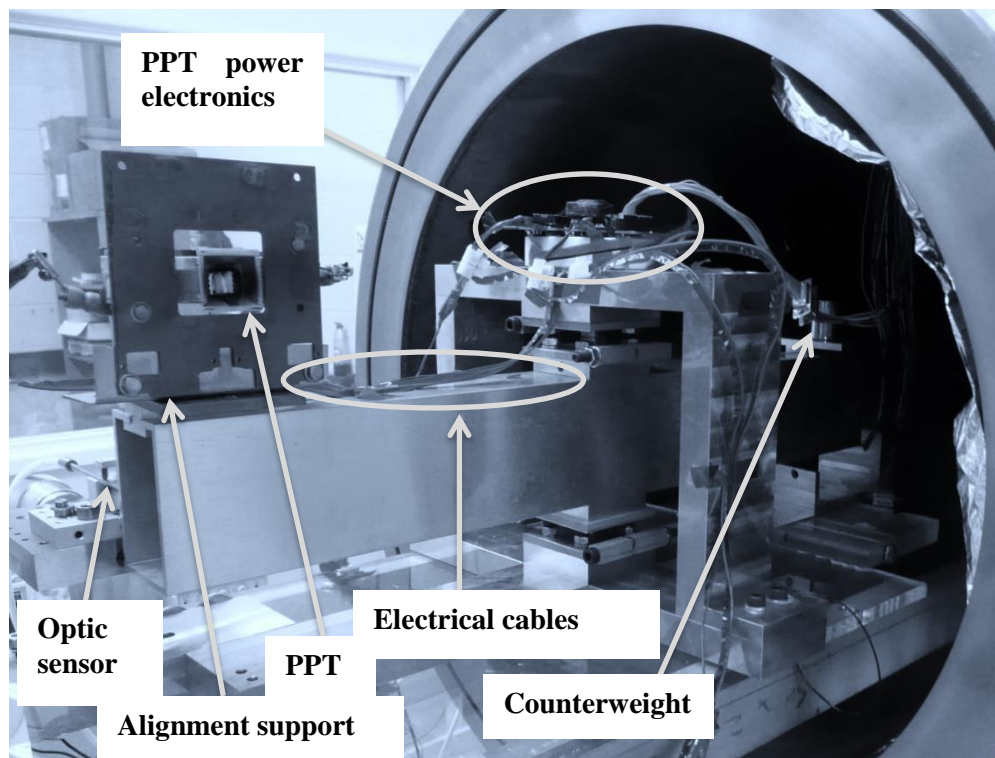


Figure 3-7 – PPT balance set-up. PPTCUP-EM installed on the balance arm

Being a torsional pendulum, the balance can only detect the force component perpendicular to the balance arm and to the rotational axis. If the thruster is not aligned with the balance arm, the thrust component parallel to the balance arm may not be detected. For this reason, the PPT is kept aligned with the misalignment angle $< 1^\circ$ using an alignment support where the thruster can be mounted and fixed with bolts. In this condition, the parallel thrust component proportional to the sine of the misalignment angle is negligible, as shown in Figure 3-8.

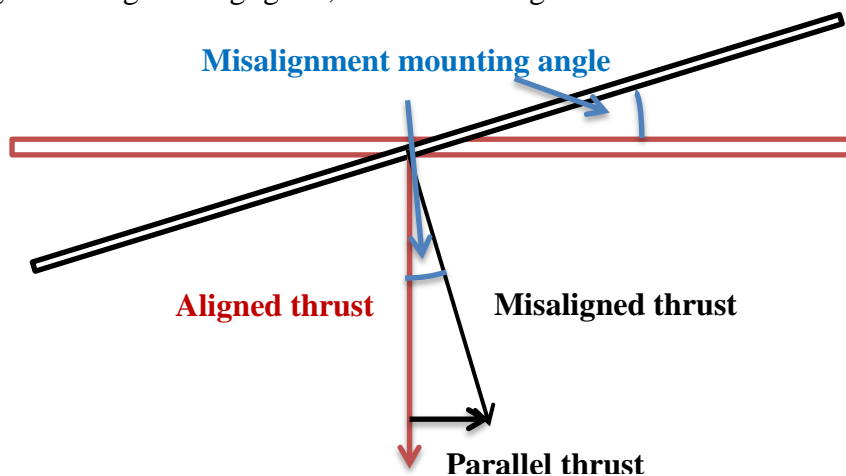


Figure 3-8 – Definition of thrust misalignment and parallel thrust.

Thus assuming that the thrust is perpendicular to the balance arm, the dynamics of a torsional balance are described by the harmonic oscillator equation:

$$J\ddot{\theta}(t) + \lambda\dot{\theta}(t) + k\theta(t) = r_{th}T(t) \quad (57)$$

where θ is the angular displacement, J is the total momentum of inertia about the rotational axis, λ is the damping coefficient, k is the total torsional elastic constant, and $T(t)$ is the applied thrust at the distance r_{th} from the rotational axis (see Figure 3-9).

If t_d is the PPT discharge time the thrust can be modeled as [97]:

$$T(t) = \begin{cases} T & 0 \leq t \leq t_d \\ 0 & t > t_d \end{cases} \quad (58)$$

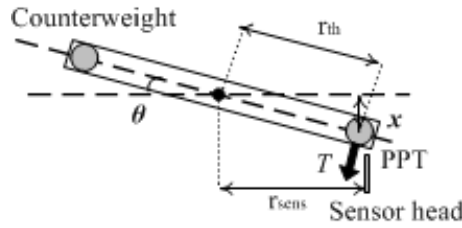


Figure 3-9 – Balance arm schematics (not to scale).

Considering the general solution of equation (57) for $0 \leq t \leq t_d$ and assuming that $t \ll t_{nat}$, where t_{nat} is the balance natural oscillation period, it can be demonstrated [98] that at $t = t_d$

$$\theta(t_d) \approx 0 \quad (59)$$

$$\dot{\theta}(t_d) \approx \frac{r_{th}T}{J} t_d = \frac{r_{th}Ibit}{J} \quad (60)$$

Using equations (59) and (60) as initial values of the homogeneous differential equation (57) for $t > t_d$ leads to

$$\theta(t) = \frac{r_{th}Ibit}{J\omega_0} \exp\left(-\frac{\lambda}{2J}t\right) \sin(\omega_0 t) \quad (61)$$

where ω_0 is by definition

$$\omega_0 = 2\pi f_{nat} \quad (62)$$

From equation (61) the maximum amplitude θ_{max} is defined as

$$\theta_{max} = \frac{r_{th}Ibit}{J\omega_0} \quad (63)$$

For small angular displacements (i.e. $\theta < 5^\circ$), the displacement x_{max} measured by the optical sensor is given by:

$$x_{max} = r_{sens} \sin(\theta_{max}) \approx r_{sens} \theta_{max} \quad (64)$$

where r_{sens} is the distance of the sensor head from the rotational axis.

Combining equations (62), (63) and (64), the following expression for the *Ibit* evaluation can be obtained

$$I_{bit} = \frac{2\pi f_{nat} x_{max} J}{r_{sens} r_{th}} \quad (65)$$

According to equation (65), to evaluate the *Ibit* provided by the thruster five parameters have to be measured or calculated, i.e. the natural frequency f_{nat} , the total momentum of inertia J , the maximum displacement x_{max} measured by the optical sensor and the distances r_{th} and r_{sens} from the rotational axis.

3.2.3.1. Natural frequency evaluation

The natural oscillation frequency f_{nat} depends on the balance arm length and cross section, the mass and position of the thruster that is under test and the counterweight. It is also influenced by the electrical wires fixed on the top of the balance that feed the thruster. However f_{nat} can be easily calculated as the peak of the Fourier transform (FT) of the acquired displacement signal, as shown in Figure 3-10.

This method of measurement takes into account the effects of all the possible sources of influence. It requires the processing of the signal acquired once the balance is set in the final arrangement with the PPT and the counterweight located on the arm tips and the electrical wires connected to the thruster.

The uncertainty in f_{nat} measurement δf_{nat} is the frequency resolution of Fast Fourier Transform algorithm [99] for the given set of samples in the time domain and can be expressed as follow:

$$\delta f_{nat} = \frac{f_s}{2} \cdot \frac{1}{P_2/2 + 1} \quad (66)$$

where f_s is the signal sampling frequency and P_2 is the power of 2 closest to the number of acquired samples. The signal is acquired using an oscilloscope with a sampling frequency of at least 25 kHz for a time of at least 2 minutes, which corresponds to at least 3 million acquired samples ($P_2 = 2^{22} = 4,194,304$). Thus the uncertainty in f_{nat} measurement has an order of magnitude of 1 mHz. Since f_{nat} has an order of magnitude of 1 Hz, the error is $< 1\%$ and can be considered negligible.

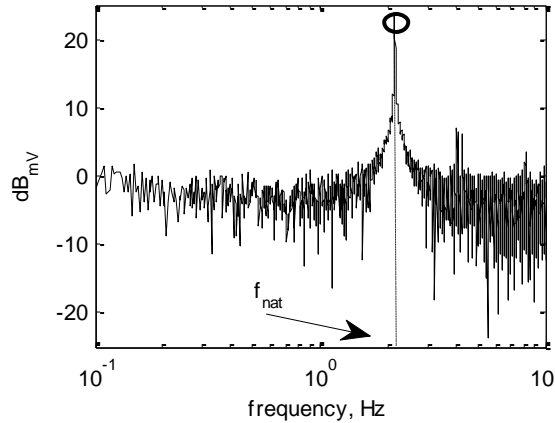


Figure 3-10 - Example of FT used to evaluate the natural oscillation frequency. In the picture $f_{nat} = 2.145 \pm 0.003$ Hz.

3.2.3.2. Moment of inertia evaluation

The total moment of inertia J can be expressed as:

$$J = J_{arm} + J_{th} + J_{cw} \quad (67)$$

where J_{arm} , J_{th} and J_{cw} are respectively the moment of inertia of the balance arm, the thruster under test and of the counterweight. J_{arm} has been evaluated by adding different cylindrical weights on the balance arm and calculating the relative natural oscillation frequency. If two weights having the same shape and size are located symmetrically to the rotational axis, equation (67) can be written

$$J = J_{arm} + 2J_{weight} \quad (68)$$

where the moment of inertia of the tested weight J_{weight} is known. From the definition of the angular velocity ω , it can be obtained

$$2\omega^2 J_{weight} = -J_{arm}\omega^2 + k \quad (69)$$

As ω is calculated with the FT of the acquired signal, equation (69) is in the form of a straight line equation, where the absolute value of the slope is J_{arm} and the intercept is the torsional elastic constant. The weights used for this test are made of steel and have a cylindrical shape. Their mass, which is of the order of 0.1 kg, has been measured with the Mettler-Toledo XP205 mass scale with a resolution of $\pm 5 \mu\text{g}$ (Figure 3-6), whereas their diameter and height, which are of the order of tens of mm, have been measured using a caliper with a resolution of ± 0.25 mm. Therefore, the error in J_{weight} is $< 1\%$.

Repeating the measurements changing the pair of weights and acquiring the relative ω , it has been possible to fit the test results hence evaluating the balance arm moment of inertia and torsional elastic constant (Figure 3-11). The mass of the

weights used for this test is in range of the typical mass of PPTs for miniaturised satellite.

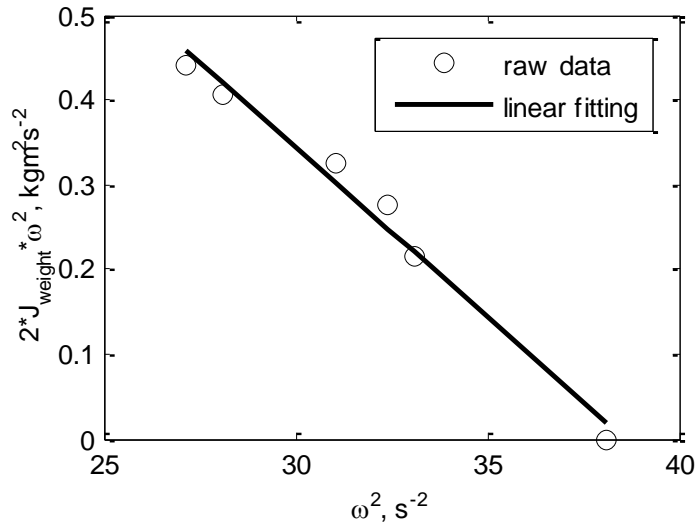


Figure 3-11 - Linear fitting results to evaluate J_{arm} (slope) and k (y-axis intercept). Error bars are not shown because they would not be visible. R-square = 0.9816

The values of J_{arm} and k and their relative uncertainties δJ_{arm} and δk , calculated using the least-square interpolation method [100], are summarized in Table 3-1. As shown in Figure 3-7 and Figure 3-12, the electrical connections and the power supply unit are located on the balance central pillar to minimize the disturbances of the balance arm motion. Only three cables are fixed on the top surface of the balance arm and are used to feed the PPT providing the voltage to apply to its capacitor bank and to trigger the main discharge. These cables might affect the value of the balance torsional elastic constant k whereas their influence in terms of total moment of inertia about the rotational axis is negligible being the ratio between the balance arm and the cables momenta of inertia $< 0.1\%$. However, it has to be noted that the data shown in Figure 3-11 are obtained with the electrical wires fixed on the top of balance. Therefore, the obtained values of J_{arm} and k take into account the electrical cables mechanical influence.

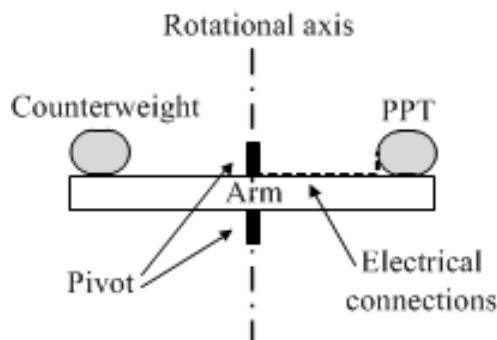


Figure 3-12 – Thrust stand schematic (not to scale) showing the position of the electrical connections

Finally, according to equation (67), only J_{arm} is effectively used for the $Ibit$ calculation.

Table 3-1 - Balance moment of inertia and torsional elastic constant

	Value (from linear fitting)
J_{arm} (kgm ²)	40.2E-3 ± 2.7E-3
k (Nmrad ⁻¹)	1.550 ± 0.086

J_{th} and J_{cw} that appear in equation (67) and their relative uncertainties are known once the thruster to test is set on the balance arm. J_{th} is a geometrical property of the thruster and the counterweight is chosen and placed on the balance arm in order to have $J_{cw} \approx J_{th}$, hence balancing the load that acts on the flexural pivots and allowing the thrust stand to be statically balanced [97].

3.2.3.3. Arm displacement evaluation

The evaluation of the maximum arm displacement x_{max} is obtained by fitting the ideal thrust stand response to the real displacement signal $x_{sens}(t)$ acquired with the optical sensor using the standard least square method [49], [97], [101]. Combining (61) and (63) gives

$$x_{sens}(t) = x_{max} \exp\left(-\frac{\lambda}{2J}t\right) \sin(\omega t) \quad (70)$$

As shown in Figure 3-13, the acquired data $x_{sens}(t)$ always include noise mainly due to background vibrations, i.e. turbo pumps. However, the turbo molecular pump rotates at about 36000 rpm, hence inducing vibrations that have a frequency spectrum peak at about 600 Hz. Considering the data in Table 3-1 and typical PPTs mass (< 400 g, [35]), the thrust stand has a natural oscillation frequency less than 3 Hz. In the present configuration, turbopump induced noise doesn't significantly affect $x_{sens}(t)$ and the data fitting can always be performed with a goodness estimated in terms of R-square coefficient [100], greater than 0.98.

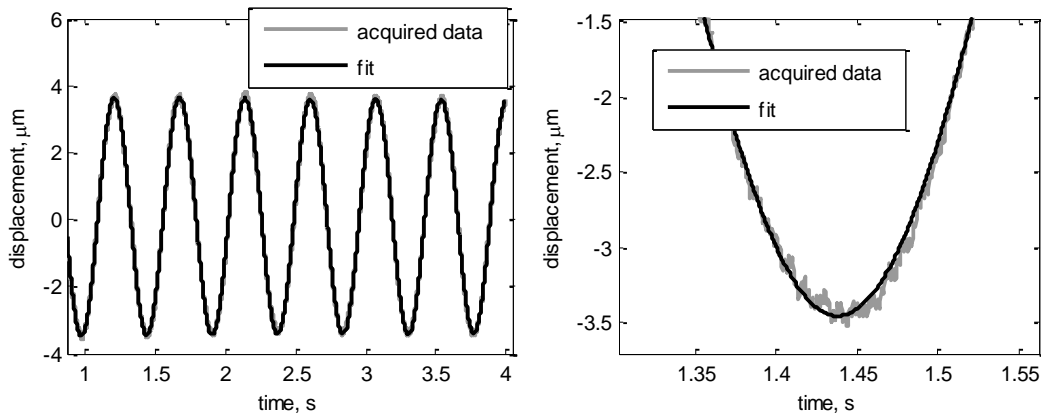


Figure 3-13 - Example of acquired displacement signal (grey curve) and its best fitting (black curve). R-square = 0.9986

The raw optical sensor output signal $\Psi(t)$ is a 0 - 5 V signal. The gap between the sensor head and the balance arm is selected by the micrometer screw to allow the sensor to work in the linear region of its characteristic curve. If α is the slope of the characteristic in the linear region, the following equation can be obtained:

$$x_{sens}(t) = \alpha\Psi(t) \quad (71)$$

The optical sensor is calibrated before starting the *Ibit* measurement by acquiring the output signal $\Psi(t)$ at different values of the gap between the sensor head and the balance arm. The gap is modified using a sliding micrometer screw. From the data so obtained the linear region of the sensor characteristic is selected and fitted (Figure 3-14) to determine the value of α and its uncertainty $\delta\alpha$ using the common equations of the statistics fitting [100].

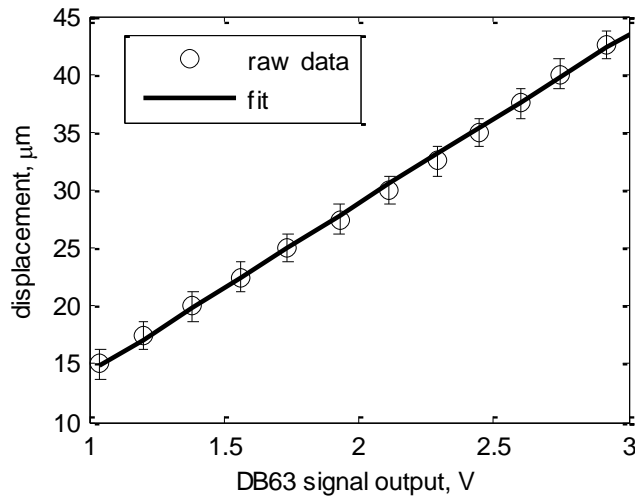


Figure 3-14 - Example of optical sensor linear region characteristic fitting.

Taking into account the sliding micrometer screw resolution (i.e. $\pm 1.25 \mu\text{m}$), it has been found that $\delta\alpha/\alpha$ is typically $< 4\%$.

The error in voltage signal $\Psi(t)$ acquisition is related to the resolution of the oscilloscope used for the measurement ($\pm 5 \text{ mV}$). As the typical $\Psi(t)$ values are in the range between 1 and 3 V in the linear region of the sensor characteristic, the relative error $\delta\Psi/\Psi$ is always $\leq 0.5 \%$. In the present configuration it has been chosen $\delta\Psi/\Psi = 0.5 \%$ for a more conservative error evaluation.

3.2.3.4. Sensor head and thruster distances from rotational axis evaluation

The optical sensor head is placed close to the edge of the balance arm to maximize the distance r_{sens} between the sensor itself and the balance rotational axis, hence maximizing the acquired arm displacement according to equation (65). In the present arrangement $r_{sens} = 270 \pm 1$ mm.

Assuming that the thrust is applied in the geometrical centre of the PPT discharge chamber, the distance r_{th} of the balance rotational axis from the thrust vector is also the distance from the thruster geometrical center and it is known once the thruster is installed on the balance arm. The assumption is made because of the typical PPT discharge chamber symmetric geometry that minimises the thrust vector divergence [102]. The values of r_{sens} and r_{th} are measured with a caliper with a resolution of ± 1 mm.

3.2.3.5. Error budget

The relative uncertainty in $Ibit$ measurement is calculated as:

$$\frac{\delta Ibit}{Ibit} = (1 + \gamma) \sqrt{\left(\frac{\delta r_{th}}{r_{th}}\right)^2 + \left(\frac{\delta J}{J}\right)^2 + \left(\frac{\delta f_{nat}}{f_{nat}}\right)^2 + \left(\frac{\delta r_{sens}}{r_{sens}}\right)^2 + \left(\frac{\delta x_{max}}{x_{max}}\right)^2} \quad (72)$$

It is derived by equation (65) as all the terms that appear in it can be independently measured and their errors are not correlated [100].

The first four terms of equation (72) are known once the PPT to test has been chosen and set on the balance arm with its suitable counterweight. According to equations (70) and (71) the relative uncertainty in x_{max} can be express as:

$$\frac{\delta x_{max}}{x_{max}} = \sqrt{\left(\frac{\delta \alpha}{\alpha}\right)^2 + \left(\frac{\delta \Psi}{\Psi}\right)^2} \quad (73)$$

In equation (72), the term γ has been added to take into account all the unpredictable sources of disturbance, e.g. PPT mounting misalignment angle (Figure 3-8) and thrust vector divergence (§3.2.3.4), thus a more conservative $Ibit$ error evaluation is achieved. The nozzle divergent coefficient C_n that quantifies the divergence losses is given by [103]

$$C_n = \frac{1}{2}(1 + \cos(\theta_n)) \quad (74)$$

where θ_n is the divergence angle. Since $\theta_n = 30^\circ$ in the PPTCUP and NanoPPT designs, the non-axial thrust vector is about the 7% of the total thrust for equation

(74). Therefore, it has been chosen $\gamma = 10\%$ for a worst case estimate of the error. Table 3-2 summarizes the value of all the terms in equations (72) and (73).

Table 3-2 – Balance error budget summary.

Error source	Value (%)
$\delta r_{th}/r_{th}$	0.3
$\delta r_{sens}/r_{sens}$	$< 0.5^a$
$\delta f_{nat}/f_{nat}$	$< 0.5^a$
$\delta J/J$	$< 7^a$
$\delta \alpha/\alpha$	3.8
$\delta \Psi/\Psi$	0.5

^a The exact value depends on the actual PPT under test

In the present configuration, the uncertainty in *Ibit* measurement is 8.8%.

3.2.3.6. Balance noise analysis

Acquired data are always affected by the mechanical noise induced on the balance by background vibrations, i.e. turbo pumps. In this case, considering equations (57) and (64) and assuming small angular displacements (i.e. $\theta < 5^\circ$), the dynamics of a torsional balance can be express in term of arm displacement $x(t)$ by the following equation:

$$\ddot{x}(t) + 2\zeta_t \dot{x}(t) + \omega_0^2 x(t) = \frac{r_{sens}}{J} N(t) \quad (75)$$

where $N(t)$ is the torque induced by the vibrations and ζ_t is by definition

$$\zeta_t = \frac{\lambda}{2J} \quad (76)$$

Performing the Laplace transform to equation (75) and taking into account the initial conditions of the problem reported in equations (59) and (60), the following equation can be evaluated:

$$X(s) = H(s)N(s) + H(s)r_{th}Ibit = X_N(s) + X_{sol}(s) \quad (77)$$

where the balance transfer function $H(s)$, shown in Figure 3-15, is given by:

$$H(s) = \frac{r_{th}/J}{s^2 + 2\zeta_t s + \omega_0^2} \quad (78)$$

For equation (77) the solution $X(s)$ consists of two terms: $X_N(s)$ which is due to the noise and $X_{sol}(s)$ which is the ideal solution. Note that the inverse Laplace transform of the latter term is equivalent to equation (70).

Since equation (75) and the Laplace transform operator are linear, the effect of the noise can be analysed considering only the term $X_N(s)$.

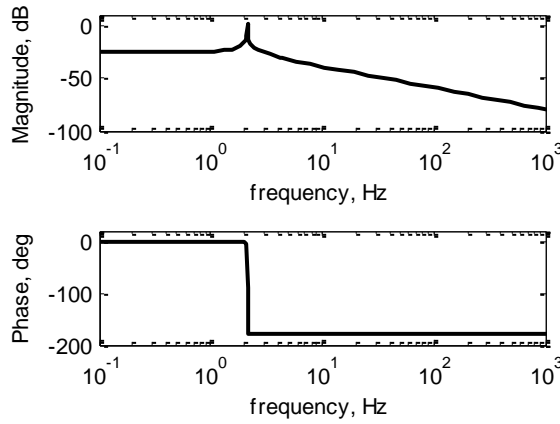


Figure 3-15 - Balance Bode diagrams ($\zeta_t = 0.0145 \text{ s}^{-1}$ and $\omega_0 = 13.44 \text{ rad s}^{-1}$).

The displacement sensor has been used to acquire the arm displacement $x_N(t)$ only due the vibrations (without any PPT shots). For equation (75), if the FT of the $x_N(t)$ is known, it is possible to calculate the FT of the noise $N(t)$ as follows [104]:

$$FT[N(t)] = \frac{FT[x_N(t)]}{H(s)} \quad (79)$$

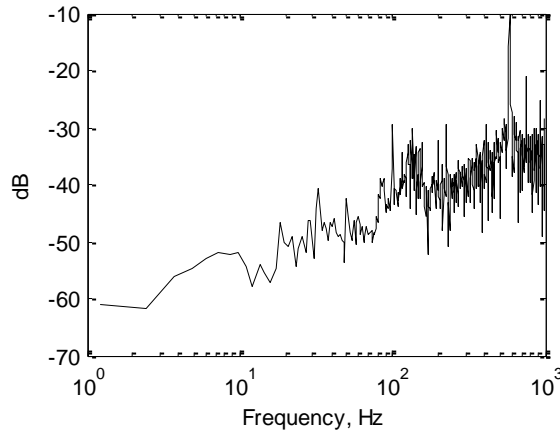


Figure 3-16 - Induced noise $N(t)$ FT.

The FT magnitude of the induced noise is shown in Figure 3-16. Note that it reaches the maximum at about 600 Hz which is the rotational frequency of the pump. Finally to quantify the order of magnitude of $x_N(t)$ and to compare this value with the ideal solution $x_{sol}(t)$, the root mean square (RMS) method has been used. The RMS noise has been evaluated integrating the FT of $x_N(t)$, whereas the RMS amplitude of the ideal solution is simply calculated as the ratio between its amplitude and $\sqrt{2}$ because $x_{sol}(t)$ is a sine wave for equation (70). The results are shown in Figure 3-17.

It has been found that, as the natural frequency of the balance is about 2 Hz, the noise RSM is $< 2\%$ of the ideal RMS amplitude, depending on the actual I_{bit} for equation (65). This justifies the reliability and the goodness of the data fitting estimated in terms of R-square and the overall I_{bit} uncertainty of the balance (i.e. typically less than 9%), that is smaller than the error values that characterize other impulsive torsional pendulums for PPTs applications (12 and 15%, as reported respectively in [4] and [98]).

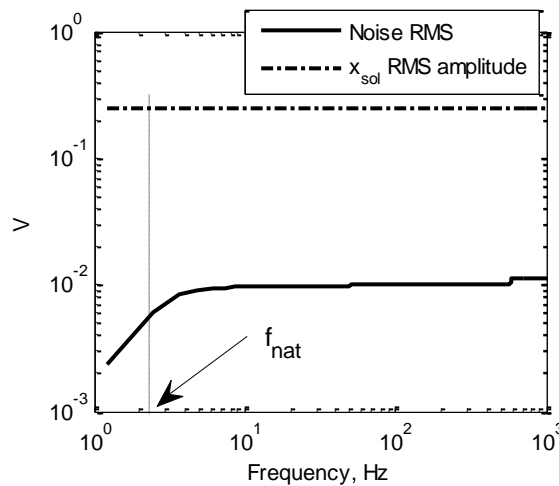


Figure 3-17 – Comparison between the inducted noise RMS and the ideal RMS amplitude (in the example $I_{bit} = 40 \mu\text{Ns}$)

3.3. PPTCUP discharge chamber engineering model (PPTCUP-EM)

The PPTCUP-EM design is based on the previous breadboard model design. The PPTCUP-BB performance was found to be in line with the requirements, however the thruster was able to perform only a few thousands shots mainly because of failures occurring in the capacitor banks and short circuiting of the electrodes due to carbonization [3]. Therefore, the changes of the discharge chamber EM design have been made taken into account the BB main thruster issues and their possible solutions suggested in the relevant literature [29], [30], [31], [39], [47], [58], [59]. The overall dimensions of the discharge chamber, shown in Figure 3-18, have not been significantly changed in the EM design.

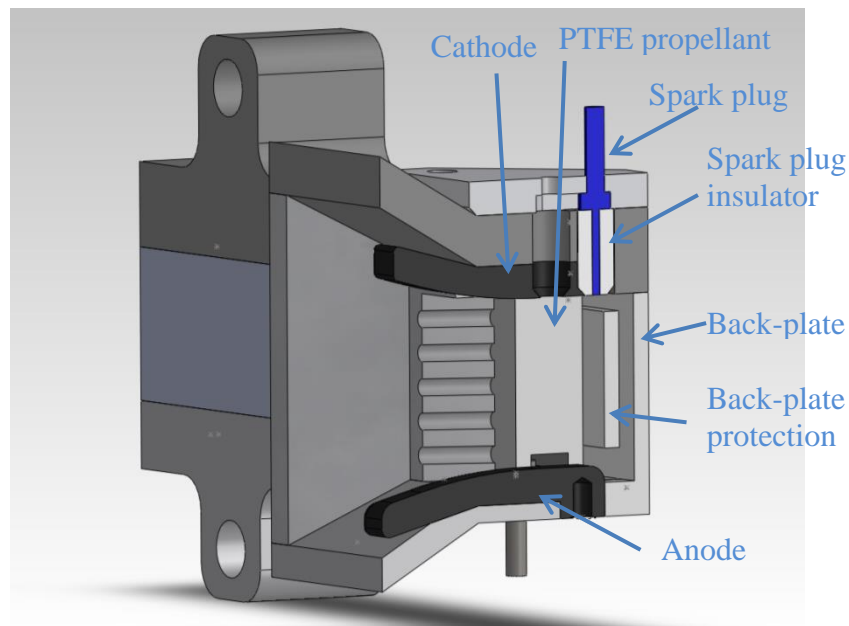


Figure 3-18 – 3D section of the PPTCUP-EM discharge chamber

The initial mass of the propellant (M_{prop}) is about 8 g. The propellant area exposed to the main discharge is about 0.0001 m^2 . The whole test campaign has been performed at $E_0 = 2.00 \pm 0.02 \text{ J}$, which corresponds to an initial voltage $V_0 = 1720 \pm 10 \text{ V}$. The spark plug, which is used to trigger the main discharge, operates with an initial energy of about 0.01 J and an applied voltage of 7.5 kV. As for the breadboard model, the PPTCUP-EM has a $1.6 \mu\text{F}$ capacitor bank, used to store the shot energy E . The bank consists of a parallel arrangement of 8 ceramic capacitors rated up to 2000 V and with a nominal capacitance $C = 200 \text{ nF}$. These capacitors have been chosen after an extended test to prove their reliability when used for pulsed applications to avoid failures similar to those occurred during the PPTCUP-BB test campaign.

The PPTCUP-BB and model design comparison is shown in Figure 3-19. The main design changes are:

- The shape of the electrodes,
- The shape of the lateral nozzle walls,
- The back-plate geometry,
- The material chosen for manufacturing the parts,
- The spark plug system.

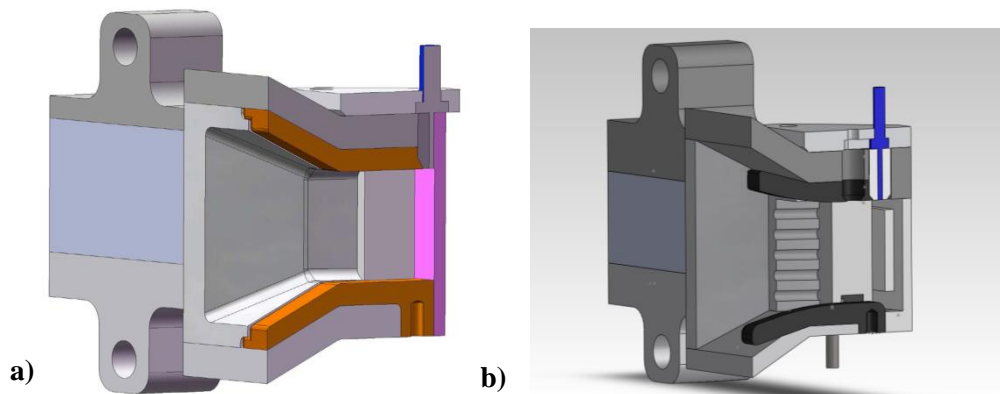


Figure 3-19 – 3-D section views of PPTCUP-BB (a) and PPTCUP-EM (b)

The PPTCUP-EM was tested in two different feeding configurations, i.e. the side-fed and the V-fed configurations [42]. The divergence angle α_d that characterizes the V-fed configuration (see Figure 3-20) has been fixed to 15° . The possibility of testing the thruster in different configurations allowed the acquisition of more data to prove the PPTCUP-EM lifetime and, at the same time, to optimize the thruster performance.

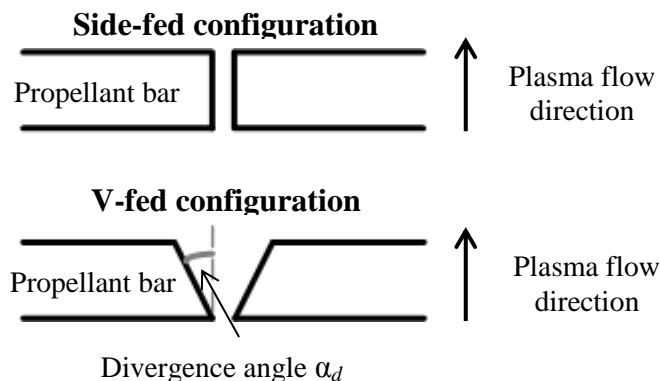


Figure 3-20 - Definition of side-fed and V-fed configurations.

3.3.1. Electrode shape

The EM electrodes have been re-designed to improve the PPTCUP overall performance. They are about 18 mm long; the width w is about 6 mm and the thickness τ is about 2 mm.

As shown in Figure 3-21, the new electrodes have a rectangular shape similar to the old ones. They are characterized by a divergence of 15° , with the old electrodes having a 30° divergence. This divergence angle value has been proved to optimize low energy PPTs [1], [13]. The separation distance of the electrodes h is about 10 mm.

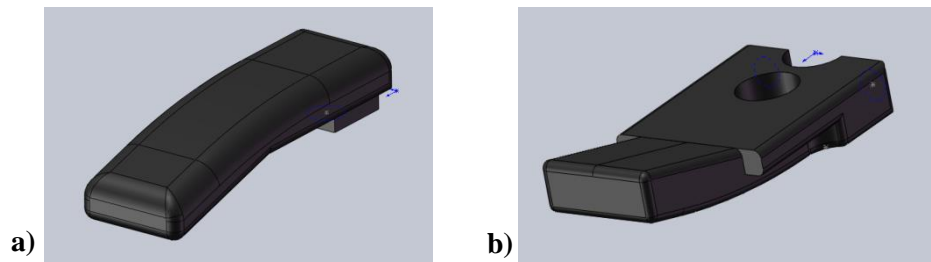


Figure 3-21 – 3-D models of the EM electrodes: a) Lower electrode (anode), b) Upper electrode (cathode)

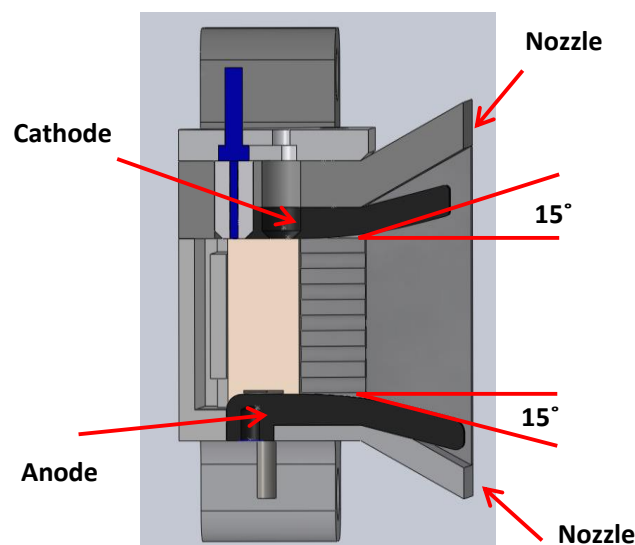


Figure 3-22 - Details of electrodes divergence angle

Since the nozzle angle divergence has not been modified and it is equal to 30° , it results that in the new configuration the electrodes are not parallel to the upper and bottom nozzle walls. This will help to avoid the creation of a conducting path on the inner walls of the discharge chamber (for the carbonization effect) that might short the two electrodes leading to a fatal failure of the thruster.

The creation of a gap between the electrodes and the nozzle walls (Figure 3-23) is an easy solution to this issue preventing the physical short circuiting of the electrodes unless a carbon layer thick enough to fill the gap (0.8 mm) is deposited.

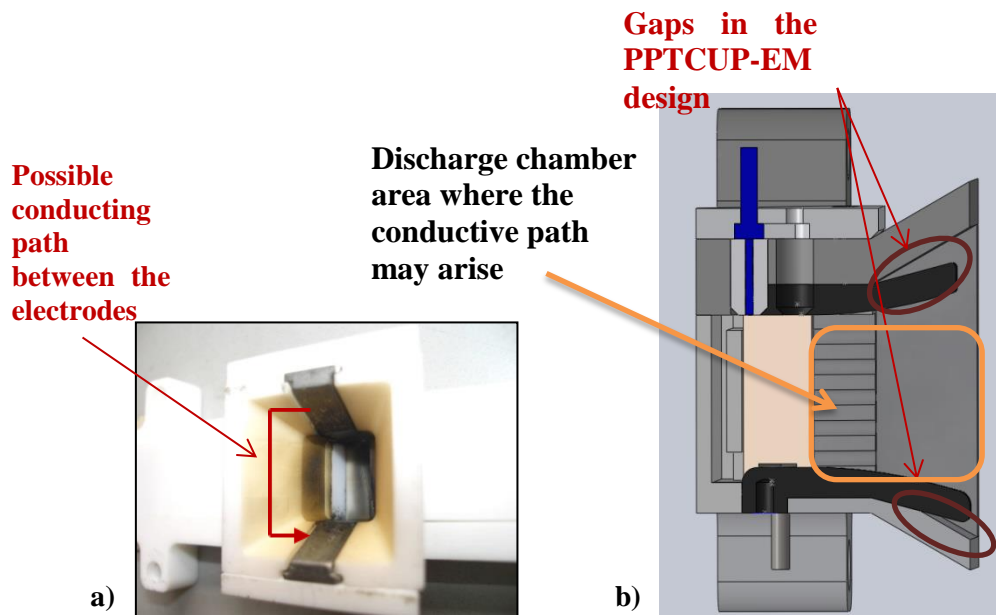


Figure 3-23 – a) Possible conducting path on the nozzle wall, due to the carbonization effects (PPTCUP-BB) [105] b) gap between the electrodes and the walls (PPTCUP-QM)

The electrode material has not been modified, hence a copper-tungsten (75% W – 25% Cu) alloy will be employed. This material has been chosen for its low electrical resistivity (37 nΩm) and for its good mechanical and thermal properties and reduced erosion rates, which have been proved to be particularly attractive for PPT applications [14], [17].

3.3.2. Nozzle side walls shape

In order to prevent a shorting between the electrodes due to the carbonization effects, lateral grooves have been introduced to increase the total surface that will be coated by the carbon film that might eventually short the two electrodes. As reported in §2.2.2.1, in the past grooves have been already successfully included in design of the PPTs to reduce the chance of electrode short-circuiting due to carbonization (Figure 2-13). For these reasons, the nozzle side walls have been modified as shown in Figure 3-24. Five equally distributed lateral grooves have been added to maximise the surface of the nozzle close to the propellant bar, as shown in Figure 3-18, where the Teflon vapour density is higher [29], [31].

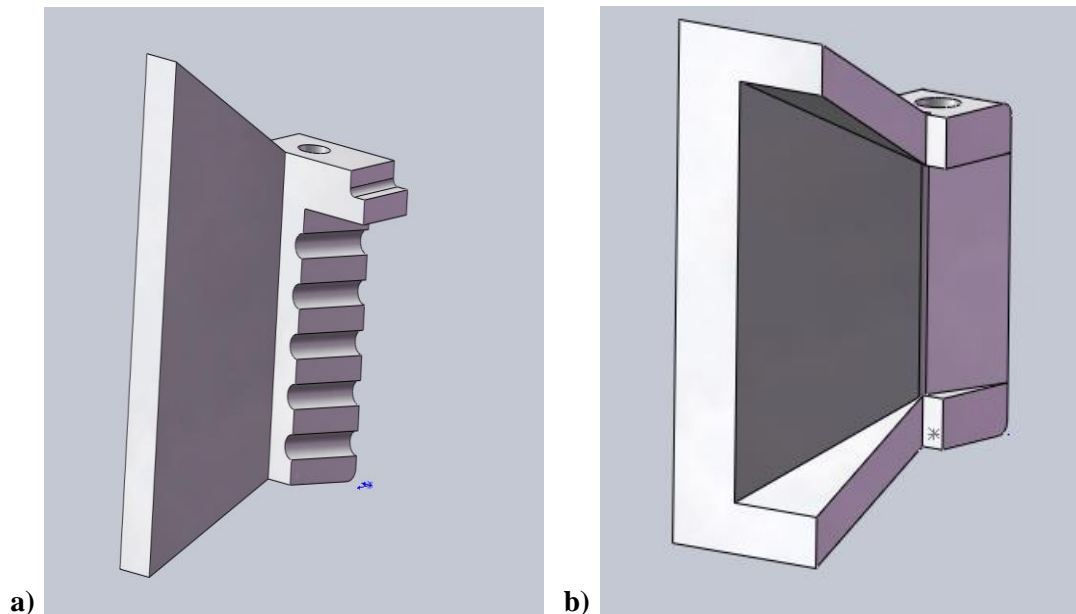


Figure 3-24 – Lateral nozzle walls (a) PPTCUP-EM, (b) PPTCUP-BB.

3.3.3. Back-plate geometry

The PPTCUP-BB back-plate proved to be the component most affected by carbonization [105]. To prevent the short circuit in this critical area, a configuration like the one shown in Figure 3-25 has been selected. Instead of using a single back-plate, the PPTCUP-EM has two back panels, named back-plate and back-plate protection. The carbon film created by the carbonization will mainly deposit on the back-plate protection surface that is not directly connected to the electrodes and this should prevent the shorting.

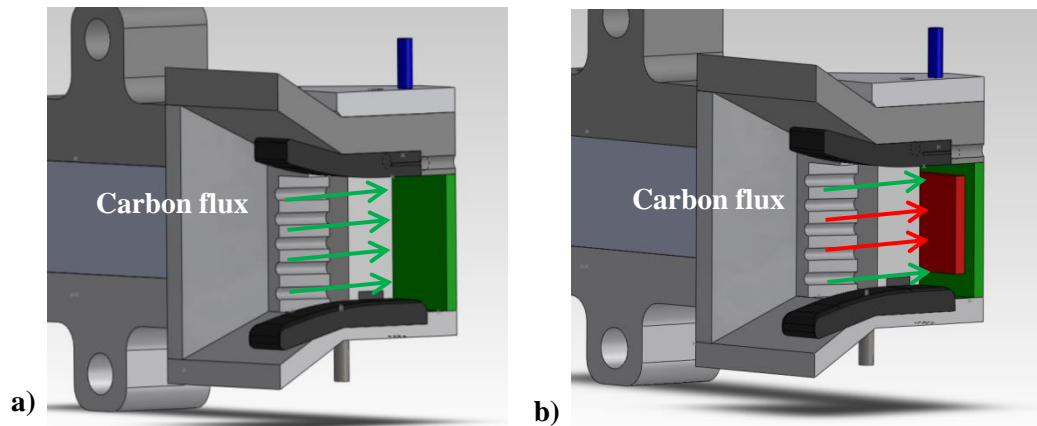


Figure 3-25 – a) Configuration without back plate protection: carbon deposited on the back-plate (in green) shorting the electrodes. b) Configuration with back-plate-protection (in red): no electrodes shorting

3.3.4. Housing material

All the PPTCUP-BB housing parts were made of Macor, with the only exception of the back-plate that was manufactured using different materials (i.e. Macor, boron-nitride and Shapal-M), because it was the component most affected by carbonization [105]. The PPTCUP-EM housing is entirely made of Shapal-M. This material was chosen for two main reasons:

- In the PPTCUP-BB test campaign, the back plate made of Shapal-M proved to be less affected by carbonization than Macor and boron-nitride, as shown in Figure 3-26. According to [105], this is due to the different porosity of the materials.
- Shapal-M is less brittle and overall has better mechanical properties than Macor (see Table 3-3) hence its use should reduce the chances of the development of cracks in the thruster that could lead to a mechanical failure.

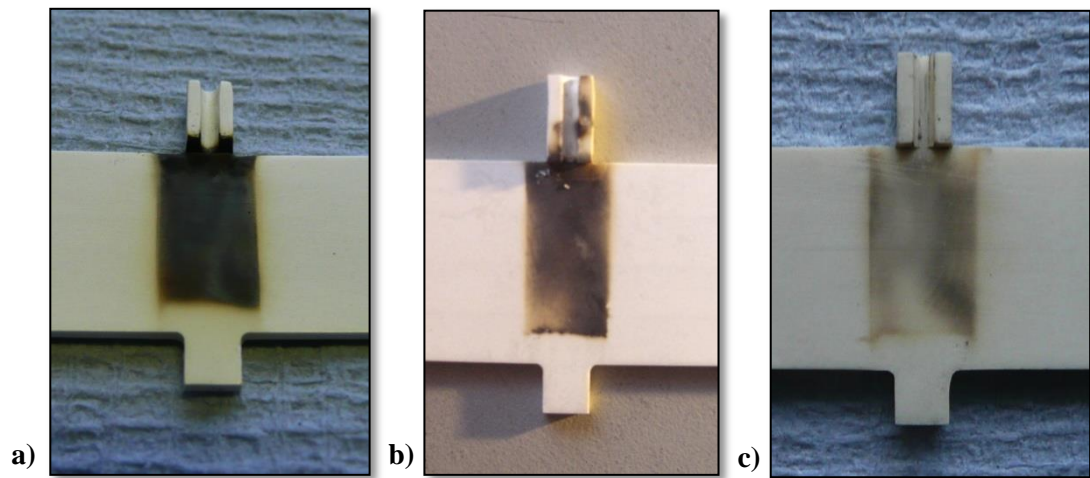


Figure 3-26 – PPTCUP-BB back plate carbonization a) Boron nitride b) Macor c) Shapal-M. Pictures taken after about 1000 shots [105]

Table 3-3 – Macor and Shapal-M physical properties comparison

Physical property	Shapal-M	Macor
density (g/cm ³)	2.92	2.52
Young's module (GPa)	160	67
Poisson's ratio	0.31	0.29
Maximum Use Temperature in vacuum (°C)	1900	800

3.3.5. Spark plug electrodes

The PPTCUP-EM spark plug design has been significantly modified. Due to its design, the PPTCUP-BB spark plug assembly was very complicated to assemble. This sometimes resulted in malfunctioning of the thruster due to problems in the spark assembly. Considering that the spark plug is one of the most delicate components of a PPT, its design was changed to make it easier to assemble and more fault proof and reliable.

In the EM configuration, the upper electrode (cathode) has two holes in which the plug and the plug insulator can be inserted. The possibility of changing the spark plug position has been introduced to test different configuration and to verify if the spark position affects the lifetime and/or the performances of the thruster. The two spark plug position will from now on be referred to as *Close* and *Far Hole*. The former is the closest to the capacitor bank, on the inner edge of the cathode; the latter

is furthest from the capacitor bank. The position of the *Close Hole* is typical of most of the PPTs since it allows the spark plug to be at the breech of the thruster where the inductance of the equivalent RLC circuit that describes the main discharge is minimum (§2.1.1). Finally, the position of the *Far Hole* is driven by geometrical considerations.

The spark plug has a square-shaped end. Its edges, together with the sharp lofted edge of the cathode holes visible in Figure 3-27, may improve the trigger discharge reliability.

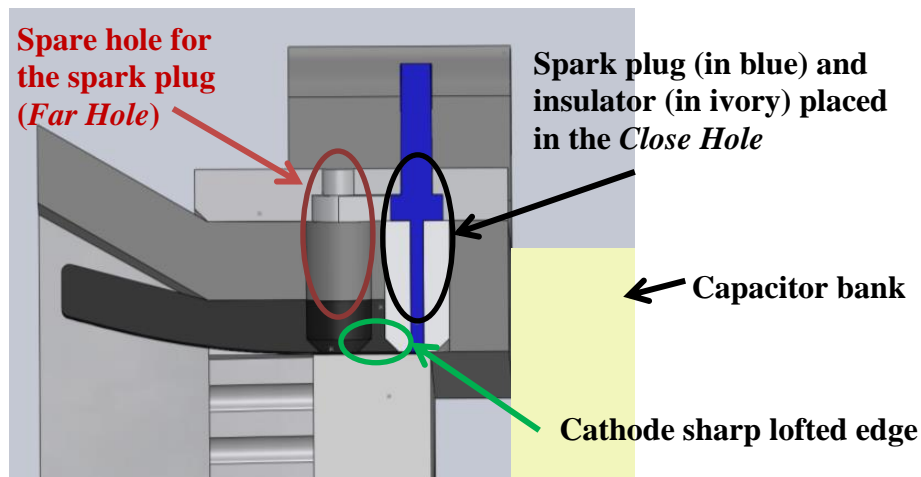
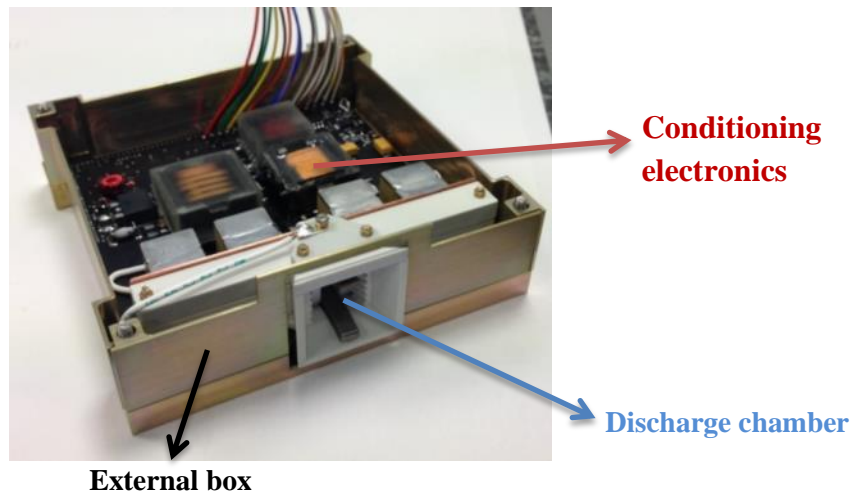


Figure 3-27 – 3D section of the PPTCUP-EM spark plug system (plug inserted in the *Close Hole*).

3.4. PPTCUP qualification model (PPTCUP-QM)

As shown in Figure 3-28, the PPTCUP-QM module consists of three main parts: the discharge chamber, which is the ablative PPT developed from the previous BB and EM models, the conditioning electronics, designed and manufactured by Clyde Space Ltd, and the external metal box. The overall dimensions are 100 x 100 x 33 mm³ and the initial total mass is about 270 g.

Figure 3-29 shows a possible thruster-satellite configuration, where the PPTCUP-QM module is connected to two 1U Cubesat structures [106]. The module can be used to deliver thrust along the **X** or **Y**-axis of a Cubesat, depending on how the PPTCUP-QM is mounted in the satellite structure.



External box

Figure 3-28 - PPTCUP-QM module (without the box lid).

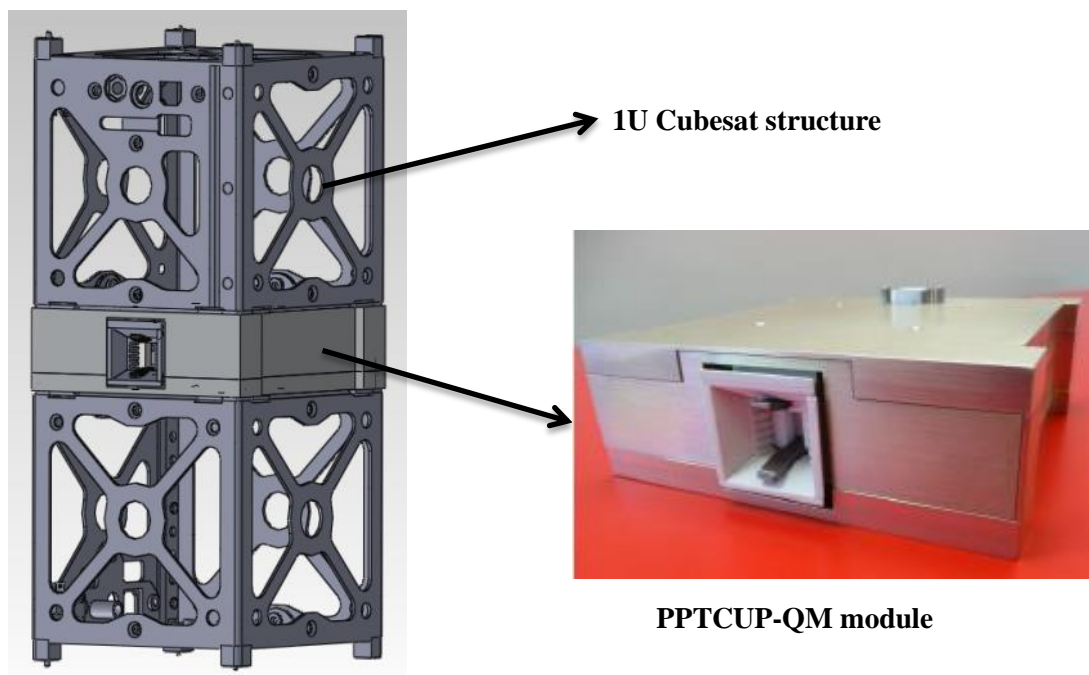


Figure 3-29 - Example of possible PPTCUP-QM assembly with Cubesat structures.

3.4.1. QM discharge chamber

The overall dimensions of the discharge chamber have not been significantly changed in the QM design and are the same reported in §3.3. The only changes are the mounting holes that in the QM have to assure the mechanical interfaces between the discharge chamber and the electronic board and the spark plug position. In the

QM, the cathode has one single hole where the spark plug can be mounted. The position of the hole is chosen between the *Close* and *Far Hole* (Figure 3-27) depending on the best performance measured during the PPTCUP-EM test campaign. Figure 3-30 shows the discharge chamber components.

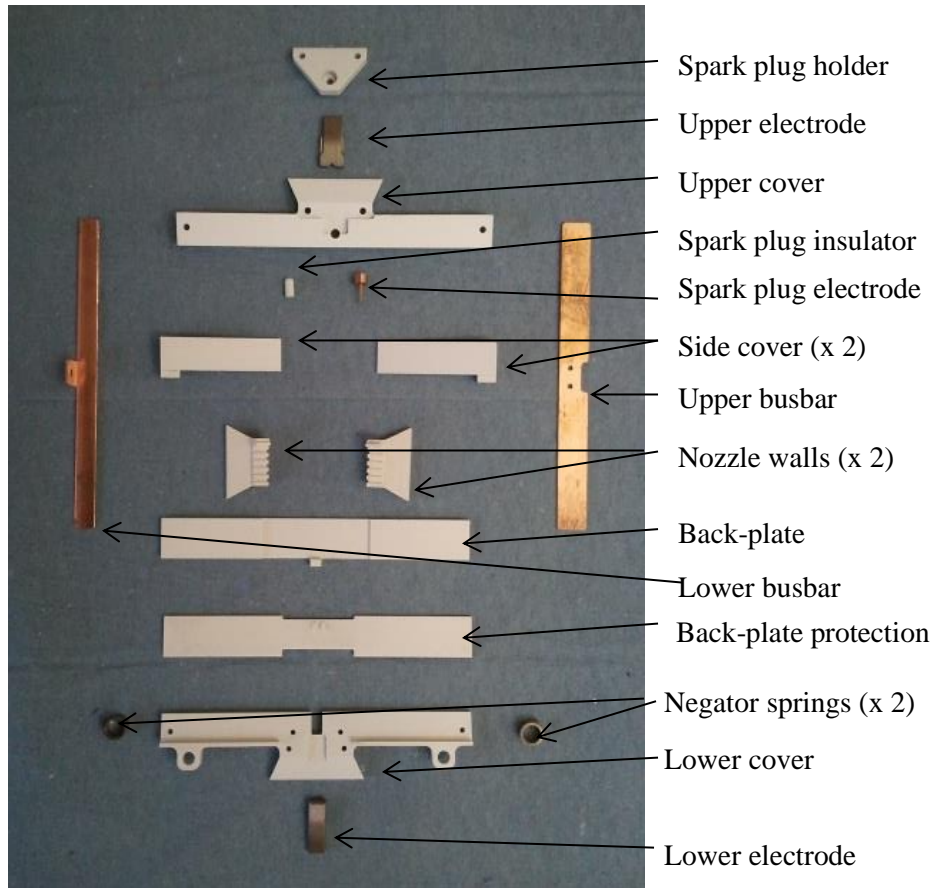


Figure 3-30 – PPTCUP-QM discharge chamber main components

3.4.2. Electronic board

The QM conditioning electronics is based on the design of the high voltage (HV) board prototype board prototype produced by Clyde Space Ltd in the frame of a PPT study for nano-satellite applications [70].

The PPTCUP-QM board shown in Figure 3-31 has been specifically designed to charge the main capacitor bank, to trigger the main discharge and to provide synchronization between these processes and to match the tight mass and volume Cubesat budgets.

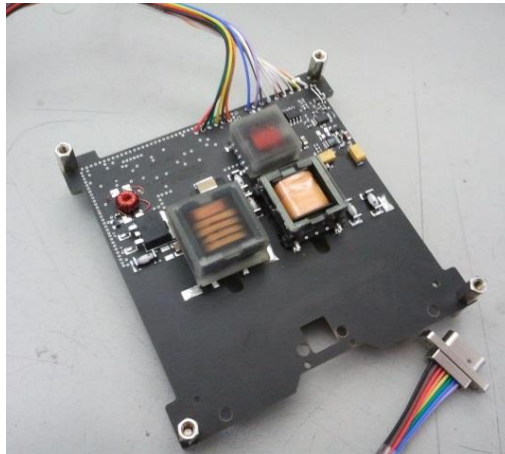


Figure 3-31 – PPTCUP-QM electronic board

It needs two dedicated lines: a + 3.3 V line for the digital circuit and a + 7.6 V line for the power. The low voltage (LV) ground (i.e. the reference ground of the board and of the power supply units) is connected to the earth ground; whereas the HV reference potential (i.e. the reference potential for the electrodes and spark plug potential) is left floating and insulated from the LV ground using optocouplers (Figure 3-32). The board can be remotely enabled and controlled. The communication protocol used is the I²C. The electronic board is conceptual similar to the GSE-2 shown in Figure 3-4. Further details of the electrical scheme cannot be presented because the intellectual properties belong to Clyde Space Ltd.

A 15 pins micro connector is used to electrically interface the unit with the GSE shown in Figure 3-3 when the unit is operated in a laboratory or with the rest of the satellite, if the unit is operated in space.

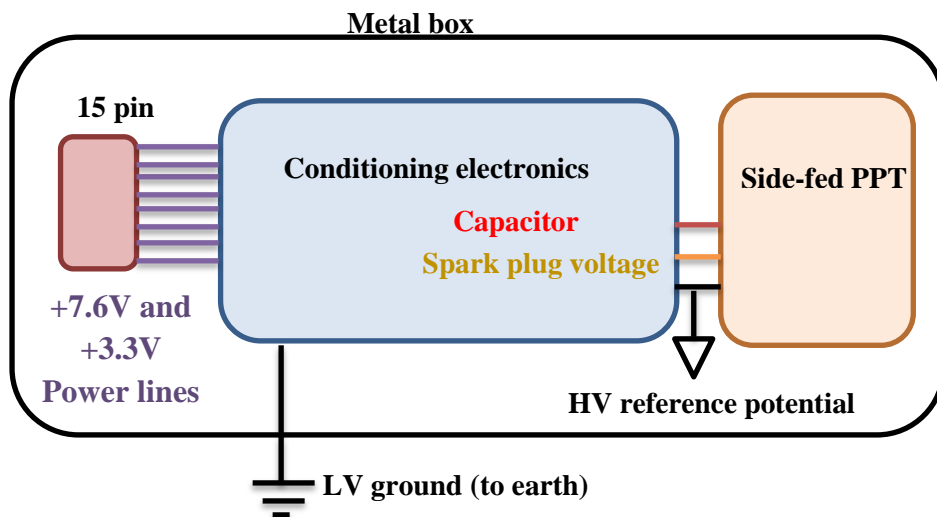


Figure 3-32 – PPTCUP-QM grounding scheme

3.4.3. External box

The external box has been introduced in the design to provide shielding from the noise radiated during the main discharge and assures that no arcing can occur between the thruster and the Cubesat systems, being insulated from the discharge chamber [88]. The main drawback might be the total weight of the unit since it is slightly heavier because of the mass of the external box that is about 70 g, i.e. the 26 % of the initial total mass.

The box, which is about 1 mm thick, is made of 6082-T6 aluminium alloy. Alocrom 1200 was chosen as final surface finish treatment to protect the box from corrosion. A complete structural analysis has been performed to find the lightest design that can sustain the typical loads in a Cubesat mission without permanent deformations, provide enough stiffness to the whole structure and avoid mechanical resonance coupling, having the natural oscillation frequency of the box to be compliant with the Cubesat requirements (i.e. $f_{nat} > 150$ Hz).

3.5. Spark plug insulator samples

As explained in §2.2.3, a dedicated study on the spark plugs to use on PPT for miniaturized satellite applications has been carried out in parallel to the development of the PPTCUP. Different spark plug insulators have been manufactured and then tested to find the best configuration that can withstand the PPTs lifetime and reduce the spark plug breakdown voltage.

The best spark plug configuration is then defined by these two requirements. Indeed, to match the lifetime requirement is an absolute because a failure in the spark plug system causes the failure of the whole propulsion system; indeed it represents the first criterion of choice of the spark plug configuration. The second requirement, i.e. the reduction of the spark plug breakdown, is the figure of merit of a certain spark plug configuration, which already proved its lifetime. The lower the breakdown voltage is, the better that spark plug configuration is.

The reduction of the spark plug breakdown voltage can be achieved by depositing a layer of semiconductor or metal on the spark plug insulator surface exposed to the main discharge. This has been found from the analysis of previous works on coated igniters (§2.2.2.2) and from the discussion about their possible applications on PPT spark plugs for miniaturized satellites applications (§2.2.3). The coated spark plugs could not always be tested on the PPTCUP. The PPTCUP-QM has a well-defined design that cannot be changed during the testing. On the other hand, the PPTCUP-EM design can be changed and, as mentioned above, the module has been used to test the lifetime of spark plug insulators of different materials. However it has to be

noticed that the coated spark plugs could not be tested when the PPTCUP-EM was driven by its dedicated electronic board that delivers a fixed value of voltage to apply to the spark plug (i.e. about 7.5 kV). Therefore, the testing of the spark plugs working at lower voltages has been carried out using the PPTCUP-EM, when not fed by its electronic board, or using another PPT for nano-satellite applications, called NanoPPT. More details about the NanoPPT design process and its measured performances are reported in ANNEX A. The geometry of the NanoPPT spark plug is shown in Figure 3-34. By comparing the geometries of the PPTCUP and NanoPPT spark plugs insulators (i.e. respectively Figure 3-33 and Figure 3-34), it can be noticed that the shape and the dimension of the surface exposed to the main discharge is exactly the same, being a ring with the inner and outer diameters of 0.7 and 1.4 mm. Therefore, the resistance of a thin layer of whatever material deposited on these insulators can be calculated using the second Ohm's law:

$$R = \int_{r_{in}}^{r_{out}} \frac{\rho}{2\pi\delta_{coat}r} dr = \frac{\rho}{2\pi\delta_{coat}} \ln\left(\frac{r_{out}}{r_{in}}\right) = \frac{\rho}{2\pi\delta_{coat}} \ln(2) \quad (80)$$

where δ_{coat} is the layer thickness and ρ the resistivity of the material.

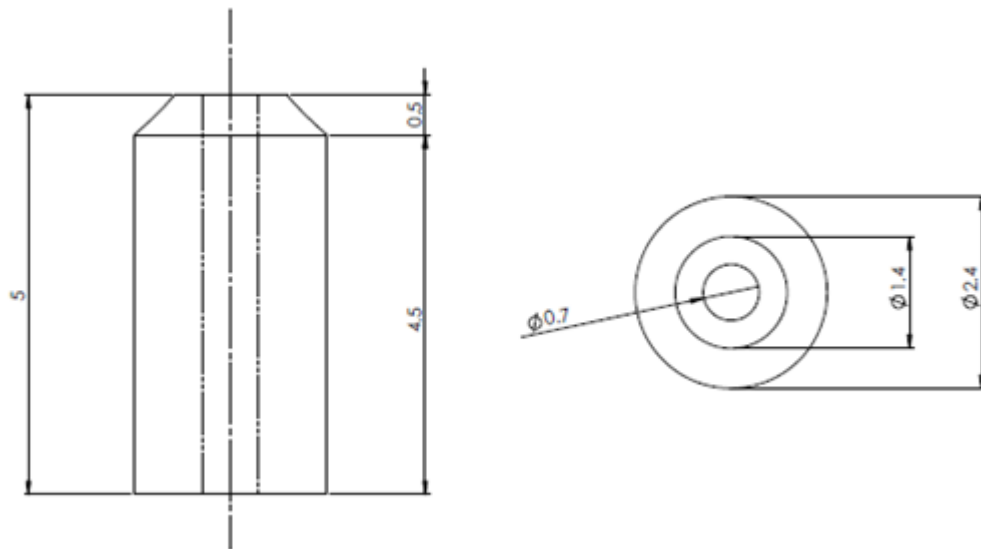


Figure 3-33 – PPTCUP spark plug insulator geometry. Dimensions are in mm.

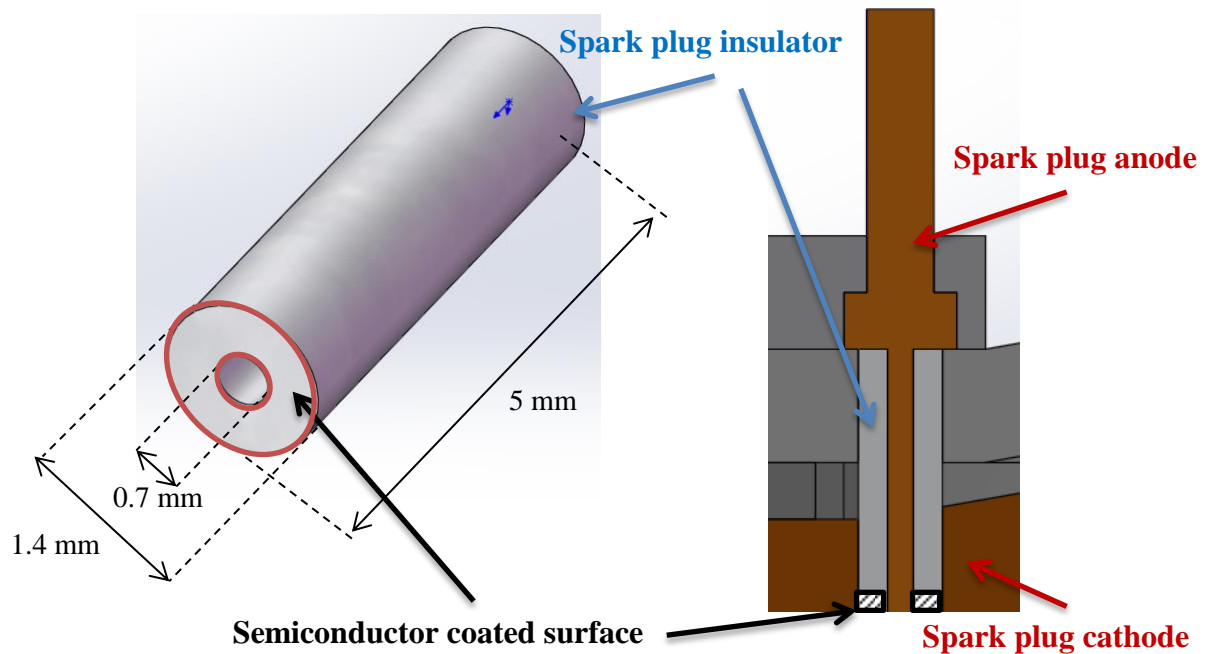


Figure 3-34 – NanoPPT spark plug insulator geometry.

The deposition of the semiconductor has been done using the equipment available at the UoS. Germanium and silicon were chosen among the semiconductors and deposited using the PECVD technique as explained in §2.2.3.1.

Table 3-4 summarizes the spark plug insulators that have been manufactured and tested. Test samples are shown in Figure 3-35.

Table 3-4 – Tested spark plug insulators

Bulk material	Coating
PTFE	a-Ge:H
	a-Si:H
Macor	a-Ge:H
	a-Si:H

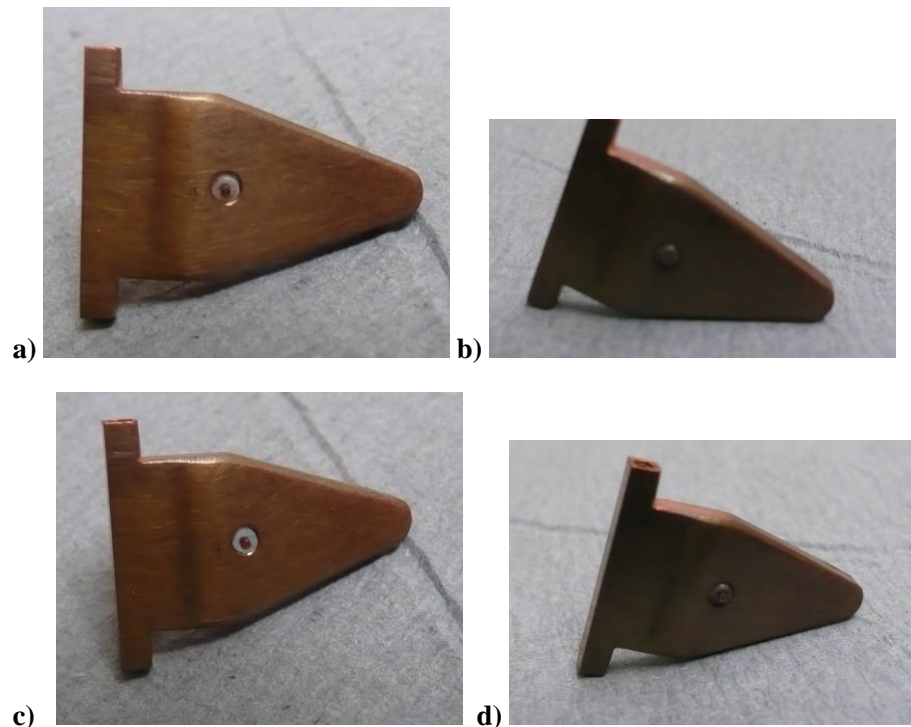


Figure 3-35 – Tested spark plugs: a) PTFE and a-Ge:H, b) PTFE and a-Si:H, c) Macor and a-Ge:H, d) Macor and a-Si:H

For what concerns the metal deposition, in §2.2.3.2 it has been discussed that, considering the deposition equipment capabilities and the mechanical properties of the metal [63], only titanium and gold can be chosen. However, as described in the relevant literature [59], [63], [65], [66], [67], [82], the thin metal layer has to have an equivalent resistance in the range between 1 and 1000 Ω . Therefore, for equation (80) and for the typical resistivity value ($\rho_{Ti} = 5.6 \cdot 10^{-7} \Omega\text{m}$, $\rho_{Au} = 2.2 \cdot 10^{-8} \Omega\text{m}$), a layer of a thickness of the order of some tens of nm would have an equivalent resistance of few Ω using Ti or fraction of Ω using Au. Since the Au layer resistance would be out of the range reported in the literature, titanium represents the best choice as material to deposit on the spark plug insulators.

Chapter 4. Experimental test campaigns results

4.1. PPTCUP experimental testing overview

Even if it based on a breadboard module, the design of space-flight qualified PPT discharge chamber needed an intermediate step to demonstrate its lifetime requirements. As mentioned in §3, the PPTCUP engineering model discharge chamber was manufactured and tested before the development of the final qualification model.

The entire process of analysis of the lifetime and optimization of the design to allow the PPT to deliver the best performance whilst keeping lifetime long enough to fulfil the mission requirements can be divided in four phases. As shown in Figure 4-1, the engineering model (i.e. PPTCUP-EM) was tested during the first two phases, whereas the qualification model (i.e. PPTCUP-QM) was tested during the last two phases.

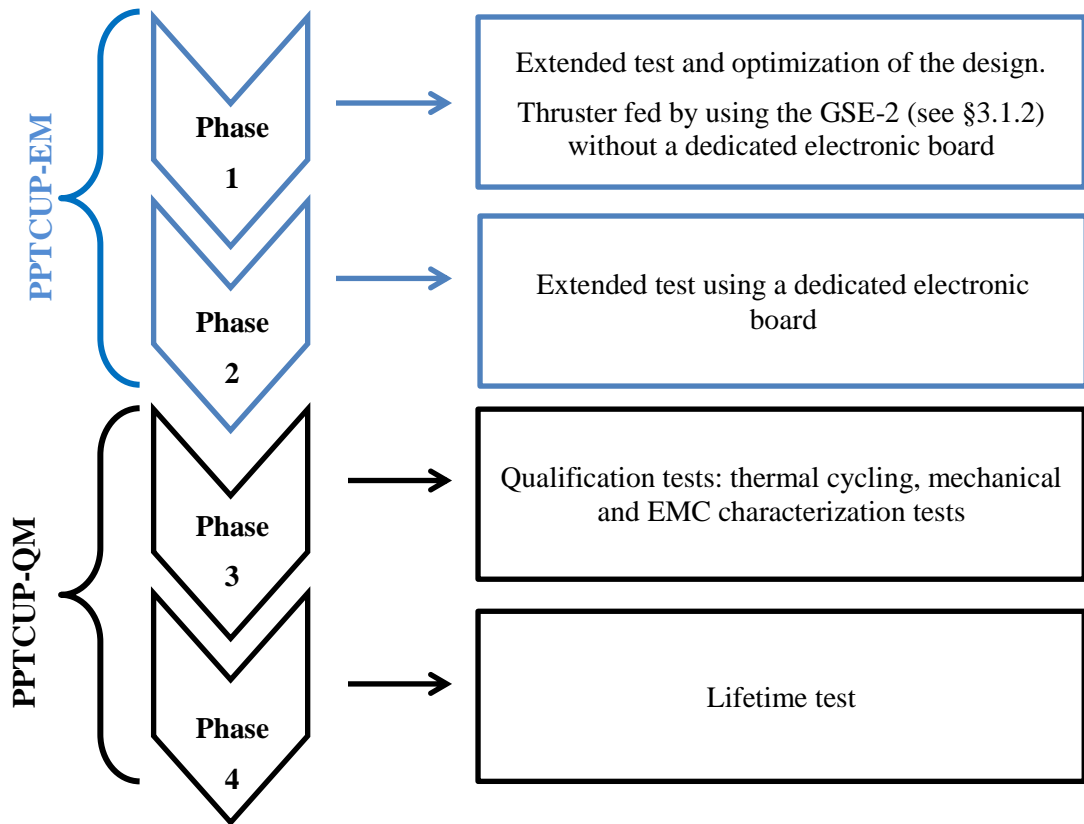


Figure 4-1 – PPTCUP test campaign sequence.

In the first phase of the experimental test campaign, the PPTCUP-EM was fed by the dedicated GSE-2 described in §3.1.2. The test was focused on the evaluation of the I_{bit} , m_{bit} , I_{sp} and η_{th} during the entire thruster lifetime. At the end of the test, once known the accurate thruster performance and its evolution during lifetime, it was possible to calculate the exact number of shots that the thruster can perform (n_{shots}) given the available propellant mass and the I_T that can be delivered. The lifetime of PPTCUP-EM was quantified as the number of shots that are needed in order to deliver the required I_T of 44 Ns. Finally, during the test the position of the spark plug and the feeding configurations were changed to find the best configuration able to fulfil the lifetime requirement.

In the second phase, the PPTCUP-EM was driven by a dedicated high voltage board prototype produced by Clyde Space Ltd in the frame of the NanoPPT study (see ANNEX A). The board has the same architecture and overall design of the final PPTCUP-QM electronic board (Figure 3-31); hence they are identical from a functional and electrical point of view. Moreover, the grounding scheme is representative of the spacecraft grounding scheme. For these reason, the test was mainly focused on the demonstration of the electronic board lifetime and reliability and on the preliminary characterization of the noise produced during the main discharge

Using the results from the first two test phases, the final design of the PPTCUP-QM was defined and the unit was manufactured. Then, in the third phase of the test, the PPTCUP-QM underwent a complete EMC characterization test that was carried out according to the NASA EMC standards environmental tests. The performances in terms of I_{bit} , m_{bit} , I_{sp} and η_{th} have also been measured. Finally, the unit underwent space-environment tests, i.e. a thermal cycling test to verify if the unit can work correctly in the range of the operating temperature and a mechanical test to demonstrate that the unit can survive the typical launch vibrations. Results of these latter tests are reported in ANNEX B.

The fourth and final phase consists of an extended test that needs to run until the module end-of-life is reached. The aims are the verification of the reliability of the system and the measurement of the total impulse (I_T) that the unit can deliver.

Unfortunately, the three years available for this research programme have not been enough to run two entire lifetime testing and, at the time of the writing, the PPTCUP-QM lifetime testing is still ongoing. Nevertheless, the complete results of the PPTCUP-EM lifetime testing are available and they are reported and discussed in this chapter.

4.2. PPTCUP performances

As explained in §4.1, the performances of the PPTCUP-EM and QM have been measured during the test campaign. Tests were focused on the evaluation of the impulse bit, propellant mass consumption, specific impulse and efficiency and on the electrical characterization of the thruster, i.e. the evaluation of the discharge current and voltage.

The diagnostics used to acquire all these data is fully explained in §3.2. Nevertheless, two key points about the data reported in the next sections need to be clarified:

- The m_{bit} and the I_{bit} were respectively measured using the mass scale described in §3.2.2 and the micro-torsional thrust balance described in §3.2.3. The specific impulse I_{sp} is defined as:

$$I_{sp} = \frac{u_e}{g_0} \quad (81)$$

where g_0 is standard gravitational acceleration ($g_0 = 9.81 \text{ m/s}^2$). Combining equation (23) and (81) yields:

$$I_{sp} = \frac{I_{bit}}{2m_{bit}g_0} \quad (82)$$

Therefore, once the m_{bit} and the I_{bit} and their uncertainties δm_{bit} and δI_{bit} are known, the I_{sp} and η_{th} are calculated using equations (32) and (82). Since I_{bit} , m_{bit} and E are independently measured, the relative errors of I_{sp} and η_{th} are calculated with the following equations [100]:

$$\frac{\delta I_{sp}}{I_{sp}} = \sqrt{\left(\frac{\delta I_{bit}}{I_{bit}}\right)^2 + \left(\frac{\delta m_{bit}}{m_{bit}}\right)^2} \quad (83)$$

$$\frac{\delta \eta_{th}}{\eta_{th}} = \sqrt{2 \cdot \left(\frac{\delta I_{bit}}{I_{bit}}\right)^2 + \left(\frac{\delta m_{bit}}{m_{bit}}\right)^2 + \left(\frac{\delta E}{E}\right)^2} \quad (84)$$

- The current parameter, ψ , is calculated from the discharge current I derived from the acquired discharge voltage, as described in §3.2.1. Nevertheless, ψ can also be calculated by directly measuring the current I using a dedicated Rogowski coil and then applying equation (25). The calculation from this second approach is more accurate because it does not require a numerical fitting of the data. However, in the PPTCUP design it is necessary to detach the capacitor bank from the backplate of the PPT in order to fit the Rogowski coil and to do the measurements. In this “modified” configuration, the inductance L of the equivalent PPT RLC circuit (Figure 2-25) increases and the current parameter decreases according to equation (42). Moreover, since it has been found that the current parameter ψ is proportional to the I_{bit} and the m_{bit} [1], [3], [20], [107], [108], an increase of the inductance L causes the decrease of the overall thruster performances. Finally, if the PPT under testing is a qualification model, like the PPTCUP-QM, it is very likely that the design is fixed and optimized for delivering the best performance and the Rogowski coils cannot be inserted and used. For these reasons, during the experimental tests carried out for this study, the Rogowski coil has been used only at the first stage of the PPTCUP-EM testing to verify the thruster functionality.

4.2.1. PPTCUP-EM: influence of spark position on performance

At the beginning of the phase one, the PPTCUP-EM has been tested in both spark plug configurations, as described in §3.3.5. During this test, in which the propellant was in the classic side-fed configuration, a total of about 3,000 shots were performed.

Figure 4-2 shows the comparison of the current and voltage curves for the two tested configurations. The curves have been obtained averaging the data of twelve different shots in each configuration. The curves are very similar for the two spark plug positions and show a trend that resembles the one that characterizes the PPTCUP-BB [4], [105] (Figure 4-3). The voltage and the current measurement were also noticed to be very repeatable with a standard deviation of the first positive peak of the current curve respectively of 0.77% and 0.41% for the *Far* and *Close Hole*

configurations and a standard deviation of the first negative voltage peak of about 3.6 % and 3.0%.

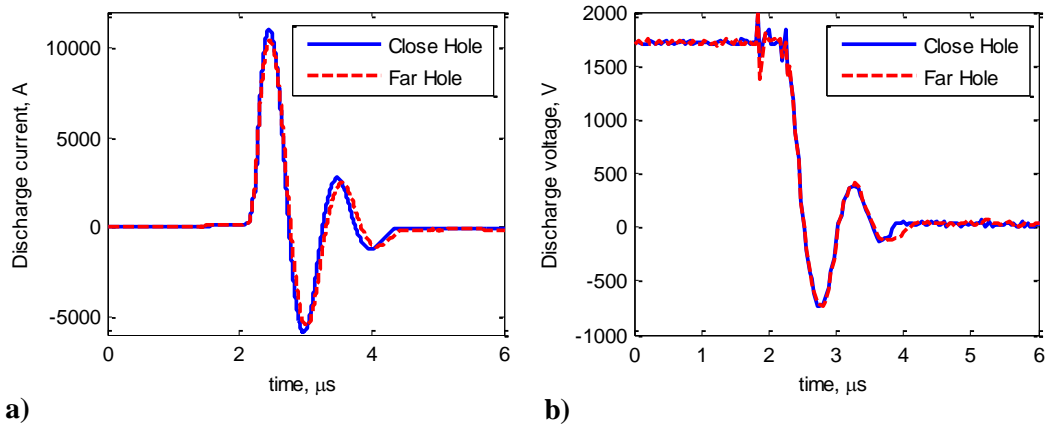


Figure 4-2 - Comparison of the typical a) discharge current curves and b) discharge voltage curves for different spark plug positions (phase 1). Side-fed configuration.

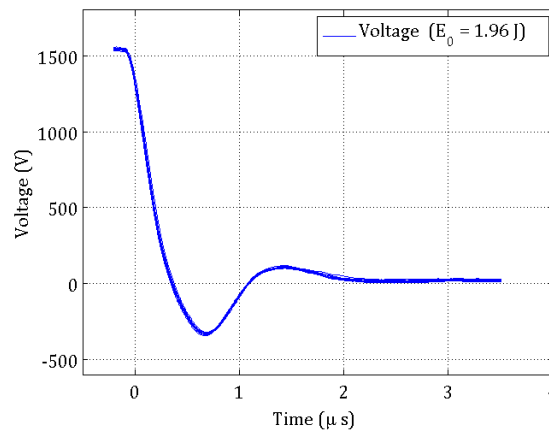


Figure 4-3 – Typical PPTCUP-BB discharge voltage curve [105].

The thruster performances for the two configurations are reported in Table 4-1. The I_{bit} and m_{bit} values and their uncertainties have been measured using the thrust balance and the mass scale described in §3.2.3 and 3.2.2. The I_{sp} and η_{th} are derived using equations (82) and (32), whereas their uncertainties are calculated using equations (83) and (84). These data show that, even if the spark plug position does not significantly affect the impulse bit value, the mass consumption is reduced by about 13.5% when the *Close Hole* configuration is used. According to these results, this configuration is characterized by a higher specific impulse and efficiency and, for same number of shots, higher total impulse.

Table 4-1 - Comparison of the different spark plug positions performances. Side-fed configuration.

Parameter	Far Hole	Close Hole
I_{bit} [μ Ns]	37.8 ± 3.3	38.2 ± 3.4
m_{bit} [μ g]	7.4 ± 0.1	6.4 ± 0.1
I_{sp} [s]	521 ± 46	608 ± 55
η_{th} [%]	4.8 ± 0.6	5.7 ± 0.7

4.2.2. PPTCUP-EM: propellant feeding performance influence

From the results obtained in the analysis of the spark plug position influence on the PPT performance, the best position for the spark plug is the *Close Hole*, i.e. the at the breech of the cathode and close to the capacitor bank. Thus, the analysis of the influence of the propellant feeding configuration on the PPT performance was performed with the spark plug electrode mounted in the *Close Hole*.

During the test to assess the propellant feeding influence, both the side-fed and the V-fed configurations have been tested using two pairs of suitable propellant bars. A second aim of the test was the verification of the discharge chamber lifetime, quantified as the total number of shots that the thruster can perform until all the total impulse is delivered or until a failure occurs. According to the performance measured during the PPTCUP-BB characterization and considering its mission requirement of delivering an $I_T = 44$ Ns [3] [4], the PPTCUP should fire at least one million time (as order of magnitude). For this reason, each propellant feeding configuration performed about 500,000 shots. Finally, in order to have a more statistic-relevant data, each configuration was set twice, as shown in Figure 4-4.

Their performance has been acquired throughout the test and their mean values are reported in Table 4-2. As for the data shown in Table 4-1, the I_{bit} and m_{bit} values and their uncertainties have been measured using the thrust balance and the mass scale described in §3.2.3 and 3.2.2. The I_{sp} and η_{th} are derived using equations (82) and (32), whereas their uncertainties are calculated using equations (83) and (84).

The measured data show that the choice of the feeding configuration significantly influences the thruster performance. In the side-fed configuration the combination of the I_{bit} and the m_{bit} leads to an I_{sp} that is 27% higher than the one calculated on the V-fed. On the other hand, the V-fed configuration is characterized by an I_{bit} which is about 24% higher. In the end, the combination of these different values of the I_{bit} and the I_{sp} leads to the same value of η_{th} (within the error bars) in both the feeding configurations.

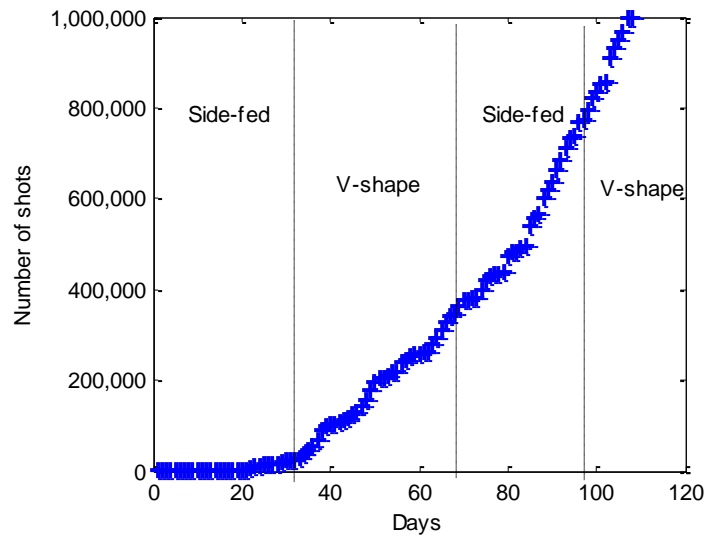


Figure 4-4 – PPTCUP-EM driven shot counter (phase 1)

Table 4-2 - Comparison of the different propellant bars configuration. Spark plug in the *Close Hole*.

Parameter	Side-fed	V-fed
I_{bit} [μ Ns]	38.2 ± 3.4	50.3 ± 4.4
m_{bit} [μ g]	6.4 ± 0.1	10.7 ± 0.1
I_{sp} [s]	608 ± 55	480 ± 42
η_{th} [%]	5.7 ± 0.7	5.9 ± 0.7

An analysis of the possible performance decay during the PPTCUP-EM lifetime has also been performed during the phase 1 of the test campaign. Figure 4-5 shows the impulse bit measurements for both feeding configurations against the number of performed shots. PPTCUP-EM does not seem to be affected by any performances decay during its lifetime; since the value of m_{bit} measured throughout the test campaign did not show any appreciable change, it can be concluded that also the value of I_{sp} and η_{th} stayed constant during the thruster lifetime, within the relative uncertainties. This is an important design improvement, as different authors [109], [110] have experienced a significant decay in I_{bit} (up to 65 % of decrease) during the lifetime of their PPTs, as shown in Figure 4-6.

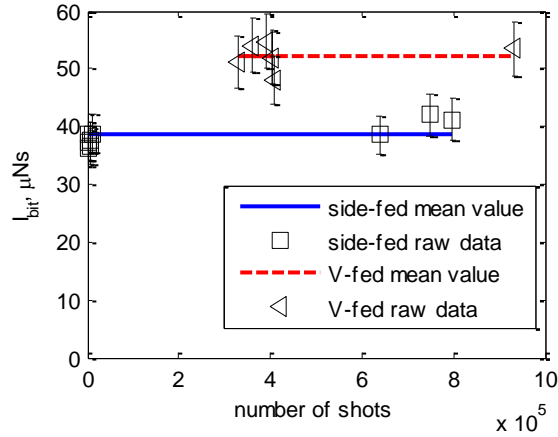


Figure 4-5 – PPTCUP-EM I_{bit} measurements (phase 1).

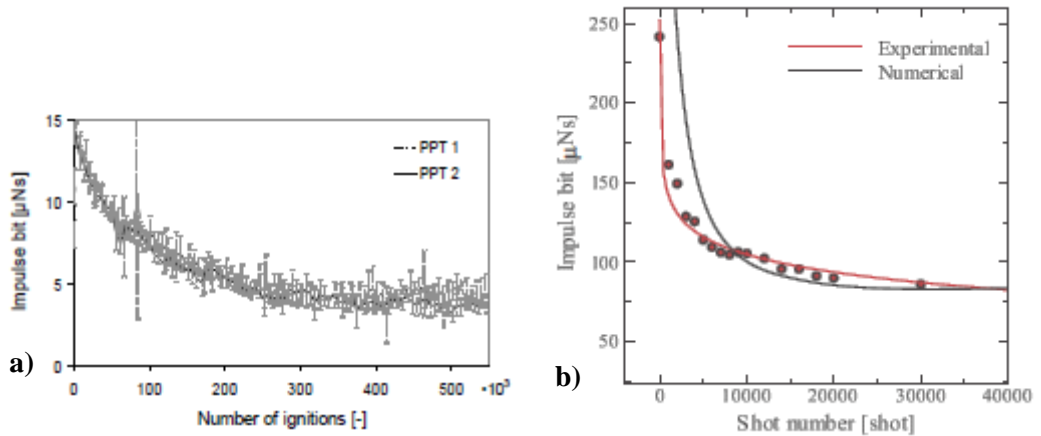


Figure 4-6 - Examples of typical PPT performances decay a) from [109] b) from [110]

Using the averaged data shown in Table 4-2, it is possible to evaluate the I_T that both feeding configurations can deliver. Assuming that only the 90% of the total stored propellant mass is used during the thruster lifetime [3], the number of available shots n_{shots} is by definition:

$$n_{shots} = \frac{\beta_{mass} \cdot M_{prop}}{m_{bit}} \quad (85)$$

where $\beta_{mass} = 0.9$ is the mass consumption margin.

Once n_{shots} is known, I_T can be calculated as follow:

$$I_T = n_{shots} \cdot I_{bit} = \beta_{mass} \cdot M_{prop} \cdot I_{sp} \cdot g_0 \quad (86)$$

where the last identity is derived using equations (82) and (85).

The values of n_{shots} and I_T evaluated with equations (85) and (86) for both the feeding configurations are summarized in Table 4-3, where the uncertainties have been calculated according to [100].

Table 4-3 – PPTCUP-EM total impulse capability

	Side-fed	V-fed
n_{shots}	1,124,000 ± 18,000	674,000 ± 6,500
I_T [Ns]	42.9 ± 3.9	33.9 ± 3.1

From the data shown in Table 4-2 and Table 4-3, the side-fed configuration with the spark plug placed in the *Close Hole* showed the best performances in terms of I_{sp} and I_T . Thus, the PPTCUP-QM was designed and manufactured in this “optimized” configuration.

Further and different tests and analysis (e.g. the environment and the EMC tests) were performed to verify if this configuration is the best PPT design not only for the deliverable performance but also for the optimization of the PPT as a sub-system to be integrated into a satellite spacecraft.

4.2.3. PPTCUP-EM: electronic board prototype performance influence

After the end of the first stage of the test campaign, the PPTCUP-EM was re-assembled in the side-fed configuration using new PTFE propellant bars and connected to the dedicated electronic board that was produced in the frame of the NanoPPT study (Figure 4-8). As reported §3.1.2, the grounding schemes in the second phase of test campaign was different from the one used during the previous phase, because the reference potential of the PPT was kept insulated from the LV ground using optocouplers.

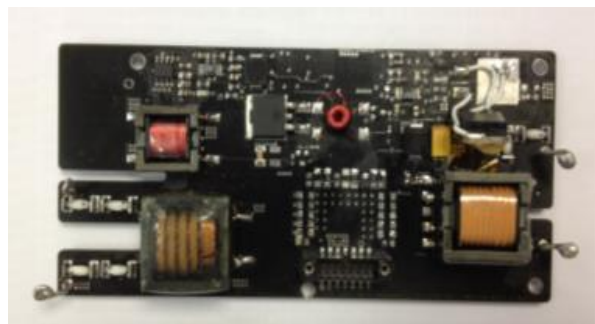


Figure 4-7 – HV board prototype used during the phase 2 of the experimental test campaign.

The first 500 discharge voltage curves have been acquired to verify the repeatability of the board operations. The discharge voltage measurements were noticed to be

very repeatable with a standard deviation of the first negative peak of the discharge voltage curves of 0.93%. An example of comparison among three different discharge voltage curves is shown in Figure 4-8. As expected, the acquired curves also show a trend that very closely resembles the one found during the previous phase (see §4.2.1).

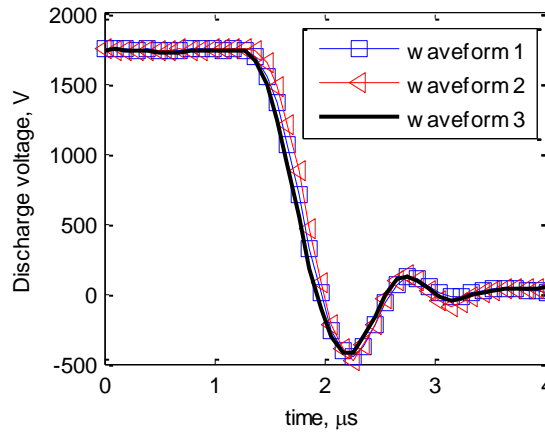


Figure 4-8 – PPTCUP-EM discharge voltage curve when powered by the HV board (phase 2).

Then, the extended test was run performing a shot every 1.5 s and checking the functionality of the board. More than 800,000 shots were completed and both the thruster and the electronics were still operational. It has to be noticed that at the end of the phase 2, the PPTCUP-EM discharge chamber performed about 1,800,000 shots, hence exceeding of about 60% the required lifetime for the side-fed configuration, i.e. about 1,124,000 shots as shown in Table 4-3.

The thruster performances in terms of I_{bit} , m_{bit} , I_{sp} and η_{th} could not be measured during this phase because of the time availability of the facility. However, it has to be noticed that test phase 2 was mainly focused on the demonstration of the electronic board lifetime and reliability, which was successfully accomplished indeed, rather than assess the thruster performance, which has been done in all the other phases of the test.

4.2.4. PPTCUP-QM performance characterization

In the third phase of the test, the PPTCUP-QM performances were checked after the end of the environment tests (i.e. thermal cycling, mechanical and EMC tests) to verify that no damages and/or failures occurred in the unit. Figure 4-9 shows an example of comparison of the voltage curves acquired during phase 3. The curves are very similar and show that the main discharge expires in about 2 μ s. The voltage measurements were also noticed to be very repeatable with a standard deviation of the first negative voltage peak of about 1%. The only appreciable difference is the

level of the noise induced by the spark plug on the capacitor line during the discharge initiation that during every shot has changed within a range of ± 500 V peak-to-peak.

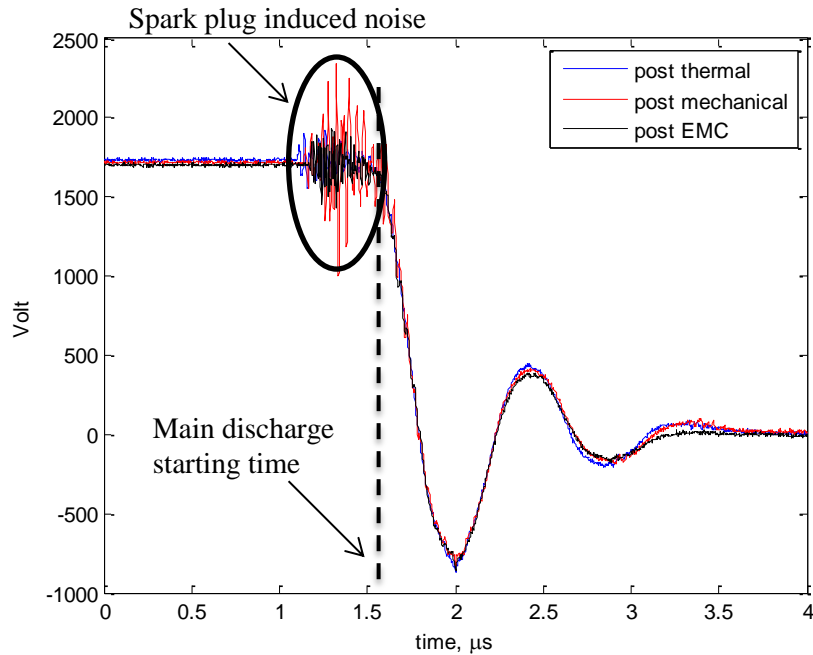


Figure 4-9 – PPTCUP-QM discharge voltage comparison (phase 3)

The PPTCUP-QM performances are summarized in Table 4-4, together with the equivalent RLC electrical parameters (i.e. the equivalent average R and L during the PPT main discharge) derived by fitting the PPT discharge curve with equation (40) and using the known value of C . The discharge voltage curve shown in Figure 4-10 and used for the fitting was obtained averaging the data of ten different shots after the end of the EMC testing and immediately before the start of phase 4 (i.e. PPTCUP-QM lifetime testing). As for the previous test phases, the I_{bit} and m_{bit} values and their uncertainties have been measured using the thrust balance and the mass scale described in §3.2.3 and 3.2.2. The I_{sp} and η_{th} are derived using equations (82) and (32), whereas their uncertainties are calculated using equations (83) and (84).

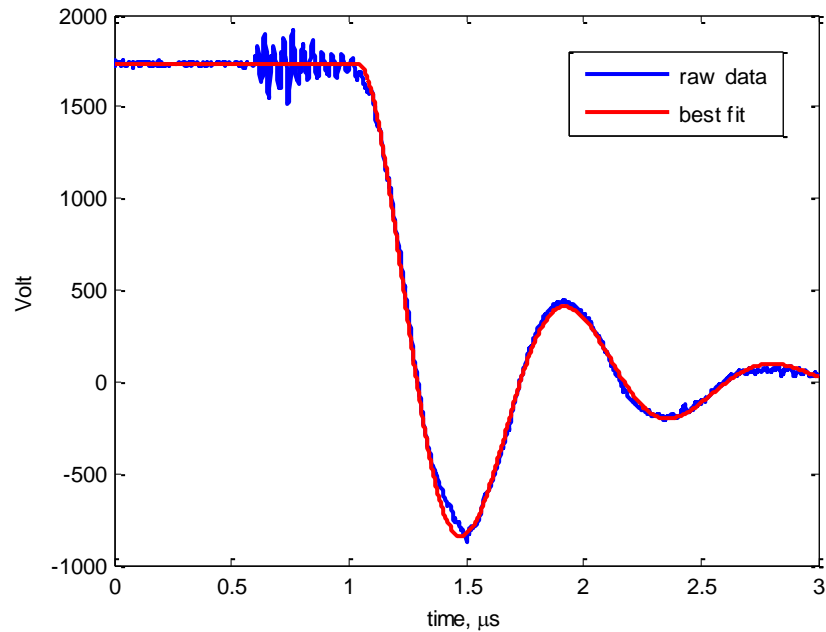


Figure 4-10 - Discharge voltage fitting

Table 4-4 – PPTCUP-QM electrical parameters and performance summary

Parameter	Value	Parameter	Value
E_0 [J]	2.01	I_{bit} [μNs]	40.0 ± 3.5
R^* [$\text{m}\Omega$]	45	m_{bit} [μg]	5.9 ± 0.1
L^* [nH]	13.8	I_{sp} [s]	696 ± 62
ψ^* [A^2s]	45.3	η_{th} [%]	6.8 ± 0.9

* evaluated from the discharge voltage waveforms fitting

From the measured data, the impulse bit over initial energy ratio I_{bit}/E_0 is $20.0 \pm 1.8 \mu\text{Ns/J}$ and this is in line with the typical value that characterizes side-fed PPTs (see Table 2-2).

Since the PPTCUP design includes a nozzle, it can be reasonably affirmed that the thrust, hence the I_{bit} , is both due to the electromagnetic force generated during the discharge and to the expansion of the plume of ablated propellant in nozzle.

Experimental results from the PPTCUP-BB testing [3] and data measured with other thrusters at similar energy level [1], [7], [20], [111], [112] indicate that the electromagnetic impulse bit ($I_{bit_{EM}}$) accounts for about 30 to 45% of the total I_{bit} .

Assuming that this range is valid for the PPTCUP-QM and taking into account the measured I_{bit} reported in Table 4-4, the estimated $I_{bit_{EM}}$ delivered by the PPTCUP-QM is in the range between 12 and 18 μNs . From these values, it is possible to calculate the inductance per unit of length L' using equation (24) that is has been

derived from the conservation of the momentum of the current sheet and neglecting the electro-thermal component of thrust (see §2.3.2).

Many theoretical and experimental studies regarding the PPT functioning confirmed that PPT performance depends on the value of L' . In particular, it has been found that the geometry of the electrodes (i.e. the electrode length d_{el} , width w and thickness τ and the electrode spacing h) strongly affect the value of the inductance per unit of length [20], [91] [93].

For electrodes aspect ratios h/w of the same order of magnitude of the PPTCUP electrode aspect ratio (i.e. about 2), L' can be calculated using equation (22) and here below reported for convenience:

$$L' = 6 + 4 \cdot \ln\left(\frac{h}{w+\tau}\right) \quad [\text{nH/cm}] \quad (22)$$

Using the PPTCUP electrodes dimensions (see §3.3.1), L' predicted by equation (22) is 7.4 nH/cm. Since the mean values of L' derived from the knowledge of the $Ibit_{EM}$ are in the range between 5.3 and 7.9 nH/cm and in agreement with the theoretical value, the hypothesis that the electromagnetic impulse bit delivered by the PPTCUP-QM accounts for about 30 to 45% of the total $Ibit$ appears valid.

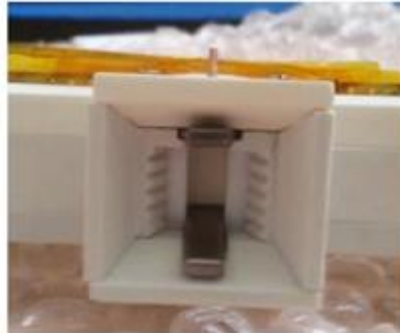
Finally, since $L' = 7.4$ nH/cm and the length of the electrodes is about 1.5 cm, the variation of the inductance during the discharge has the same order of magnitude of the average value of $L = 13.4$ nH shown in Table 4-4. Though, as shown in Figure 4-10, the fitting is good. This is likely due to the fact that also the resistance and the capacitance are not constants and change during the discharge. Therefore, for the combined effect of the electrical parameters time-variations, the natural frequency and the damping ratio, which depend on C, L and R (see equations (36) and (37)), are in good agreement with the characteristics of the measured discharge curve.

4.3. Carbonization and propellant charring

During the phase 1 of the experimental test campaign, visual inspections of the PPTCUP-EM discharge chamber have been carried out to monitor the carbonization phenomenon and the propellant bar charring.

Figure 4-11 shows the growth of the layer of carbon that has been progressively deposited on the discharge chamber and nozzle walls and on the electrodes surface throughout the test. It can be noticed that the thruster is affected mainly by back plate and nozzle walls carbonization, where the Teflon vapour density is higher [29], [31]. Despite the growth of this layer, PPTCUP-EM did not show any kind of problem which could be related to the possible conductive path between the electrodes. Since the requested lifetime of the current device was achieved, it can be concluded that the updated thruster design, i.e. the introduction of the lateral grooves on the lateral nozzle walls and the back plate protection, has prevented the growth of a carbon layer big enough to short the electrodes hence causing the thruster failure.

The housing components at the end of the test campaign are displayed in Figure 4-12, Figure 4-13 and Figure 4-14.



EM discharge chamber at the beginning of the test campaign



After about 50,000 shots



After about 250,000 shots



After about 750,000 shots



After about 900,000 shots

Figure 4-11 - Details of the carbonization occurred in the PPTCUP-EM discharge chamber.

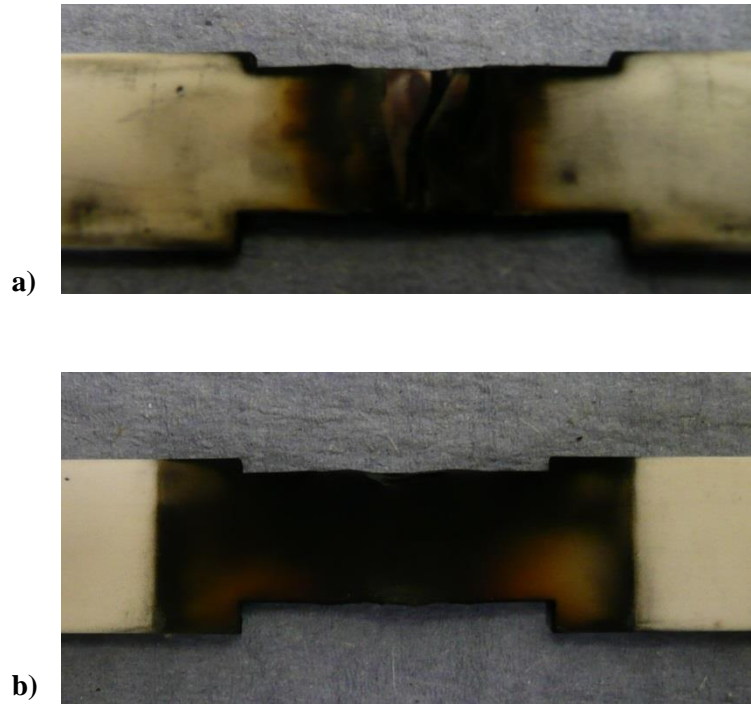


Figure 4-12 - Back plate protection at the end the test campaign (phase 1): a) discharge side
b) rear side.

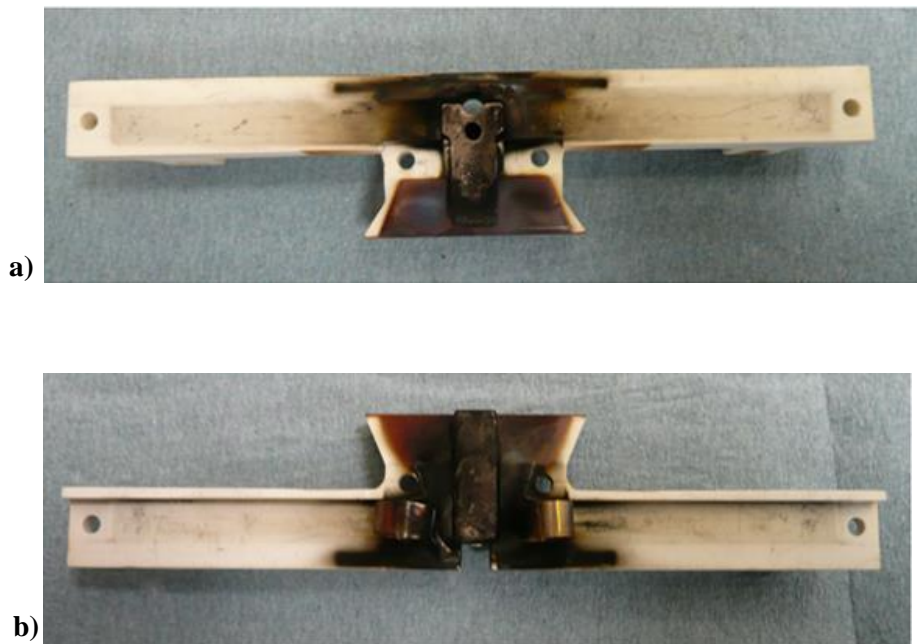


Figure 4-13 - a) Upper and b) Lower housing cover at the end the test campaign (phase 1).

Housing side walls



Spark plug holder



Nozzle lateral walls



Figure 4-14 - Housing components (discharge side) at the end the test campaign (phase 1).

Moreover, the electrodes have been scanned with an electron microscope (SEM) and the Energy Dispersive X-ray (EDX) spectroscopy performed on the surface exposed to the main discharge to confirm that the material deposited during the thruster lifetime is carbon. This analysis revealed that the surfaces appear to be covered by a carbon layer. Moreover, the carbon tends to deposit in the shape of single or cluster of globules, as shown in Figure 4-15. On the electrodes surface exposed to the main discharge, it has been found that the carbon layer gets thicker moving towards the end of both electrodes covering completely their divergent part, where it is clearly

visible a change of the surface aspect (Figure 4-16). However, the presence of this thin film is not only acceptable, but even desirable since, as reported in [29], it limits the electrode erosion because the carbon layer prevents the formation of large hot spots on the electrodes (minimizing sputtering and other wear out mechanisms).

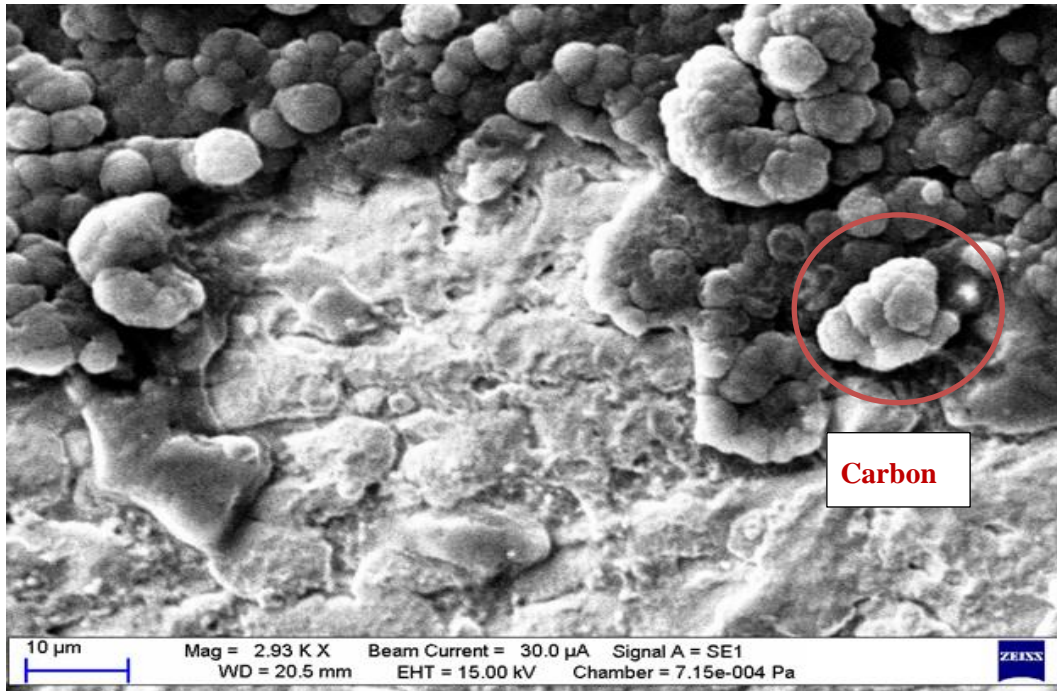


Figure 4-15 - SEM picture taken in the centre of divergent part of the cathode (discharge side) at the end the test campaign (phase 1).

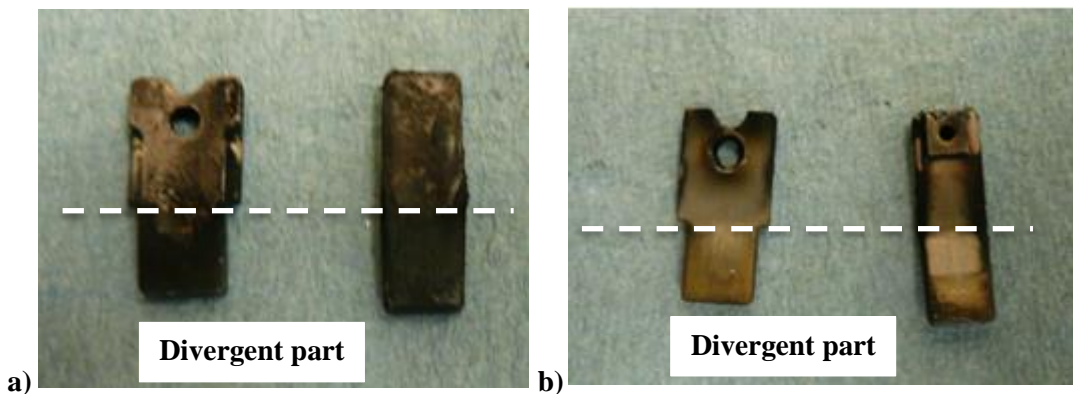


Figure 4-16 – PPTCUP-EM cathode (on the left) and anode at the end the test campaign (phase 1): a) discharge side b) rear side

It has to be noticed that these carbonization results are in agreement to what it has been found in other thruster characterization test campaigns [29], [30], [31] and summarized in § 2.2.2.1.

Regarding the propellant charring, all the investigated thruster configurations had shown a uniform consumption of the exposed propellant surface. Moreover, as

shown in Figure 4-17a, the propellant surface exposed to the main discharge appears clean and smooth, particularly if compared to the PPTCUP-BB propellant bars (Figure 4-17b) that appeared dirtier after only 3,000 shots performed at a lower initial voltage V_0 of about 1500 V [105]. The fact that the propellant ablation can be made more uniform increasing the initial voltage V_0 confirms what found by other authors [48] and [113]. The blackness around the edges shown in Figure 4-17a is carbon and it is due to the carbonization, since in a side-fed PPT that area of the propellant bars acts as an inner wall of the discharge chamber (Figure 4-11).

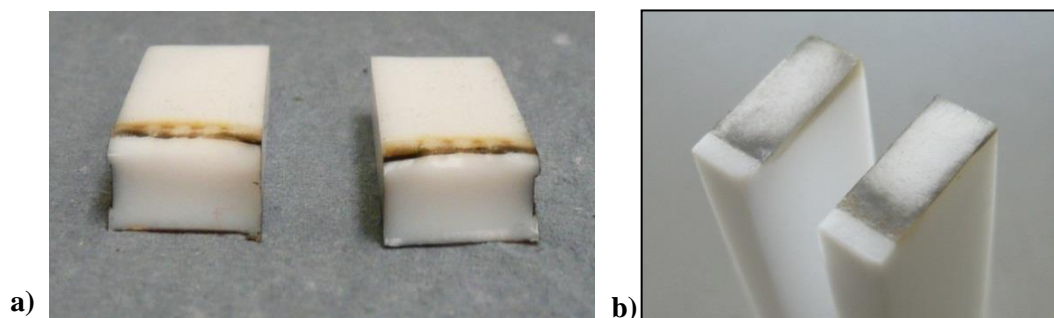


Figure 4-17 - PTFE propellant bars charring: a) side-fed PPTCUP-EM (after about 250,000 shots, phase 1), b) PPTCUP-BB (after about 3,000 shots) [105].

4.4. Electromagnetic noise interference

As mentioned in §2.1, a potential issue to be addressed for flight opportunities is the electromagnetic compatibility of the PPT with the spacecraft, because the electromagnetic noise that a PPT generates may cause failures not only on the PPT system itself but also on the other satellite subsystems.

During the development of the PPTCUP, the electromagnetic noise was preliminary analysed during the engineering model testing and then fully characterized during the qualification model testing. The results are reported and discussed in the following sections.

4.4.1. Noise characterization from the PPTCUP-EM testing

At the beginning of the phase 2 of the experimental test campaign and before the verification of the electronic board design reliability (see §4.2.3), a preliminary characterization of the noise generated by the unit has been carried out. This was possible because, when the electronic board manufactured by Clyde Space Ltd is used to command the PPTCUP-EM, the grounding scheme is representative of the ground connections in the spacecraft.

The electromagnetic noise produced by the thruster was evaluated acquiring the AC signal on the power lines between the test points shown in Figure 4-18 both during a complete thruster shot and during a single spark plug pulse only, i.e. firing only the spark plug without charging the capacitor bank. The noise test points were chosen because they are on the power lines that feed the thruster and hence representative of the position of the satellite in space.

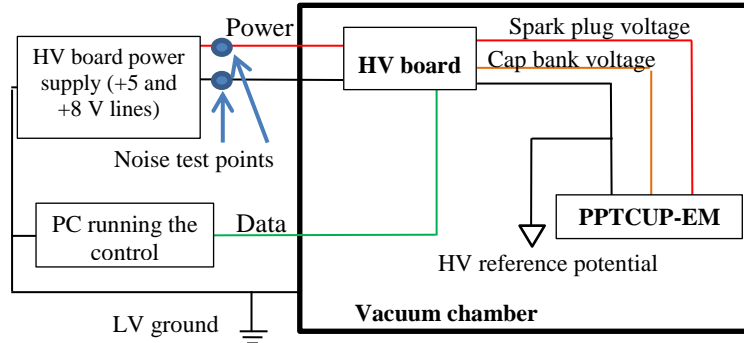


Figure 4-18 – PPTCUP-EM driven by HV board grounding scheme (phase 2)

The noise signals generated by the main discharge and by the only spark plug pulse are qualitatively similar and last for about 400 ns, starting from initiation of the spark plug pulse, as shown in Figure 4-19.

The RMS value of the noise signal during this interval of time (i.e. 400 ns) was calculated according to the RMS definition:

$$N_{RMS} = \sqrt{\frac{1}{\Gamma} \sum_{i=1}^{\Gamma} N_i^2} \quad (87)$$

where Γ is the total number of the noise signal samples N_i .

The measurements have been repeated 10 times for each test case (i.e. firing the thruster and firing the only spark plug) and the RMS values were averaged.

The results are reported in Table 4-5. Looking at these data, it can be noticed that the RSM noise does not seem to depend on the main discharge since the RMS values obtained for a complete and a spark plug shot are in close agreement (their difference is within the error bars). These results suggest that in PPTCUP-EM the main source of noise is the spark plug discharge rather than the main discharge.

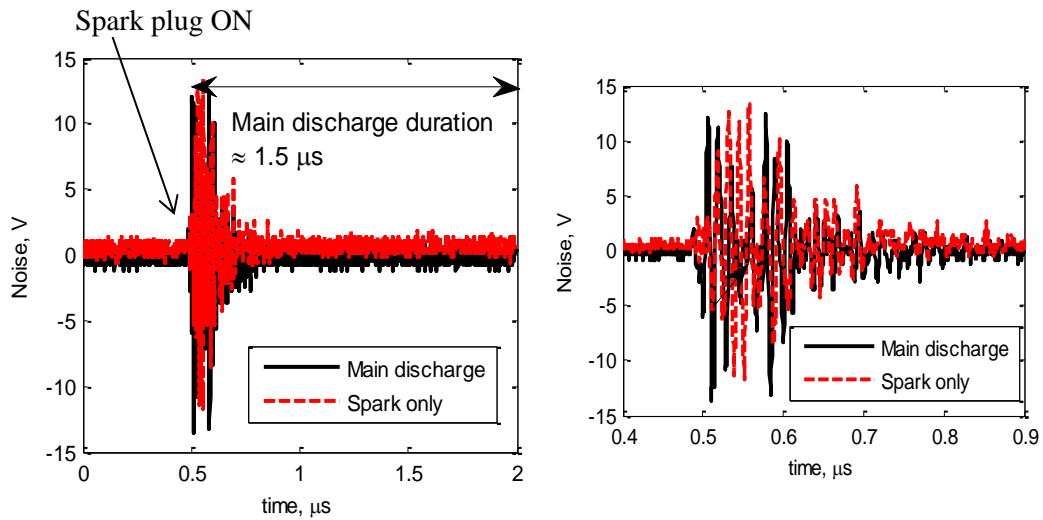


Figure 4-19 - Noise measurements for a thruster shot ($E = 2 \text{ J}$) and spark plug only shot measured on the power line.

Table 4-5 – RMS noise values

Capacitor bank voltage [V]	RSM value [V]
1720	2.72 ± 0.69
0 (spark plug pulse only)	2.76 ± 0.66

These conclusions about the main source of noise produced by a PPT are in line with the results of the electromagnetic interference (EMI) tests performed on different flight model PPTs in the past. Even if those PPTs worked at higher energy ($> 20 \text{ J}$ as summarized in [87]), they produced a noise that reached its peak before the main discharge starts, i.e. during the spark plug discharge [85], [86], as shown in Figure 2-22.

There is another possible proof that the spark pulse is the dominant source of noise. It is accepted that a PPT discharge can be modelled using a two-sources model [87], [114], which has already been proposed in the study of the electrostatic discharges in air [115]. During the discharge initiation, the equivalent circuit impedance is relatively high because the current is low and the electric fields are high. On the other hand, during the main discharge, the equivalent impedance is very low and from the PPTCUP RLC circuit analysis it has been found that the circuit impedance, including the arc impedance, is about $45 \text{ m}\Omega$ (Table 4-4). Since high impedance is characteristic of an electric dipole and low impedance is characteristic of a magnetic dipole, it is possible to assume that the spark plug discharge acts as an electric dipole, whereas the main discharge as a magnetic dipole [114].

The maximum magnitude of the noise emitted by an electric dipole (N_{el}) under vacuum condition can be expressed as [116]:

$$N_{el} = 6.3 \times 10^{-7} \frac{I_{el} \cdot L_{dip} \cdot f}{r} \quad (88)$$

Where I_{el} is the peak current, L_{dip} is the length of the dipole, f is the fundamental frequency of the signal and r is the distance of an observer from the dipole.

At the same time, the maximum noise emitted by a magnetic dipole (N_{mag}) under vacuum condition is given by [116]:

$$N_{mag} = 1.3 \times 10^{-14} \frac{I_{mag} \cdot D^2 \cdot f^2}{r} \quad (89)$$

Where I_{mag} is the peak current, D is the length of the dipole, f is the fundamental frequency of the signal and r is the distance of an observer from the dipole. N_{el} and N_{mag} have the dimensions of an electric field, i.e. V/m.

As shown in Figure 4-2, the typical PPTCUP peak current is about 10 kA. The fundamental frequency of the main discharge is about 0.7 MHz because the discharge voltage curves have a period of about 1.5 μ s, assuming them as the under-damped waveforms of a LRC oscillating circuit (see Figure 4-2 and Figure 4-9). On the other hand, the spark arc lasts in less than 10 ns, because it was not possible to acquire the spark plug signal using a HV probe with a bandwidth of 100 MHz. This means that the spark arc fundamental frequency is greater than 100 MHz and two orders of magnitude greater than the discharge frequency. During the PPTCUP experimental test campaign, the spark plug current has not been measured. However, it is accepted that PPT spark plug currents are typically of the order of 100 A [1], [114].

According to the two-source model, N_{el} and N_{mag} are respectively the noises generated by the PPT main discharge and spark plug. Their values, which are summarized in Table 4-6, have been calculated with equations (88) and (89) using the PPTCUP data. It is clear that the noise generated by the spark plug is more than two orders of magnitude greater than the one generated by the main discharge. This supports the conclusion that the dominant part of the PPTCUP noise is emitted by the spark plug.

Table 4-6 - Noise emitted by the PPTCUP spark plug and the main discharge

Spark plug noise		Main discharge noise	
I_{el} [A]	100	I_{mag} [A]	10,000
L_{dip} [mm]	0.5	D [mm]	10
f [MHz]	100	f [MHz]	0.7
r [m]	1	r [m]	1
N_{el} [V/m]	3.15	N_{mag} [V/m]	6.4E-3

4.4.2. PPTCUP-QM EMC test results

Even if important elements have been found from the qualitative noise characterization performed on the PPTCUP-EM (§4.4.1), it has been decided to run a proper electromagnetic compatibility (EMC) test to fully characterize the electromagnetic noise produced by the PPTCUP-QM module.

The EMC characterization was performed according to the NASA MIL-STD-461C and 462 standards as already done in the past for other PPTs (§2.2.4). Tests covered:

- the conducted emissions on the power leads in the range between 100 Hz to 50 MHz (both in differential and in common mode);
- the radiated electric field in the range between 150 kHz and 1.8 GHz;
- the radiated magnetic field in the range between 20 Hz and 50 kHz;
- the radiated susceptibility due to radiated electric field in the range between 14 kHz and 1 GHz.

The EMC experimental test campaign was performed with the thruster placed in the bell jar described in §3.1.1 that guaranteed the correct level of vacuum required to fire the PPT. Since it is necessary to keep the pump system (including the power supplies and the pump cooling system) on during the entire test, it has been decided to repeat each test case twice. In the first run, no shots were commanded and only the background noise (i.e. the noise generated by the pumping system and the power supplies) was detected. In the second run, the thruster was fired at nominal frequency of 1 Hz and the data acquired.

As discussed in §2.2.4, in previous publications regarding studies on the electromagnetic noise generated by PPTs [44], [85], [87], [88], it has been pointed out that the EMC standards used by NASA are unsuitable to characterize an inherently pulsed device having been developed for devices that work continuously. For this reason, to better judge the EMC results that have been gathered and to assess the suitability of PPTCUP to be used on-board of a spacecraft, the results are compared to those acquired during the flight qualification of the PPT developed for the NASA Earth Observing 1 mission (EO-1 PPT) [87], [88]

4.4.2.1. Conducted emissions

The conducted emissions test have been performed using suitable Rogowski coils to measure the AC current flowing in the cables that feed the PPTCUP-QM in the range between 100 Hz to 50 MHz (Figure 4-20). As described in §3.4, the module requires two power lines (i.e. a +3.3 V and a +7.6 V) that have the two potential reference in common and connected to the ground. Since the testing requires the measurements of the noise both in differential and in common mode, a total of five acquisitions have been performed: three for the differential mode (i.e. +3.3 V, + 7.6 V and

ground) and two for the common mode (i.e. + 3.3 V and ground cables and +7.6 V and ground cables).

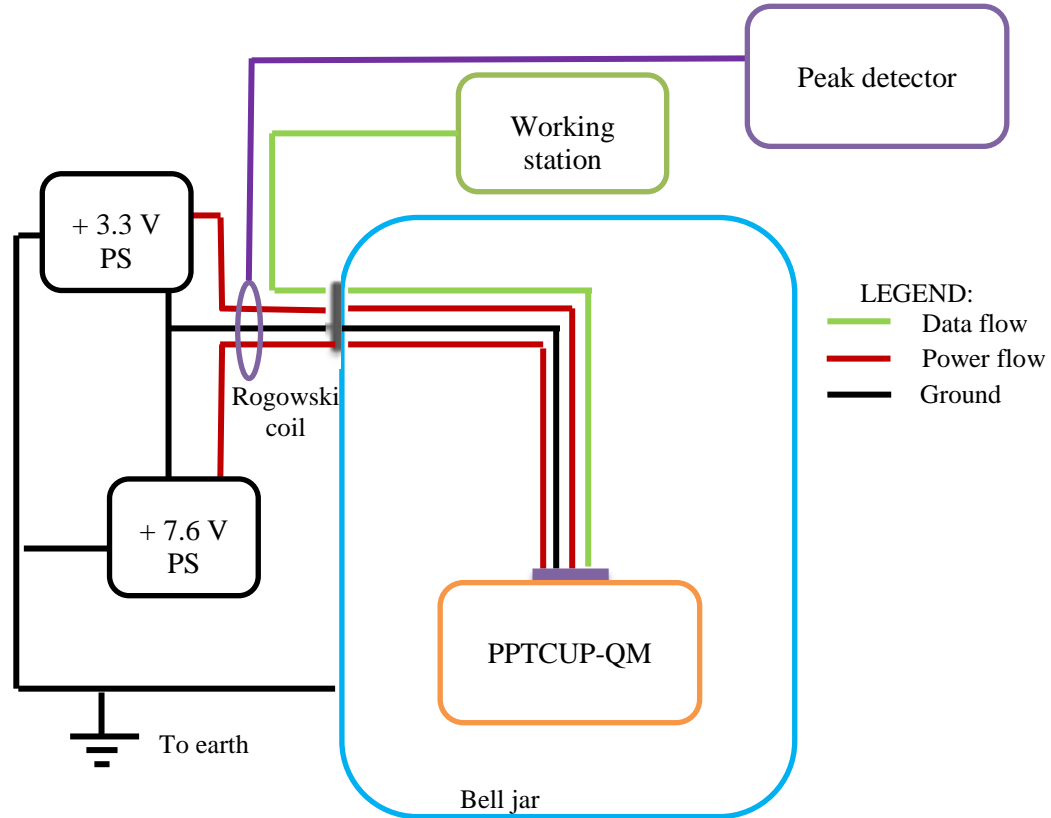


Figure 4-20 – Conducted emission test set-up.

Figure 4-21 shows the results of the test performed in the differential mode on the ground line, where the blue curves represent the background noise acquired without firing the thruster and the red curves represent the noise detected firing the PPT. The complete results are reported in ANNEX B. The level of noise measured during the testing was often smaller than the requirements and not always possible to distinguish from the background noise. However, peaks exceeding the requirements have been found during the acquisitions. These peaks are mainly centred around 30 kHz and in the range between 2.5 and 15 MHz and exceed the requirements by a maximum of about 45 dB. Nevertheless, by comparing these data with the results of the conducted emissions of the EO-1 PPT [117] shown in Figure 4-22, it is possible to notice that the magnitudes of the detected noise are similar.

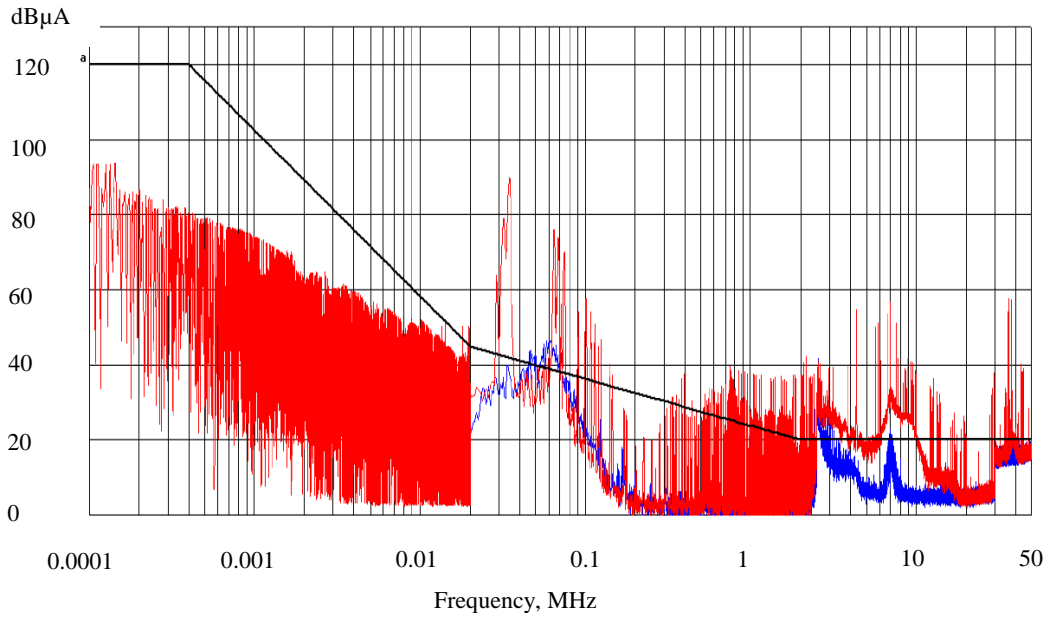


Figure 4-21 – Conducted emissions (ground line, differential mode) test results. The blue and red curves represent respectively the background noise and the noise with the thruster on. The black line indicates the requirements.

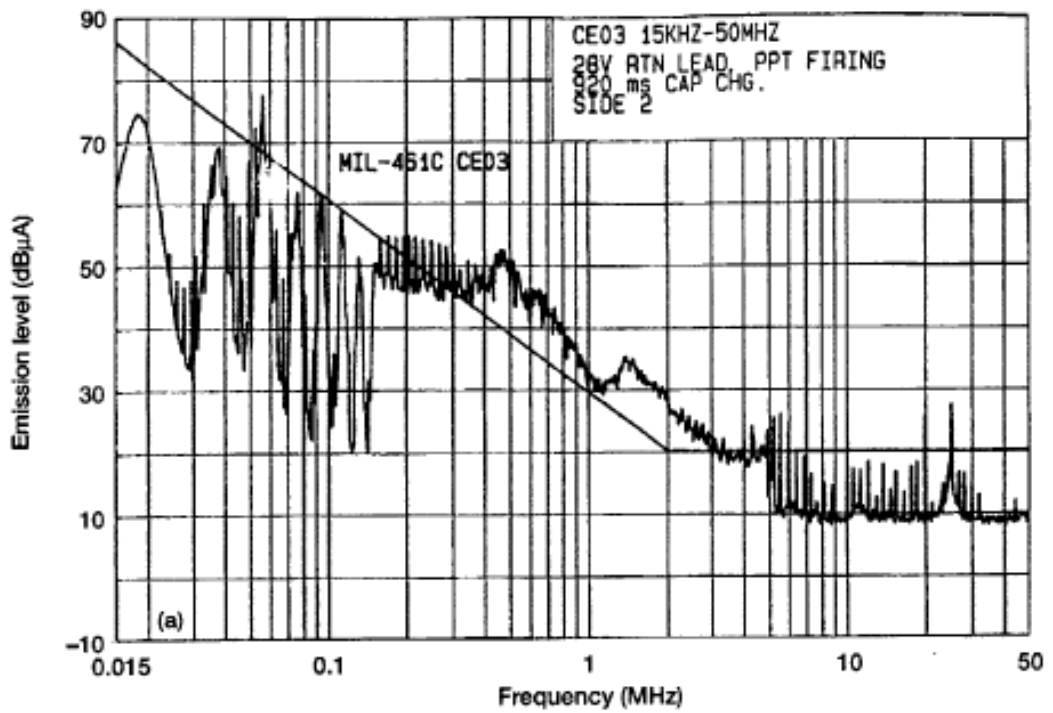


Figure 4-22 – EO-1 PPT conducted emissions [117].

4.4.2.2. Radiated emissions

The radiated emissions test have been performed using four different antennas to measure the radiated noise generated the PPTCUP-QM module, covering the range between 150 kHz to 1.8 GHz for the radiated electric fields and the range between 10 Hz to 50 kHz for the radiated magnetic field. The antennas were placed at approximately 1 m from the thruster, as shown in Figure 4-23.

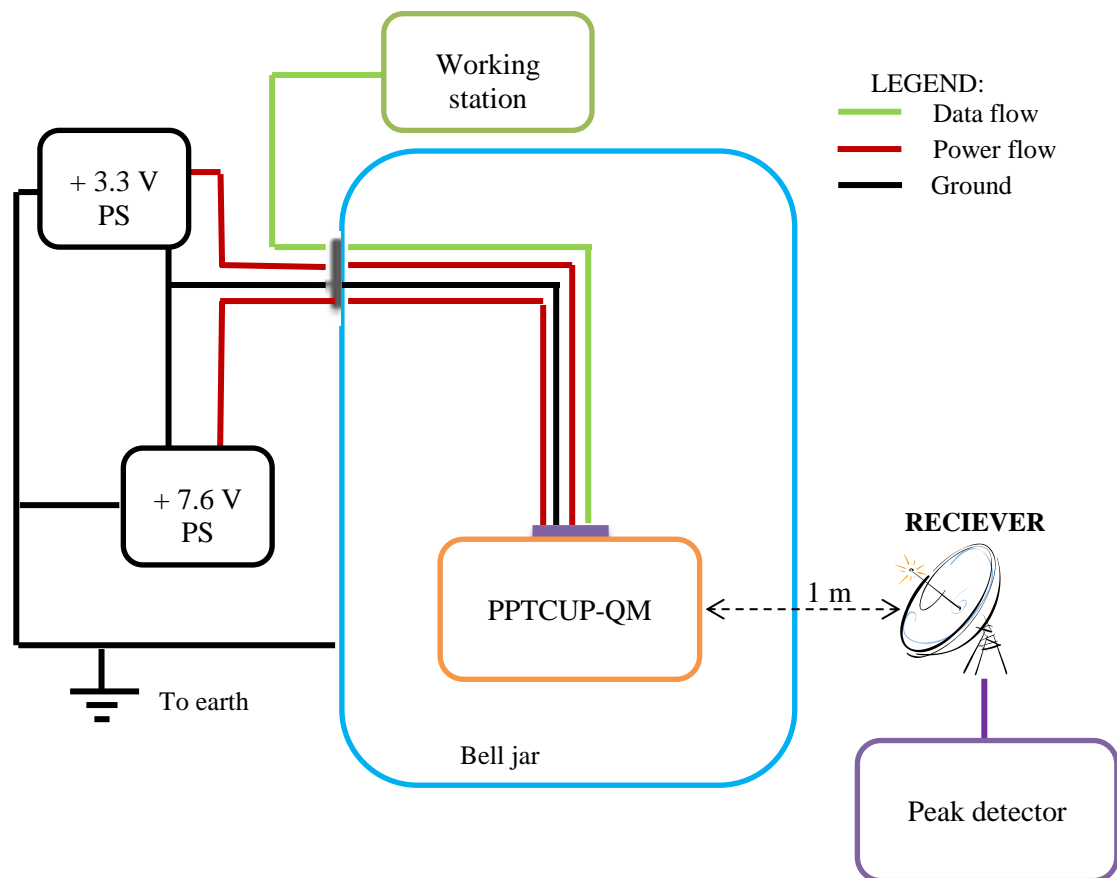


Figure 4-23 - Radiated emission test set-up.

The results of the radiated electric and magnetic fields are shown in Figure 4-24 and Figure 4-25. The complete results are reported in ANNEX B. The level of noise measured during the testing (i.e. the red curves in the figures) was often impossible to distinguish from the background noise (i.e. the blue curves).

The radiated magnetic field is compliant with the requirements in the whole range of frequencies. For what concerns the electric field, it has been found that the noise generated by the unit is very similar to the background noise.

When the thruster was fire, several spikes were detected in the range between 100 and 500 MHz. They are likely generated by the spark plug discharge that is characterised by a fundamental frequency of the order of hundreds of MHz (see

§4.4.1). This confirmed what was theorized for the first time during the development of the LES-6 and LES-7/8 PPTs between 1960s and early 1970s [85], [86]

Finally, it has to be noticed that the magnitude of the noise due to radiated electric field is smaller than the one detected during the EO-1 PPT qualification after the introduction of the external envelope to partially shield the electromagnetic radiations (discussed in §2.2.4 and shown in Figure 2-23). Therefore, from the comparison of the results of the EO-1 PPT and the PPTCUP-QM, it can be concluded that the use of an external box to enclose the PPT and its conditioning electronics is highly recommended to limit the radiated noise. However, it has to be noticed that the introduction of the EMI shield increases the total mass of the propulsion system that should be kept as small as possible, particularly for Cubesat applications where the mass and volume budgets are relatively tight.

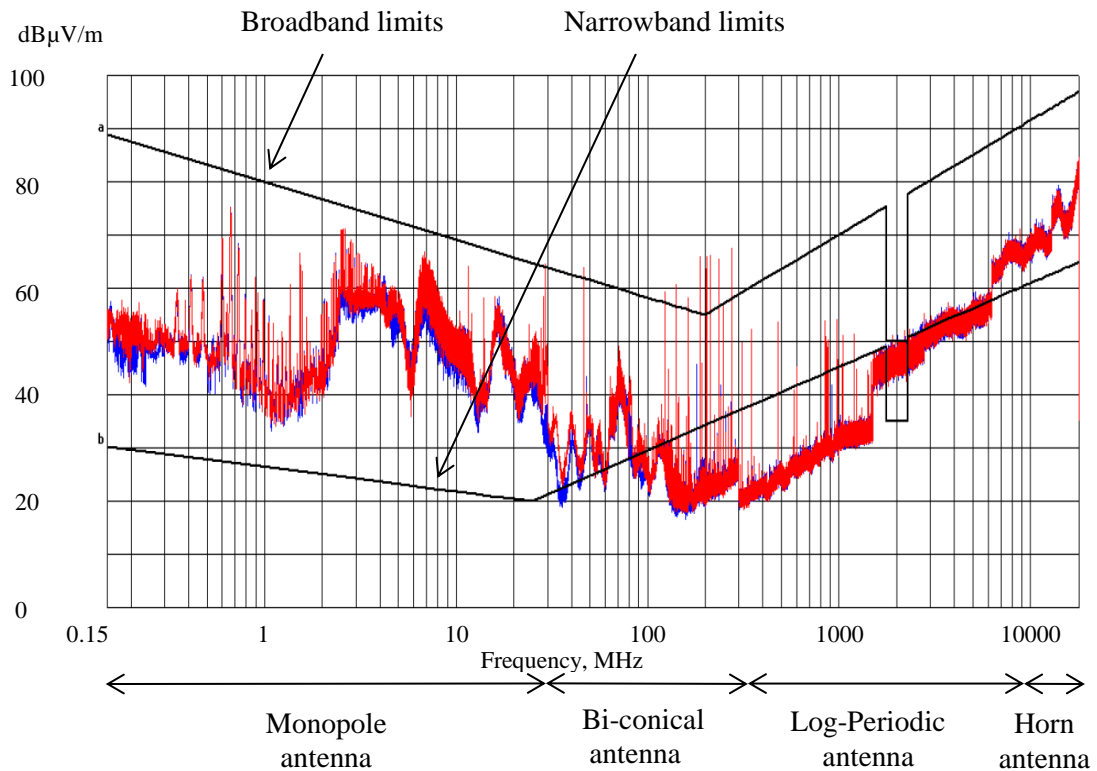


Figure 4-24 – Radiated electric field test results. The blue and red curves represent respectively the background noise and the noise with the thruster on. The black line indicates the requirements.

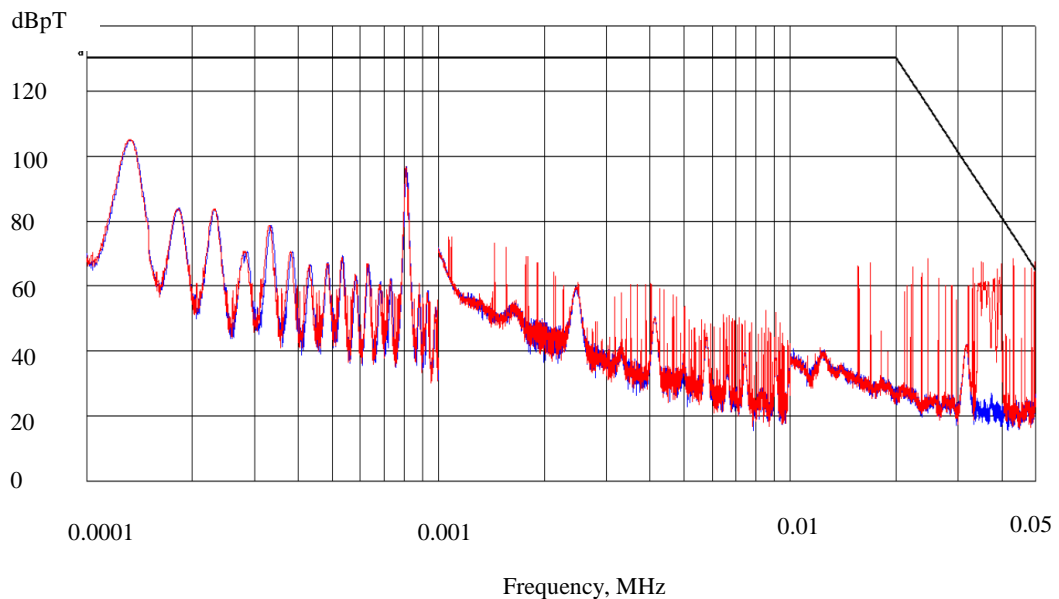


Figure 4-25 – Radiated magnetic field test results. The blue and red curves represent respectively the background noise and the noise with the thruster on. The black line indicates the requirements.

4.4.2.3. Radiated susceptibility

The radiated susceptibility test was carried out over a frequency range of 14 kHz to 1 GHz. The applied susceptibility electric field level was 2 V/m as described in the NASA EMC standards. The emitters were placed at approximately 1 m from the thruster, as shown in Figure 4-26. The test was successfully passed because the PPTCUP operated without failures during the test and there were not found any changes to the module functionality in post-test operations (see §4.2.4).

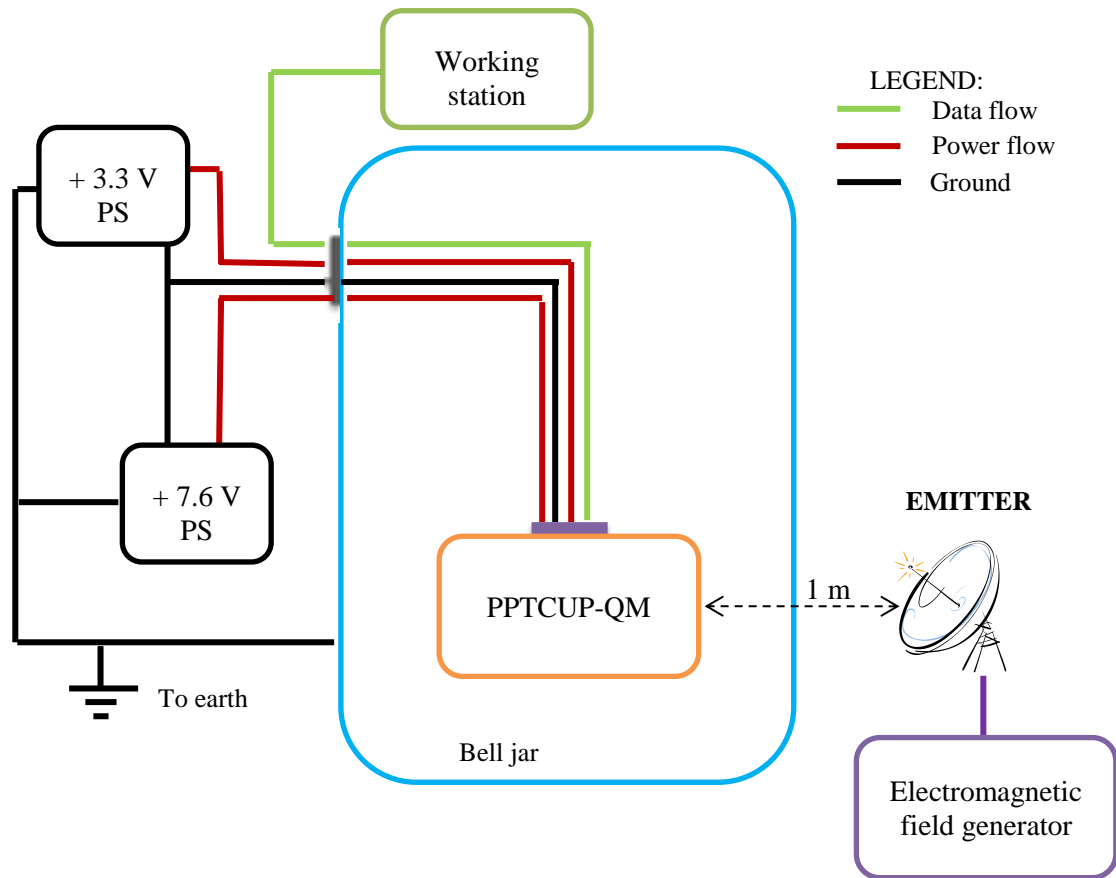


Figure 4-26 - Radiated susceptibility test set-up.

4.5. Spark plug breakdown voltage study results

As explained in §3.5, the reduction of the spark plug breakdown voltage can be achieved by depositing a layer of semiconductor on the spark plug insulator surface exposed to the main discharge. Coated spark plug insulators have been produced (see Figure 3-35) and tested.

A preliminary test has been performed using the GSE-2 to verify if the samples could generate an arc between the electrodes under vacuum condition and hence trigger a PPT main discharge. Then the selected samples were tested on the NanoPPT (see ANNEX A) driven by a low voltage electronics board designed and manufactured by Clyde Space Ltd. This second phase of testing had two main purposes: 1) to verify if the use of semiconductor-coated spark plugs produces any significant change in the thruster performance in terms of impulse bit current parameter and mass bit consumption and 2) to verify semiconductor-coated spark plugs lifetime and eventual degradation in performance.

4.5.1. Coated spark plug insulator selection

The coated spark plugs (Table 3-4) have been inserted into the upper electrode of the NanoPPT. During the test, the chamber pressure has always been maintained below $5 \cdot 10^{-5}$ mbar.

The voltage was applied between the spark plug and the main electrode, connected to the ground, starting from 0 V and increasing the value with step of 100 V until spark appeared on the coated surface between the two electrodes and the voltage drop detected by the oscilloscope. That value has been assumed as the breakdown voltage of that configuration.

The results are summarized in the following table.

Table 4-7 – Spark plug insulators selection summary

Bulk material	Coating	Test results: Breakdown voltage
PTFE	No coating	≈ 8,000
	a-Ge:H	< 1,000
	a-Si:H	≈ 7,200
Macor	No coating	≈ 8,000
	a-Ge:H	< 1,000
	a-Si:H	≈ 7,000

Breakdown voltages found for the uncoated configurations are in the range of the expected values, given the dimensions of the spark plug insulator. The coated rods are characterized by a lower breakdown voltage. However, it is clear that germanium is the best material to use to coat the spark plug insulator, as both the tested configurations are able to generate a vacuum arc once a voltage of about 1 kV is applied. At last it has to be noticed that the insulator bulk material does not sensibly affect the breakdown voltage.

4.5.2. Coated spark plug insulator characterization test

Given the results of the spark plug insulator selection in §4.5.1, only the PTFE and Macor samples coated with a-Ge:H have been mounted in the NanoPPT and tested. The test campaign was carried out twice, changing the spark plug coated propellant. First of all the electrical characteristics of the thruster in terms of voltage and current curves were acquired. For both the spark plug configurations, ten shots were performed and the data averaged. The discharge current and voltage curves are

reported in Figure 4-27. In both cases, the NanoPPT showed a very repeatable functioning with a standard deviation values for ψ of less than 2%. Moreover no appreciable differences have been found during the discharge of the NanoPPT triggered by coated PTFE and Macor spark plugs (i.e. applying a “low” spark plug voltage of about 2 kV) with respect to the discharge obtained with uncoated spark plug performed applying a spark plug voltage of about 7.5 kV [34].

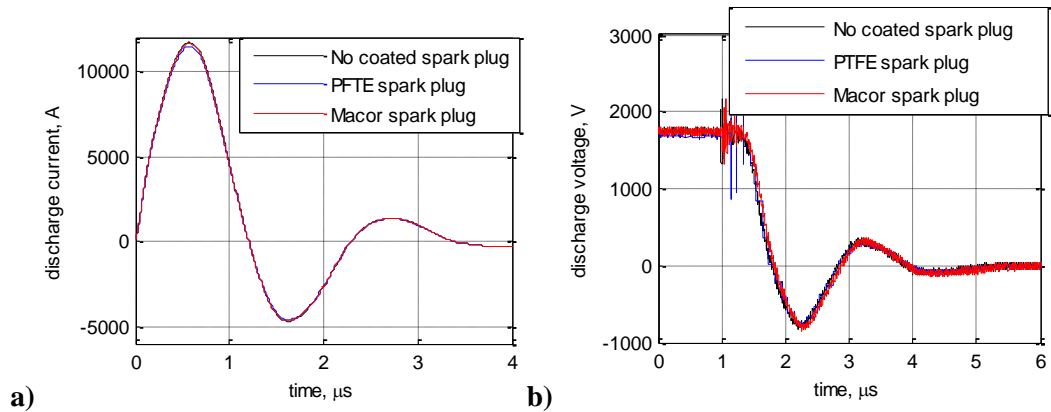


Figure 4-27 – Comparison of the a) discharge current and b) discharge voltage curves

The *Ibit* was measured using the direct impulse balance described in §3.2.3. For each energy value 10 measurements were taken and averaged. The thruster mass bit consumption has also been measured performing a sequence of 300 shots and achieving a measurement error of less than 3%.

The measured performances are summarized in Table 4-8, together with the results obtained during the test campaign of the same thruster with the no-coated spark plug [34]. It has to be noticed that all the results are in very good agreement and always within the error bars.

Table 4-8 – Summary of the NanoPPT performance validation test results

Measurements	No coating (data from [34])	PTFE coated spark propellant	Macor coated spark propellant
Initial energy [J]	5	5	5
Spark plug voltage [V]	≈ 7500	≈ 1720	≈ 1720
Current parameter ψ [As ²]	90.9 ± 1.5	88.1 ± 1.7	89.6 ± 1.6
Impulse bit [μNs]	90.0 ± 8.1	87.7 ± 7.9	88.4 ± 8.0
Mass bit [μg]	14.75 ± 0.24	14.1 ± 0.23	15.2 ± 0.25
Specific impulse [s]	622 ± 57	634 ± 58	593 ± 54
Efficiency [%]	5.49 ± 0.70	5.45 ± 0.70	5.14 ± 0.66

The spark plug lifetime test has been performed running several sequences of 1000 commanded sparks and counting the number of the occurred sparks. During the whole test, the capacitor bank was not charged. The firing rate β , defined as the ratio between the “real” and the commanded sparks, was calculated at the end of each sequence. The test was ended when β was $< 5\%$.

Both the PTFE and the Macor spark plug coated by a layer of a-Ge:H were able to produce a spark at the same voltage applied to the capacitor bank ($V_0 = 1720\text{ V}$) with $\beta > 95\%$ only for the first 10,000 shots. After 10,000 shots the firing rate started to decrease very quickly. As shown in Figure 4-28, the PTFE spark propellant stopped working after about 14,000 shots, whereas the Macor spark propellant had the failure after about 15,000 shots.

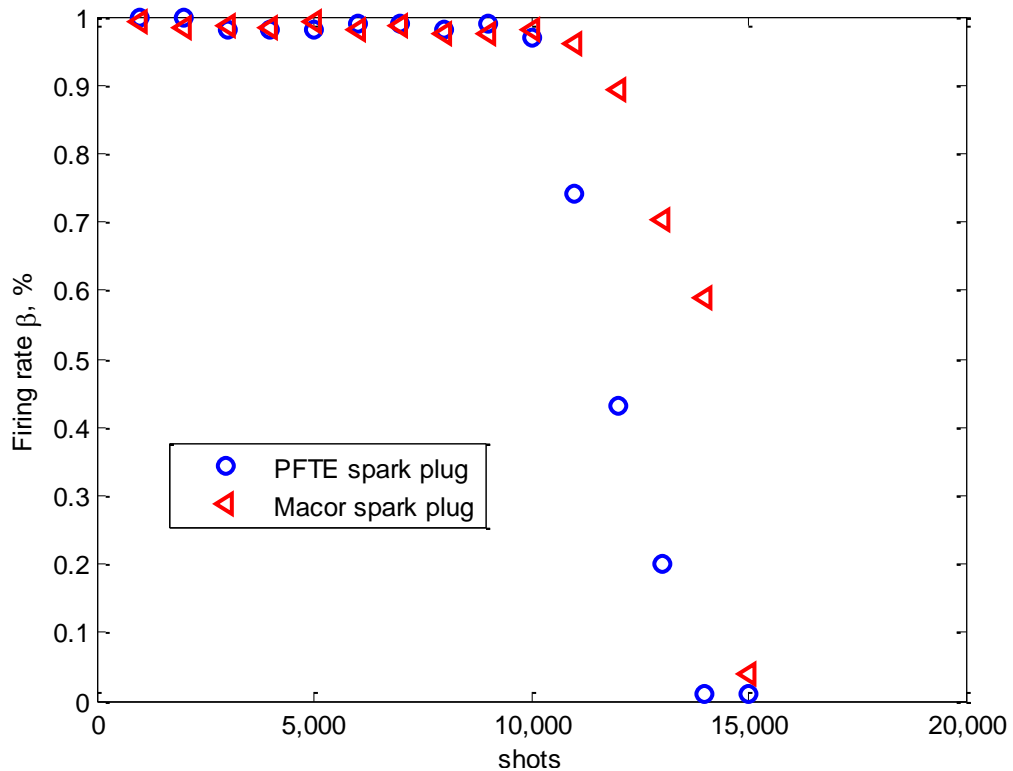


Figure 4-28 – Firing rate β trend with the number of shots.

Pictures of the coated spark plugs at the beginning of the test campaign and after the end of the lifetime test have been taken and reported in Figure 4-29. It can be noticed that from a visual inspection the a-Ge:H coating changed colour during the test campaign, from a bright grey at the beginning of the test to brownish colour at the end of the test.

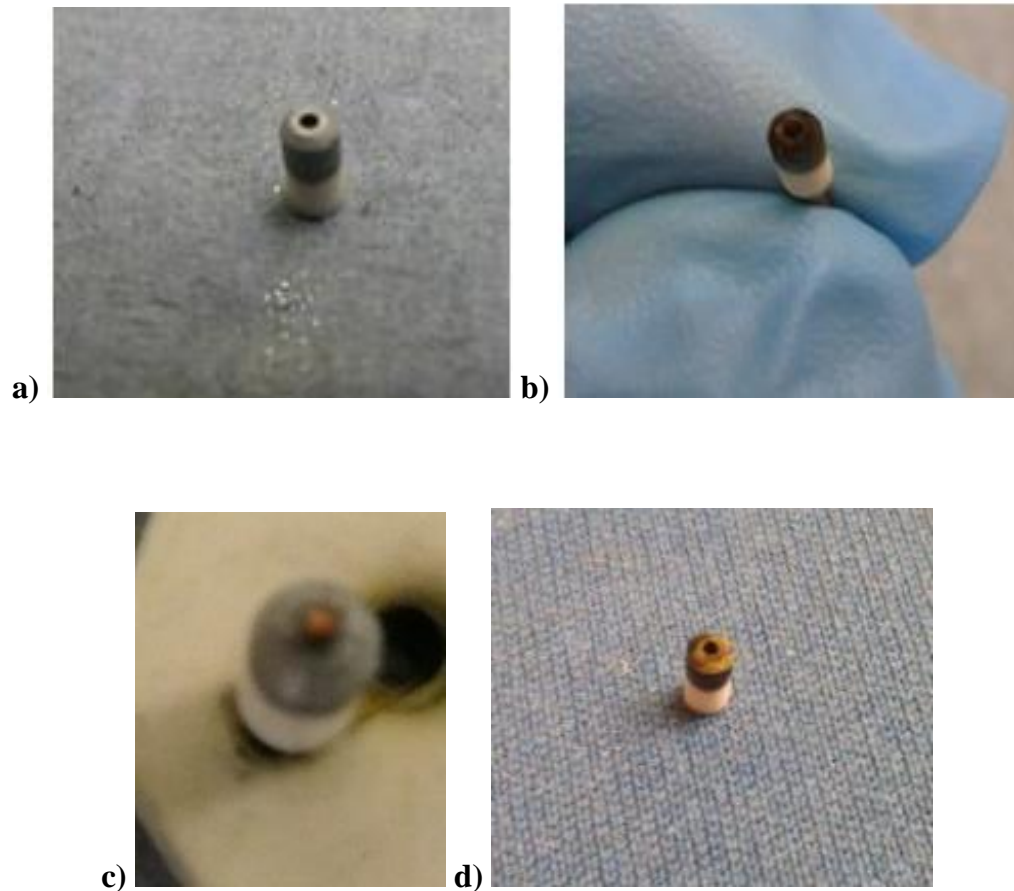


Figure 4-29 - Spark plug insulators coated with a-Ge:H a) Macor new b) Macor after 15,000 shots c) PTFE new d) PTFE after 13,000 shots

A SEM scanning has been performed to try to qualitatively understand the cause of such short coated-spark plugs lifetime. By comparing Figure 4-30 and Figure 4-31, which respectively show the semiconductor layer at the beginning (i.e. not used yet) and at the end of the test campaign (i.e. end of lifetime), it can be noticed that the a-Ge:H layer appears cracked.

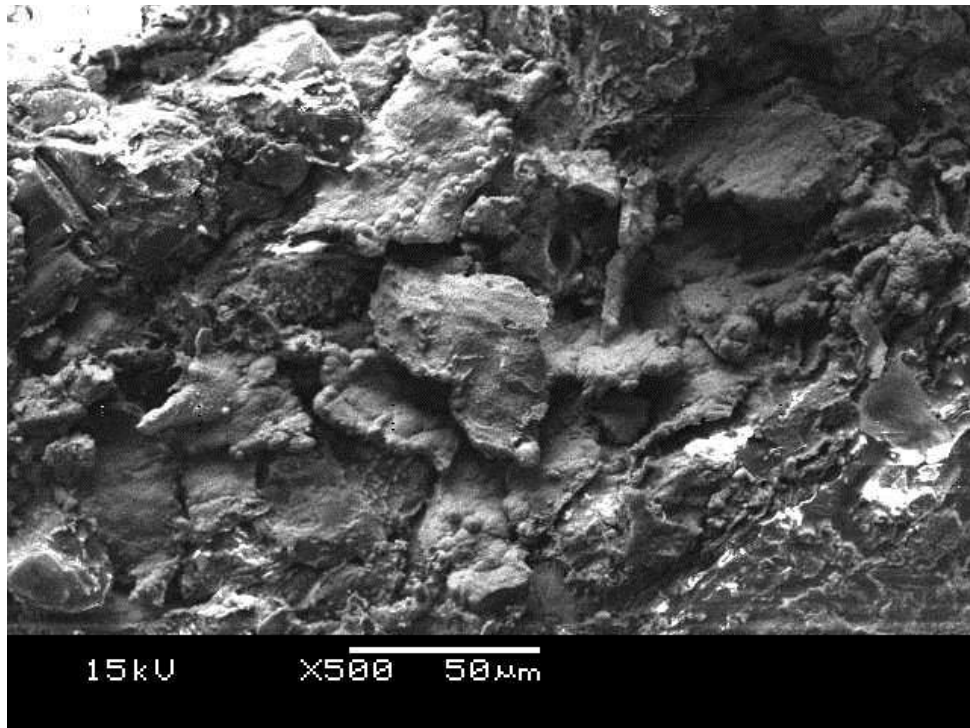
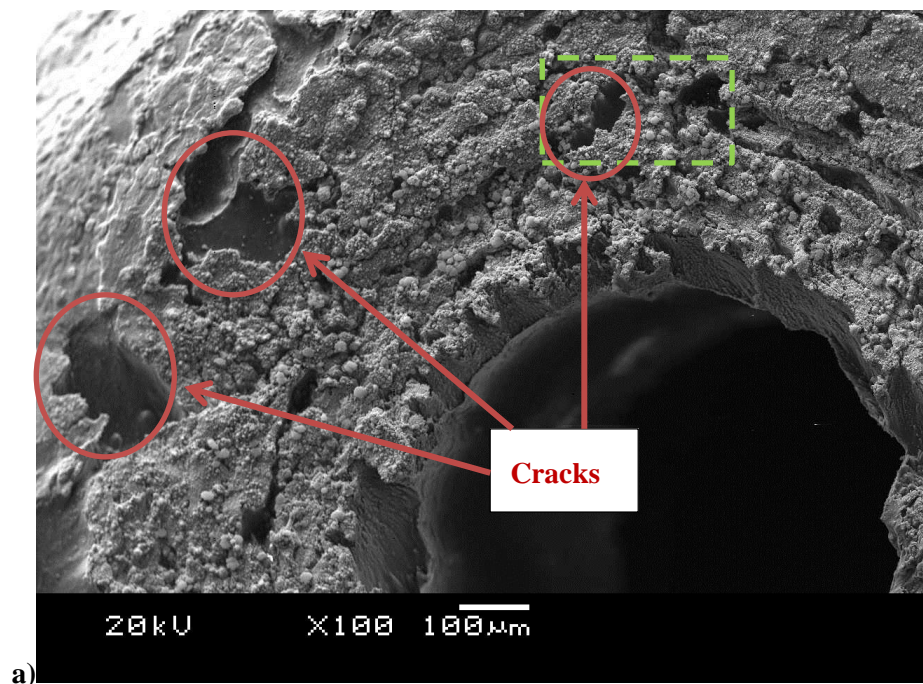


Figure 4-30 – SEM picture of the a-Ge:H layer before the beginning of the test



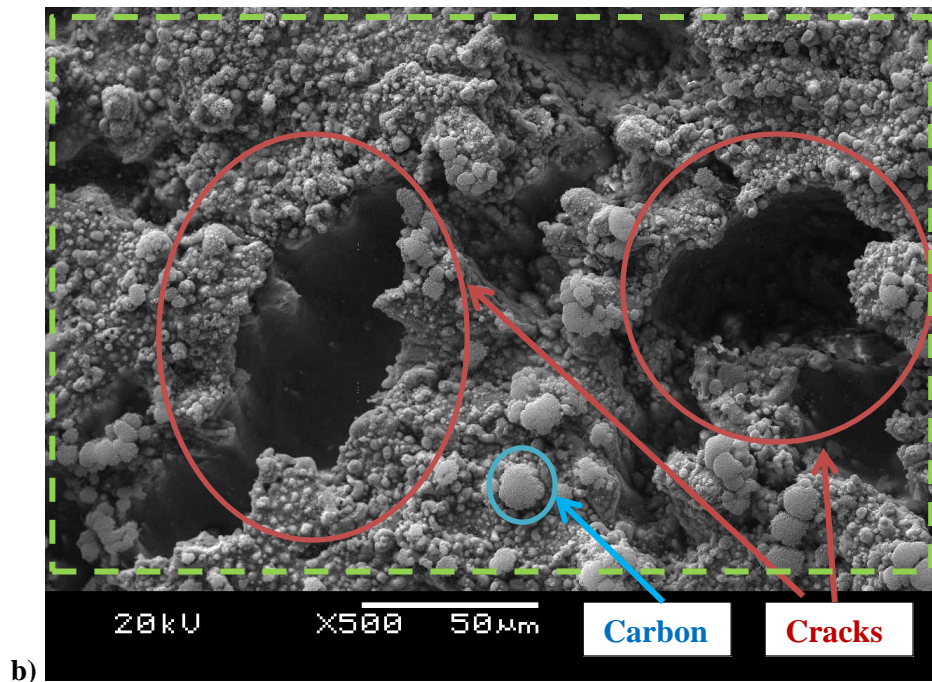


Figure 4-31 – SEM picture of the a-Ge:H layer at the end of the lifetime: a) magnification x100 b) magnification x500. Highlighted: the cracks on the a-Ge:H layer (red circles) and traces of carbon in the shape of globules (blue circle)

The most likely explanation for this effect is that the breakdown that generates the spark occurs at the very small gaps and flaws in the thin semiconductor layer as experienced in the vacuum arc thrusters [65].

As shown in Figure 4-30, at the beginning of the test the metal film deposited with PECVD technique consists of layers of grains and flakes rather than being a single smooth surface. It has to be noted that even if the average thickness of the coating can be predicted and controlled during the deposition, the final coated surface of two different samples cannot be identical. This is likely the main cause of the performance decay difference occurred in the PFTE and Macor samples (Figure 4-28).

The roughness of the surface creates the gaps where the spark is initiated. Then, these discharges create “hot spots” within the metal layer, producing metal vapour (that initiates the main spark) and cracking the surface itself and hence making the coating ineffective because of the higher equivalent resistance. It has to be noted that this phenomenon may be amplified by the fact that the molecular bonds in an amorphous semiconductor are weaker than the bonds in crystalline material [69], [73]. Thus the applied electric field can be strong enough to break the material.

Finally, from the analysis of the spark plugs after the lifetime test, carbon has been found on the a-Ge:H layers in the shape of single or cluster of globules. This has been detected and identified with the EDX spectroscopy technique (Figure 4-31 and Figure 4-32). Carbon likely comes from the propellant mass ablated during the

performance characterization test. The shape of the deposited carbon is similar to the one that was detected on the electrodes of the PPTCUP-EM (Figure 4-15) at the end of its lifetime test and due to the propellant ablation.



Figure 4-32 - Details of the carbon globules deposited on the semiconductor layer of a coated spark plug insulators.

Chapter 5. Conclusions

5.1. Overview

The study of lifetime of ablative PPTs for miniaturized satellites have been presented.

To achieve the purpose of the project, a miniaturized ablative PPT (i.e. PPTCUP) has been developed and tested, including in its design all the possible fixtures that could improve the lifetime and the performance. Carbonization and spark plug system failures have been identified as the most important factors that limit the PPTs lifetime.

An engineering model of the PPTCUP (PPTCUP-EM) has been designed and manufactured taking into account the results obtained during the PPTCUP breadboard model (PPTCUP-BB) characterization and previous experience reported in the relevant literature [29], [30], [31], [39], [47], [58], [59].

Despite the growth of a layer of carbon on the walls of the discharge chamber, the PPTCUP-EM discharge chamber has successfully completed about 1,800,000 shots. Results from the study of the influence of the spark plug position and the feeding configuration on the performance show that the side-fed configuration with the spark plug located at the breech of the cathode is characterized by the highest $I_{sp} = 608 \pm 55$ s and deliverable $I_T = 42.9 \pm 3.9$ Ns. Propellant ablation was uniform in both the tested feeding configurations and no performances decay caused by the thruster aging was found.

The PPTCUP qualification model (PPTCUP-QM) has been developed from the engineering model design as a potential flight qualified product. Therefore, the PPTCUP-QM is a “stand-alone” module that can be bolted on the Cubesat structure and it has to undergo an extended qualification test campaign. The unit has successfully completed the thermal cycling, vibrations and EMC characterization tests. Unfortunately, the three years available for this research programme have not been enough to run the PPTCUP-QM lifetime test that, at the time of the writing, is still ongoing.

The performances of the thruster have been checked after the thermal and the mechanical and the EMC tests to verify that no damage occurred in the unit during these tests. Results from the test campaign show that PPTCUP-QM:

- works correctly in the range of the operating temperatures (from -20 to +65°C);
- withstands the mechanical vibrations during launch and has main natural frequencies compliant with the Cubesat requirements;
- generates electromagnetic noise mostly compliant with the requirements or small enough to be impossible to distinguish from the facility background noise.

A dedicated study has been performed to identify the best spark plug system able to trigger the PPT main discharge with a relative low breakdown voltage. The most promising configuration is a spark plug rod coated with germanium. This “coated” spark plug was tested and the results show that it is able to trigger the main discharge when a lower voltage (i.e. 1720 V opposing to the 7500 V needed for the uncoated propellant rods) is applied without affecting the overall thruster performances. However, issues regarding their lifetime arose and still remain because the breakdown voltage increases after about 11,000 shots. Scanned Electron Microscope (SEM) inspection has shown that this is likely due to cracks that occur on the semiconductor layer.

5.2. Contributions

The main contributions and the novelty of this research to the electric propulsion are presented here.

5.2.1. PPT discharge chamber carbonization

Thanks to the analysis of the previous knowledge available in the relevant literature, the following suitable key design modifications were introduced to solve the carbonization problem:

- The lateral grooves in the inner wall of the discharge chamber,

- The double back-plate arrangement,
- The gap between the electrodes and the nozzle walls.

The actual design was extensively tested and the discharge chamber successfully completed about 1,800,000 shots, i.e. 60% bigger than the nominal number of shots required to deliver the entire total impulse. Moreover, the performed number of shots results also in being almost three times bigger than the latest endurance test performed on a miniaturized PPT.

5.2.2. PPT performance optimization

The influence of the spark plug electrode position and the propellant feeding configuration on the overall thruster performance (i.e. in terms of specific impulse and deliverable total impulse) was assessed during the project.

Results from the testing show that it is possible to maximize the performance of an ablative PPT of a given geometry and input power:

- By positioning the spark plug electrode at the breech of the cathode and as close as possible to the capacitor bank,
- By preferring the side-fed configuration to the V-fed feeding configuration.

5.2.3. Spark plug breakdown voltage

A study has been performed to identify a spark plug system able to trigger the PPT main discharge with a lower breakdown voltage that is about 7.5 kV for the PPTCUP and the NanoPPT.

Thanks to the analysis of the previous knowledge available in the relevant literature, it has been found that PTFE and Macor spark plug insulator rods could be used for this purpose when coated with a layer of semiconductor. The results of a dedicated material selection showed that the most promising material to use is the germanium deposited with the Plasma-Enhanced Chemical Vapour Deposition (PECVD) technique. The contribution and novelty of this part of the research to the field can be summarized with the following key points:

- Identification of a working “low voltage” spark plug configuration, including the coating material and the deposition technique to use;
- Significant reduction of the breakdown voltage, e.g. in the NanoPPT testing only 1,720 V were enough to trigger the discharge opposing to the almost 8,000 V for the uncoated propellant rods, without affecting the overall thruster performance
- Possible reduction in complexity of the PPT electronic board design because of the lower voltage that has to be applied to the spark plug electrodes.

5.2.4. Electromagnetic interference and compatibility

Looking at a PPT as a sub-system that is interfaced with the spacecraft sub-systems, the electromagnetic noise generated by a pulsed device like a PPT has to be carefully taken into account to avoid failures in the spacecraft during the mission. Therefore, during the project, the noise generated by the PPTCUP has been firstly preliminary analysed and then fully characterized with a dedicated electromagnetic compatibility (EMC) testing. The contribution and novelty of this part of the research to the field can be summarized with the following key points:

- For the first time, a PPT designed for Cubesat application, i.e. the PPTCUP-QM, underwent a complete EMC test performed following the NASA procedures
- It has been proved that the spark plug is the main source of electromagnetic noise rather than the main discharge;
- Evidences from the EMC test results confirm that the use of an external box to enclose the PPT and its conditioning electronics is highly recommended to limit the radiated noise emissions.

5.3. Achievements

During this project a series of research and personal achievements were accomplished and are described in this section.

5.3.1. Project achievements

- The PPT discharge chamber design innovations solved the carbonization problem that is due to the carbon conductive path deposited in the discharge chamber and that might eventually short the PPT electrodes.
- The PPTCUP lifetime was proved to be about 60% bigger than the nominal lifetime required to deliver the entire total impulse.
- The PPTCUP lifetime was proved to be almost three times bigger than the latest endurance test performed on a miniaturized PPT.
- The PPTCUP was the first PPT for Cubesat applications to undergo a complete EMC test campaign.

- It has been proved that the spark plug is the main source of electromagnetic noise both during the preliminary noise characterization, using the two-source model, and during the EMC testing.
- It has been found that an external box to enclose a PPT significantly limit the radiated noise emissions.
- A working “low voltage” spark plug configuration has been identified, manufactured and tested, showing a significant reduction of the breakdown voltage without affecting the PPT performance.
- Three flight models have been already ordered, pending the conclusion of the PPTCUP-QM test campaign, and will possibly be launched in the next 2 years.

5.3.2. Personal achievements

All the work done over the past three years has been an incredible and unique opportunity for the growth of my technical skills and knowledge. With the hope that I learnt as much as possible from all the faced challenges, the most important personal achievements are:

- To have had the opportunity to present my research in international conferences, where I met all the most important experts that gave and are still giving the most significant contribution to the field;
- To have two conference proceedings awarded as best papers of the session;
- To have contributed to the scientific research of the field with the production of four peer-reviewed journal papers that are already published or accepted.
- To have increased my knowledge in engineering fields (e.g. electronics, material sciences and signal processing) different from the electric propulsion field, because the solution of some challenges required a more complete understanding of all the physics processes that were happening.

5.4. Future work

5.4.1. PPTCUP-QM further development

The PPTCUP-QM should complete the lifetime test to further confirm the reliability of the thruster and to quantify the actual total impulse that the unit can deliver. This will complete the qualification of the thruster that would be then ready for the space flight. Considering the advantages of using a PPT system and the growth of the Cubesat market, this could globally strengthen the University of Southampton and the UK reputation of the electric propulsion and possibly of the space propulsion sector.

5.4.2. PPT numerical model development

Future works should also focus on developing a predictive PPT model to be used to define the PPT design that can deliver the best performance (i.e. the highest I_{sp} and I_T) given fixed constrains (e.g. maximum overall dimensions, mass and/or input power). A valid starting point for the development of this predictive model may be the “snowplow model” [20]. The classic approach in order to solve it is to assume that all the inputs parameters are constant hence relying on the availability of the experimental data needed to determine the plasma characteristics and the ablated mass. Indeed, most of the optimization efforts carried out so far were strongly based on experimental measurements and lasted for several years (e.g. the studies on the LES-6/7 and SMS in the 70s [6], [39], [42] and the on-going studies at IRS [14], [95] and Tokyo Universities [110]). To improve the state of the art in PPT modelling and move away from the need of a vast amount of experimental data, it may be necessary to model the physical processes that occur during the PPT discharge to predict the influence of the thruster geometry and operational parameters on performance. Given the complexity of these processes (coupling of thermal, chemical, electromagnetic and gas and plasma dynamics processes), in the predictive PPT performance model, the thruster should be represented as an RLC circuit but with electrical parameters that are variable in time and space and obtained from the numerical simulation of the different physical processes. This model would ideally remove the need of extensive test campaigns. Therefore, the model would have a strong multidisciplinary character, since it would need to include: the estimation of the magnetic field generated by the discharge current, the characterization of the plasma column in the discharge (in terms of its size, ionization level, electrons and heavy particle temperature and resistivity) and the quantification of the propellant ablation as a function of the discharge parameters. Assuming a given thruster geometry, the model would be able to calculate the space and time variable parameters to use as inputs for the standard PPT snowplow model. The snowplow

model will then allow for the calculation of the PPT performances in terms of impulse bit, specific impulse and total impulse. Then, it should be possible to find the best configuration by iteratively changing the thruster geometry and input parameters. From a research point of view this model would not only be useful in order to shorten the time scale of experiments, but might also be used to exploit new PPT designs, and their validity, prior to develop new test campaigns.

5.4.3. Spark plug breakdown voltage

Considering the results of the coated spark plug insulator rods, there are three possible ideas for future work:

1. Trying to solve the coated spark plugs lifetime issue. A valid starting point may be the results of the SEM investigation. Since several cracks were found on the deposited material, future works will possibly include a suitable study of the amorphous semiconductor layer to identify perhaps a more efficient way to deposit the material on the propellant rod or a better semiconductor element or compound to use.
2. Developing a numerical model to understand how the semiconductor coated spark plug insulators works. In the PPTCUP and NanoPPT applications, the voltage that the conditioning board applies to the spark plug electrodes is originated by the discharge of a capacitor across a high voltage transformer designed to provide the required breakdown voltage. During the discharge, the current that flows on the deposited layer causes the heating of the material. Therefore, the resistivity of the semiconductor changes because of the temperature variation and consequently the discharge process is modified because of the equivalent resistance that depends on the deposited material resistivity. During the entire process, the semiconductor ablates depending on the temperature reached during the capacitor discharge, which typically lasts few tens of nanosecond. Then after a period of time, which depends on the PPT firing frequency, a new spark is generated and the entire process restarts.
3. Using the metal-coated spark plugs propellant. The most promising configuration of this kind of spark plugs has been investigated during this project and two possible coating metals, i.e. titanium and gold, have been identified considering the deposition equipment capabilities at the University of Southampton. However, as described in the relevant literature [59], [63], [65], [66], [67], [82], the thin metal layer has to have an equivalent resistance in the range between 1 and 1000 Ω . Therefore, for equation (80) and for the typical resistivity values of these two metals ($\rho_{Ti} = 5.6 \cdot 10^{-7} \Omega\text{m}$, $\rho_{Au} = 2.2 \cdot 10^{-8}$

Ωm), a layer of a thickness of the order of some tens of nm would have an equivalent resistance of few Ω using Ti or fraction of Ω using Au. Since the Au layer resistance would be out of the range reported in the literature, titanium should be chosen as material to deposit on the spark plug insulator. However, it has to be noticed that even if spark plug insulators coated by metal have been successfully used in VATs [63], [68], the replenishment of the thin metal layer on a PPT spark plug insulator might not work properly, limiting the lifetime of the spark plug and of the PPT itself.

ANNEX A. NanoPPT performance results

The breadboard model of the NanoPPT has been designed and developed by the University of Southampton, Mars Space Ltd and Clyde Space Ltd with the mission requirement of providing attitude and translational control for a 20 kg nano-satellite for a total ΔV of 40 m/s. The system shall be comprised of 6 NanoPPT, each of which having a wet mass lower than 500 g.

After completing a trade-off comparing the most promising propulsion technologies suitable for nano-satellites, it was decided to design the NanoPPT as a breech-fed pulsed plasma thruster (Figure A-1). Considering the power available and aiming at a pulse frequency of about 1Hz, discharge energy of 5 J was selected. The discharge energy density, i.e. the ratio between the discharge energy and the propellant surface exposed to the discharge (E/A), has been fixed at 2.5 J/cm^2 to obtain good performances at the same time allowing a compact thruster design. Moreover, for the selected E/A according to [43], an I_{sp} of 550s is expected. Therefore, the required total impulse and applying a 20% margin on the propellant mass, a total of 30g of PTFE will be used as propellant in each PPT.

The PPT electrodes have been manufactured using a copper tungsten alloy; they will have a spacing of 2 cm and a width of 1 cm resulting in a h/w ratio identical to the one used in PPTCUP-BB [3]. The electrodes are about 2cm long and, in an attempt of improving performances, they are tongue-shaped and flared at 20° [94]. The spark plug uses a copper electrode surrounded by a thin ring of PTFE delivering the discharge ignition at a voltage of about 8kV. The discharge energy is stored in a capacitor bank made of 20 ceramic capacitors charged at a nominal voltage of 1720 V and equivalent to 5 J of energy. The capacitors are the same that were successfully tested to 1,800,000 discharges in the frame of the PPTCUP lifetime verification (§4.2). The assembled PPT, which has an envelope of about $110 \times 30 \times 45 \text{ mm}^3$, is shown in Figure A-1.

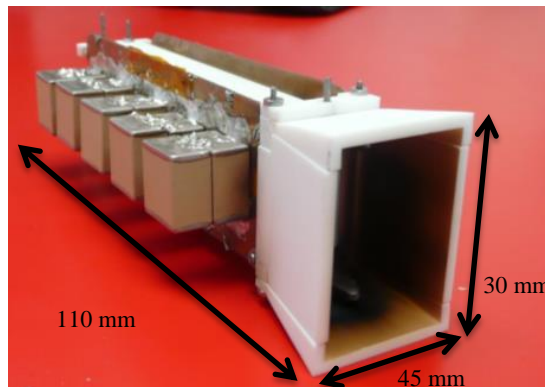


Figure A-1 – Assembled breech-fed NanoPPT

A dedicated electronics board has been designed and manufactured by Clyde Space Ltd. The electronics is split over two boards (Figure A-2): one containing the RS-485 communication interface used to communicate with the satellite and one containing the HV circuitry needed to deliver the required capacitor bank and spark plug voltage. To allow for performance investigation, the capacitor charge voltage can be varied in the range 900 to 1850 V via the RS485 interface. The spark plug voltage is instead fixed at 8 kV. The electronics board assembly has an overall mass of about 100 g and an envelope of about 120x60x30 mm.

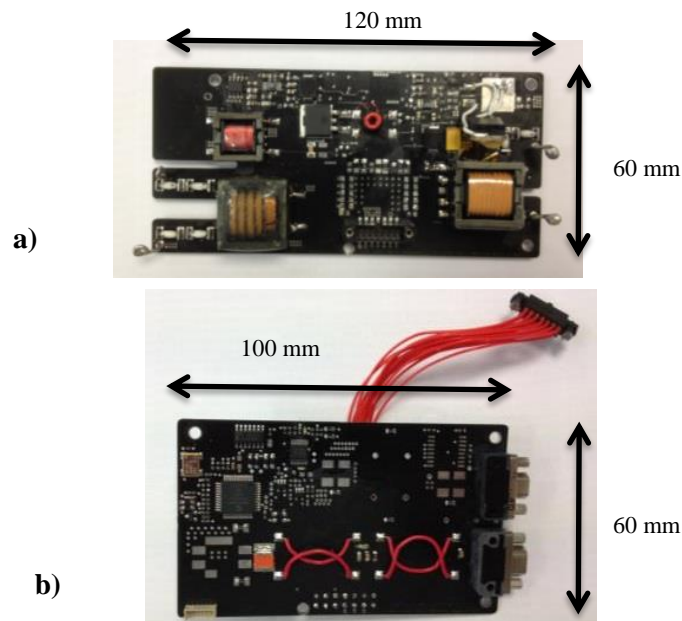


Figure A-2 – PPT electronics a) HV board b) digital board for communications and telemetry

Table A-1 – NanoPPT design parameters

PTFE bar geometry	Breech fed	Thruster wet mass	240g
PTFE mass	30g	Electronics mass	100g
PTFE bar length	6.8 cm	Total wet mass	340g
Required I_{sp}	550 s	Electronics power output	5W
Discharge energy	5 J	Electronics Efficiency	~75%
Nominal capacitor charge voltage	1720V	Electronics capacitor bank charge voltage	900 – 1850 V
Bank capacitance	4uF	Electronics spark plug voltage	8 kV
E/A	2.5 J/cm ²		

1. Experimental set-up

The main aim of the experimental test campaign was to verify the thruster performance against the requirements by measuring the current and voltage curves, the impulse bit and the mass bit consumption. Nevertheless to obtain more data that can be used in the future for thruster optimization, it was decided to perform testing over a wide range of energies, from 3 to 5.5 J. The thruster has been tested in two different configurations for a range of discharge energies. The first configuration (the “nominal” configuration reported in Figure A-3-a) has the capacitor bank mounted as close as possible to the thruster body to minimize the parasitic inductance and improve the thruster performances and it does not allow the use of Rogowski coils. In the second configuration (“wide bank” configuration shown in Figure A-3-b) the capacitor bank has been displaced from the thruster body to allow current monitoring via the incorporation of Rogowski coils between the capacitor bank and the electrodes.

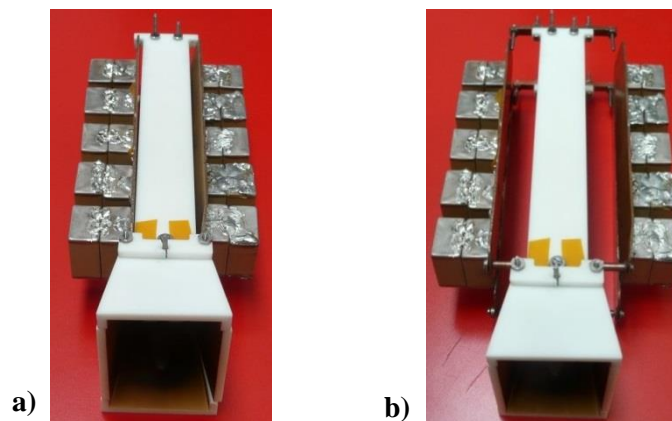


Figure A-3 - NanoPPT configuration: a) configuration 1, nominal, b) configuration 2, “wide” bank

The test campaign was carried out at the University of Southampton. The vacuum chamber used is a stainless steel vertical cylinder with an internal volume of 0.35 m³. It has 6 CF flanges where the electrical F/Ts are installed and a 0.5 m diameter circular main port on the side surface. The vacuum chamber is evacuated by a pumping system comprised of an Edwards roughing pump and by a Pfeiffer Balzers TPH 450 H turbo molecular pump with a pumping speed of 450 l/s backed up by a MD4TC Vacuubrand membrane pump achieving a base pressure of about 5E-6 mbar. The electrical test setups are shown in Figure A-4. It must be noted that during the whole test campaign the electronics low voltage (LV) ground and the chamber ground were always connected to Earth whereas the high voltage (HV) reference potential was left floating. The impulse bit was measured with the direct impulsive

thrust balance described in §3.2.3. The mass consumption has been measured using the Mettler Toledo XP205 mass scale with an accuracy of $\pm 5 \mu\text{g}$ and performing a minimum of 300 shots per energy (1000 shots were performed at energies below 3.5J) achieving a measurement error of less than 3%.

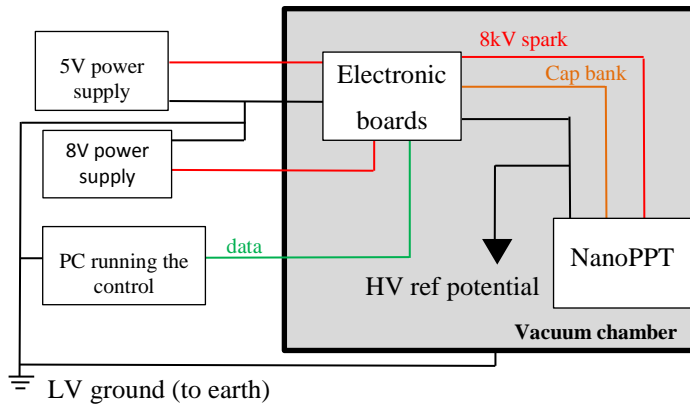


Figure A-4 – Electrical set-up

2. Experimental results

2.1. Electrical characteristics

The first test that was performed had the purpose to characterize the thruster electrically. For each discharge energy ten shots were performed and the discharge voltage and current curves acquired and then the data were averaged. The discharge voltage and current curves for the “wide bank” configuration are reported Figure A-5 and Figure A-6 for various energies. The calculated ψ values are presented in Figure A-7.

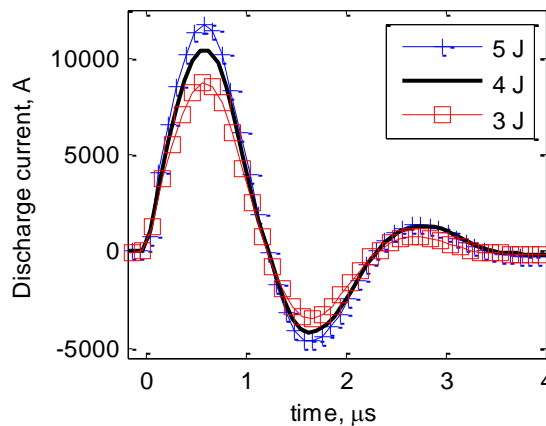


Figure A-5 – Discharge current curves (“wide bank” configuration)

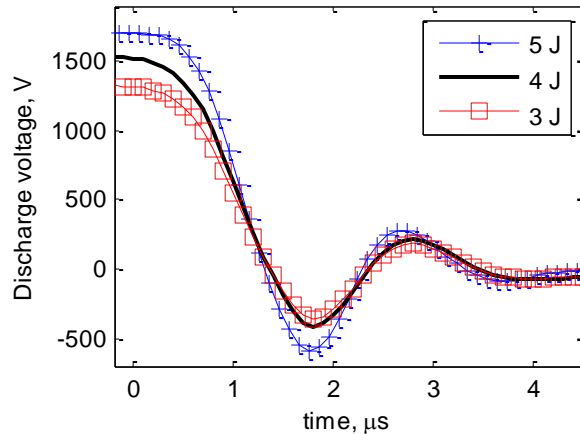


Figure A-6 – Discharge voltage curves (“wide bank” configuration)

The NanoPPT showed an under damped discharge behaviour that expires in about 1.5 cycles similar to the one that was previously measured on the PPTCUP developed [3].

The PPT also showed a very repeatable functioning with a standard deviation values of the current parameter ψ of less than 2% over the full range of energies that were tested (Figure A-7).

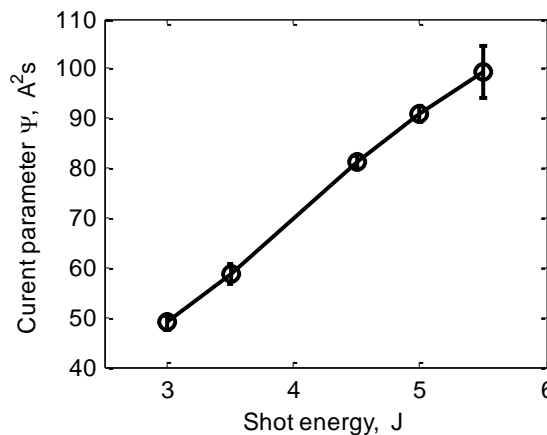


Figure A-7 – Current parameter ψ trend with shot energy (“wide bank” configuration)

The analysis of the discharge curves has been performed by fitting the acquired data with the classic under-damped solution of a RLC circuit. The estimated average NanoPPT electrical parameters are reported in Table A-2.

Table A-2 – NanoPPT electrical parameters

R [m Ω]	L [nH]	C [μ F]
56	41.5	4

Regarding the electrical characterization of the nominal configuration, only the discharge voltage curves were acquired since it was impossible to fit the Rogowski coils. The voltage curves so obtained are shown in Figure A-8 and they are qualitatively similar to those in Figure A-6. The only significant difference is a reduction in the discharge time due to the reduced inductance of the nominal configuration in comparison to the “wide bank” configuration. Comparing the voltage curves relative to the two configurations, a reduction in inductance of about 30% can be calculated based on the reduction in the discharge period and by assuming that the resistance is constant and equal to the value in Table A-2.

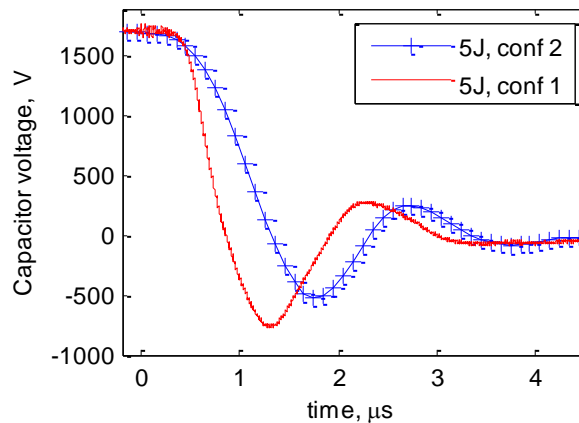


Figure A-8 – Comparison of the typical discharge voltage curves for configuration 1 and 2

2.2. Impulse bit

The impulse bit trend with the energy is shown in Figure A-9.

For each energy value, ten *Ibit* measurements were taken and then averaged. These measurements were performed after the thruster had completed about 1000 shots.

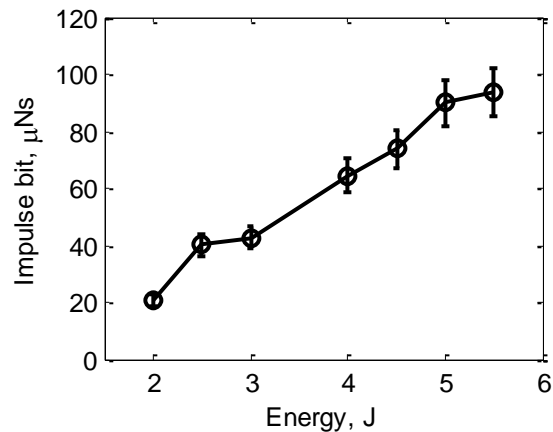


Figure A-9 – Impulse bit trend with energy.

During these tests, the NanoPPT delivered very repeatable performances as the standard deviations of the impulse bit values were less than 3%. It must be noted that the error bars in Figure A-9 include also the balance measurements error that has been quantified to be about 9 %. Moreover, the NanoPPT delivers an *Ibit* of about $90.0 \pm 8.1 \mu\text{Ns}$ at 5J with an *Ibit/E* ratio of about $18 \pm 1.6 \mu\text{Ns/J}$ in line with the typical performances of breech fed pulsed plasma thrusters [1].

2.3. Mass bit and specific impulse

The mass bit trend with energy is reported in Figure A-10 and the I_{sp} values, that have been derived using equation (82), are shown in Figure A-11.

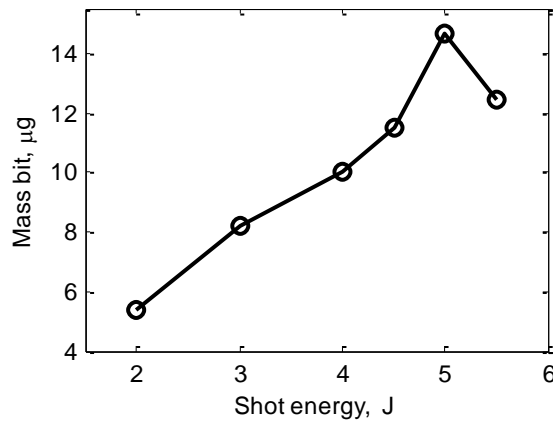


Figure A-10 – Ablated mass bit trend with energy.

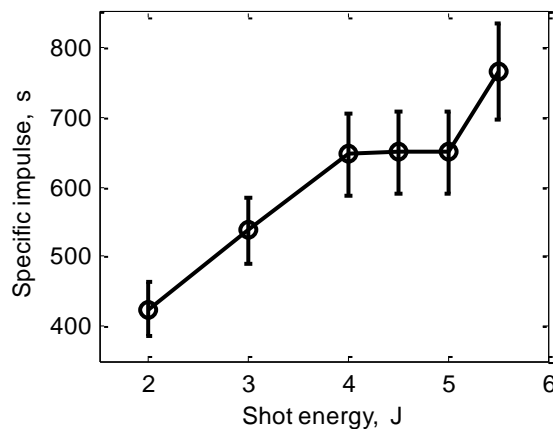


Figure A-11 – Specific impulse trend with energy.

As it can be noted in Figure A-10, the mass bit consumption shows an unusual peak at 5 J of energy. This measurement has been repeated twice (performing a total of 600 shots) but the results obtained did not change appreciably. It has to be noted that also the value of *Ibit* measured at 5 J is higher than the linear fit determined by the

measurements at the other energy values (Figure A-9). This explains why the resulting I_{sp} value does not differ significantly from what is expected based on measurements at the other energy levels. Finally, looking at Figure A-11, it can be noted that the specific impulse value at the nominal energy of 5 J is about 650 ± 56 s hence 18% higher than the requirement of 550 s in Table A-1.

ANNEX B. PPTCUP-QM environment test results

1. Thermal cycling test results

The aim of thermal cycling test was to demonstrate that the unit can work correctly in the range of the operating temperature (from - 20 to + 65 °C). The PPTCUP-QM underwent a 2 hour soak at hot and cold survival temperature limits (from -30 to +75 °C), before being raised to the operational temperature limits (from -20 up to 65 °C) and repeating the cycle in the operative temperature range eight times. Since the test was performed in air, it was not possible to fire the thruster with the bank of capacitors charged within the thermal chamber. However the telemetry and the command interface have been successfully checked during the whole test as it was always possible to communicate with the board.

2. Mechanical test results

High sine burst and random vibration tests were performed along each main axis defined in Figure B-1 respectively to apply a quasi-static load to the thruster as a simulated strength test and to demonstrate that the unit can survive the vibrations at launch. Before and after the sine burst and after the random vibration, a low sine sweep test was carried out to assess the natural frequency of the unit (f_{nat}). As described in §3.4.3, these measured frequencies have to be greater than 150 Hz to avoid resonance coupling with the Cubesat structure. Moreover, the low sine sweep test had also the aim of verifying the structural integrity of the module, since a significant change in the measured f_{nat} could mean that fatal failures occurred. The high sine burst was performed from 5 to 50 Hz at 4g, whereas the low sine sweep test from 5 to 2000 Hz at 0.5g. The random vibration profile is summarized in Table B-1 and it was applied for 60 seconds.

Table B-1 – Random vibration test parameters

Frequency, Hz	Power spectral density, g^2/Hz
20	0.026
20-50	+ 6 dB/oct
50-800	0.16
800-2000	- 6 dB/oct
2000	0.026

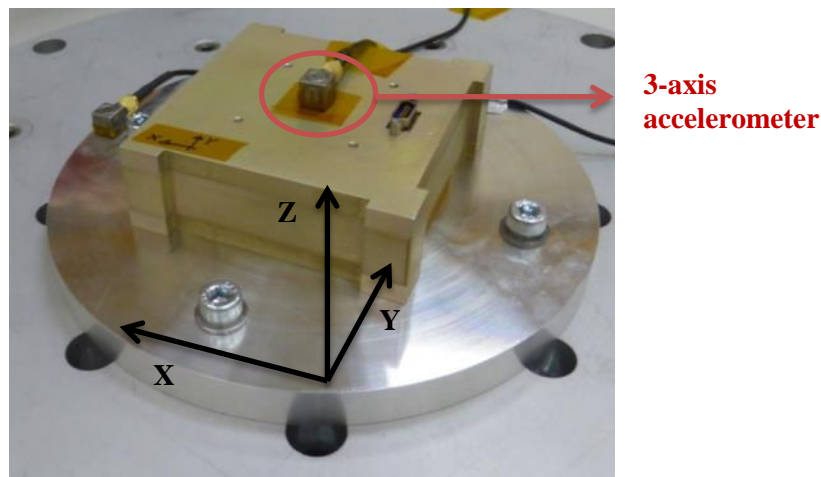


Figure B-1 – Mechanical test set-up

No damage or failures were observed during the vibration testing. The natural frequencies acquired during the sine sweep checks are summarized in Table 4-5. All the measured frequencies are compliant with the requirements (i.e. $f_{nat} > 150$ Hz) and no significant changes in the f_{nat} values were detected. The only exception is the f_{nat} measured along the Z-axis after the first random vibration test. The value changed of about 22% compared to the f_{nat} measured before the same test. Since this has not happen again during the following tests, the reason of such change was likely due to small adjustments of the lateral wall of the external box that occurred during the first performed random vibration test.

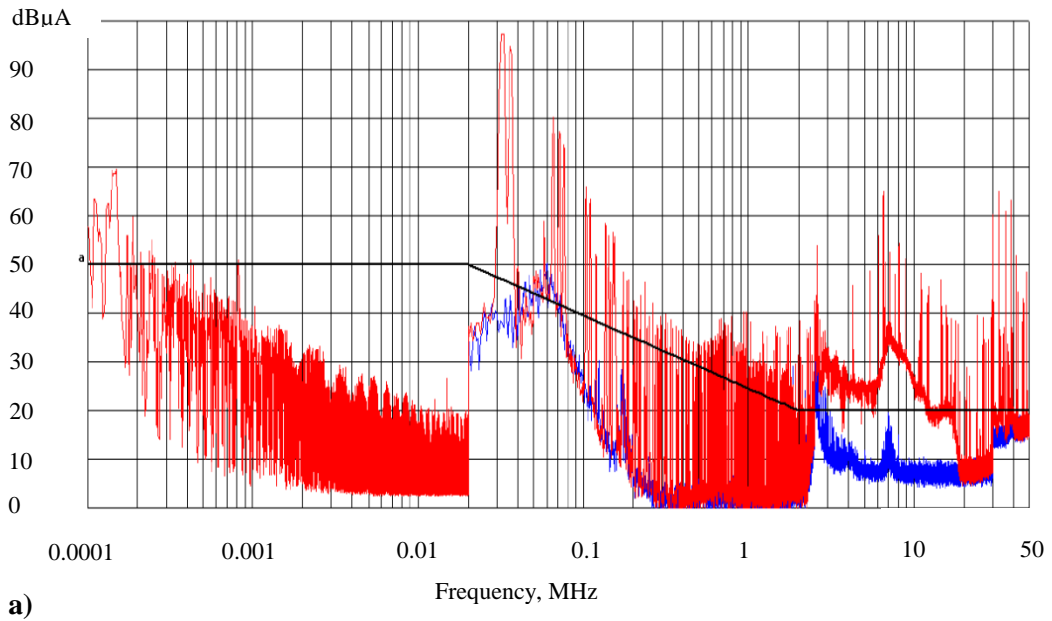
Table B-2 – Low sine sweep test results.

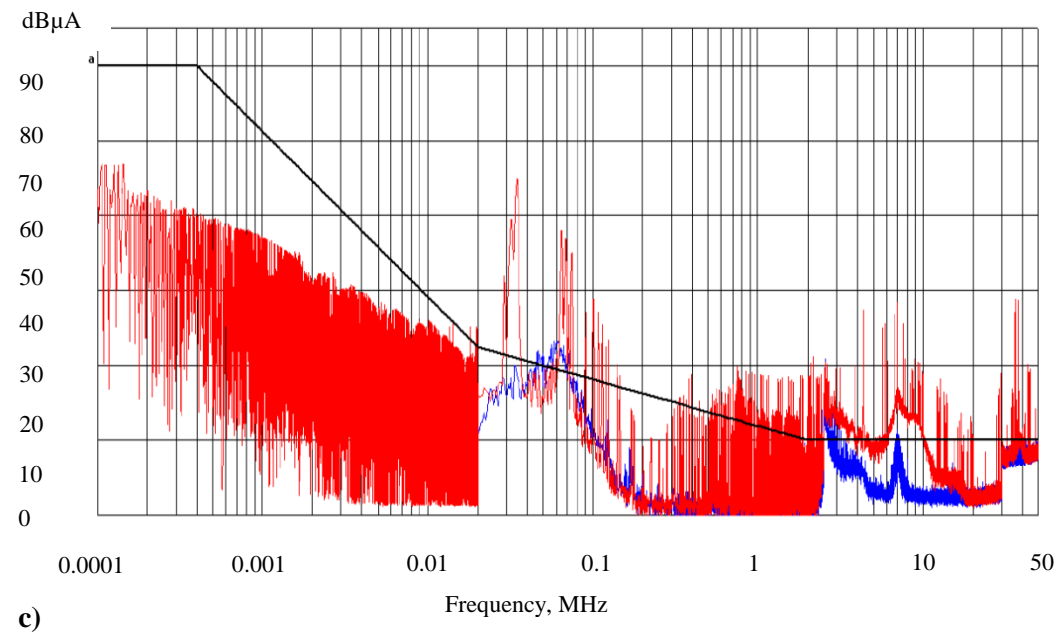
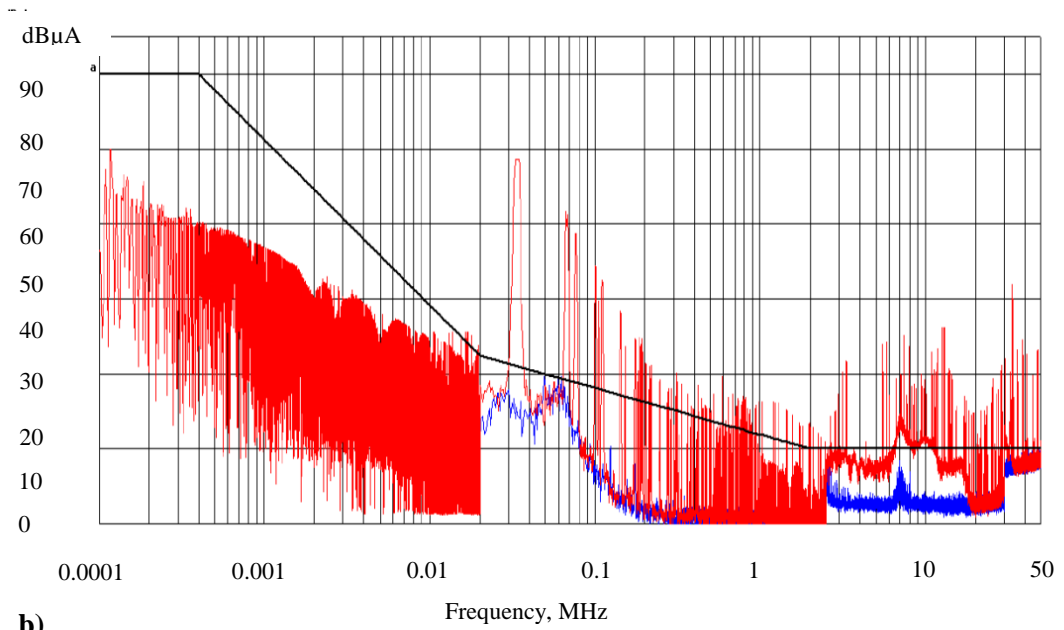
Axis	Test case	Main natural frequency, Hz
Z	Before high sine	584
	After high sine and before random vibration	578
	After random vibration	453
X	Before high sine	1137
	After high sine and before random vibration	1135
	After random vibration	1135
Y	Before high sine	679
	After high sine and before random vibration	676
	After random vibration	660

3. EMC test results

In this section, the diagrams showing all the data acquired during the PPTCUP EMC characterization are reported. In all the figures, the blue and red curves represent respectively the background noise and the noise with the thruster on. The black line indicates the requirements taken from the NASA MIL-STD-461C and 462 EMC standard.

3.1. Conducted emissions





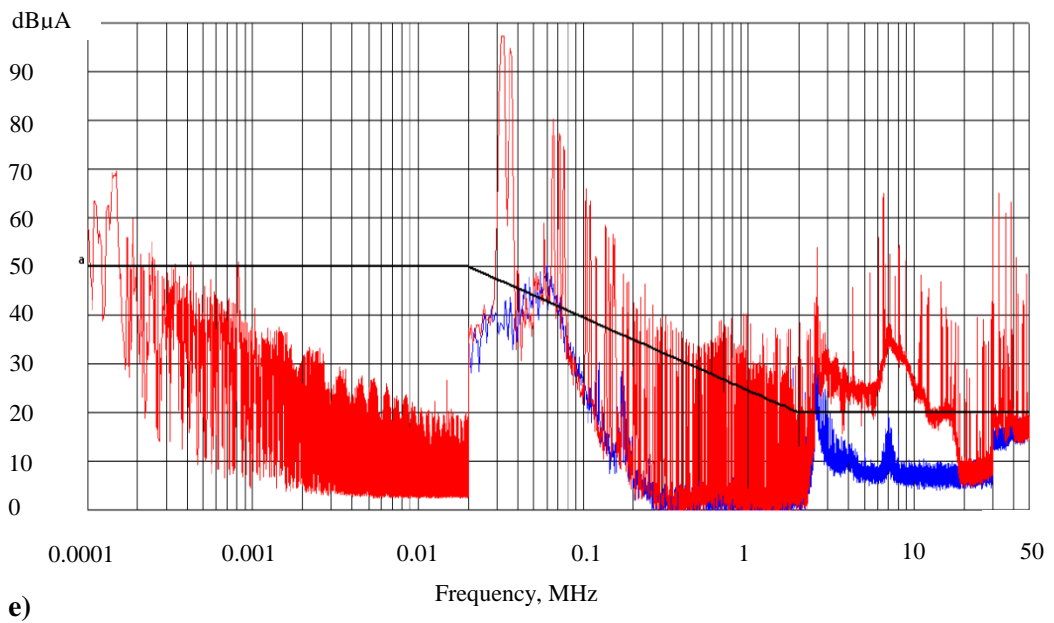
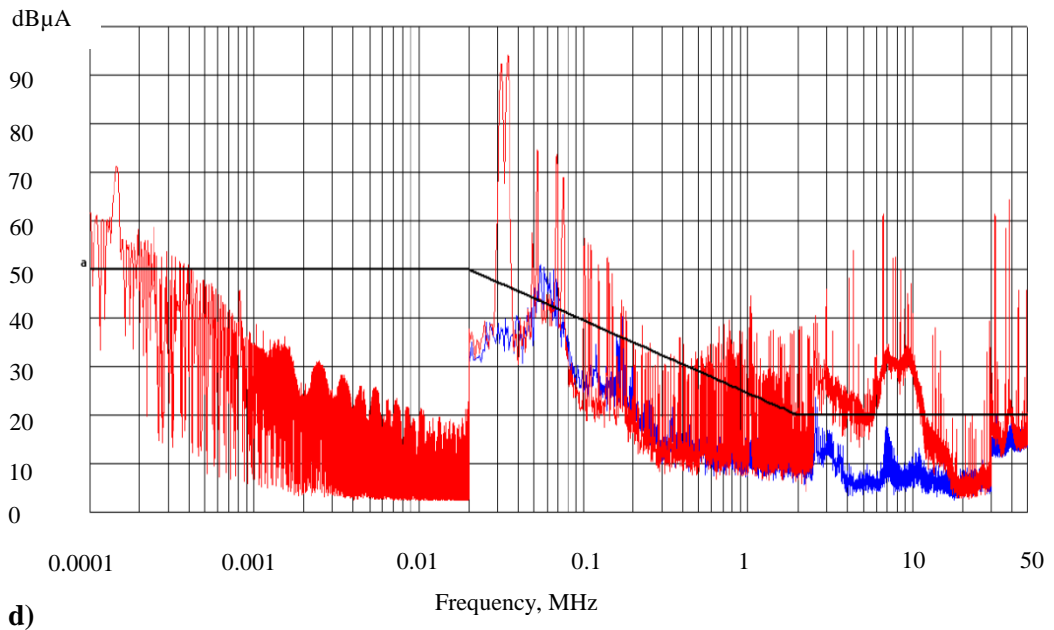
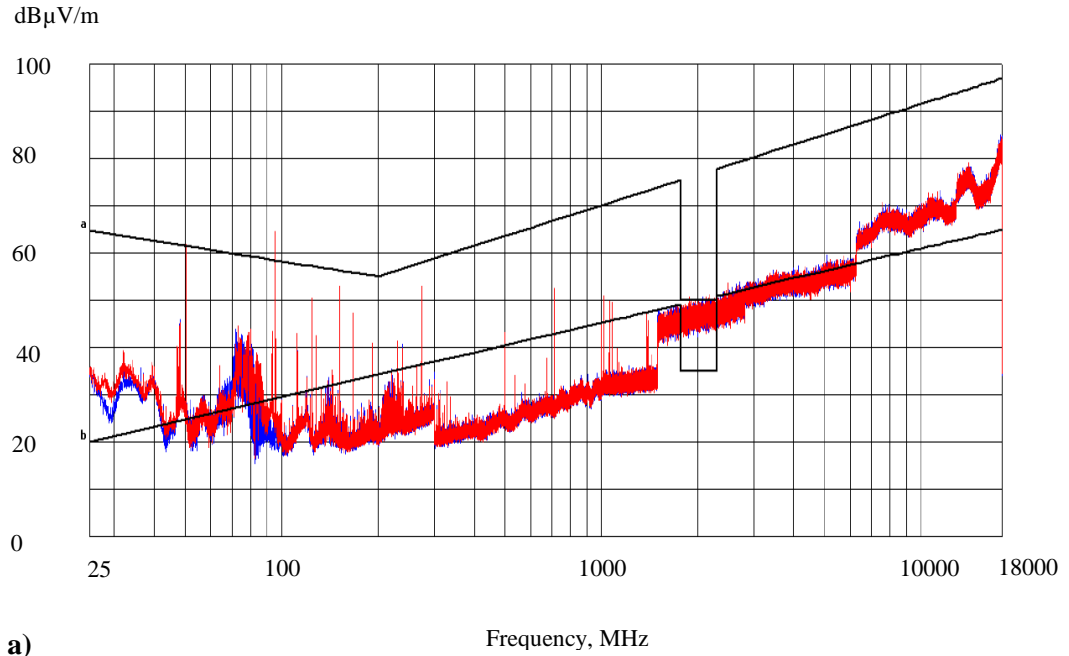
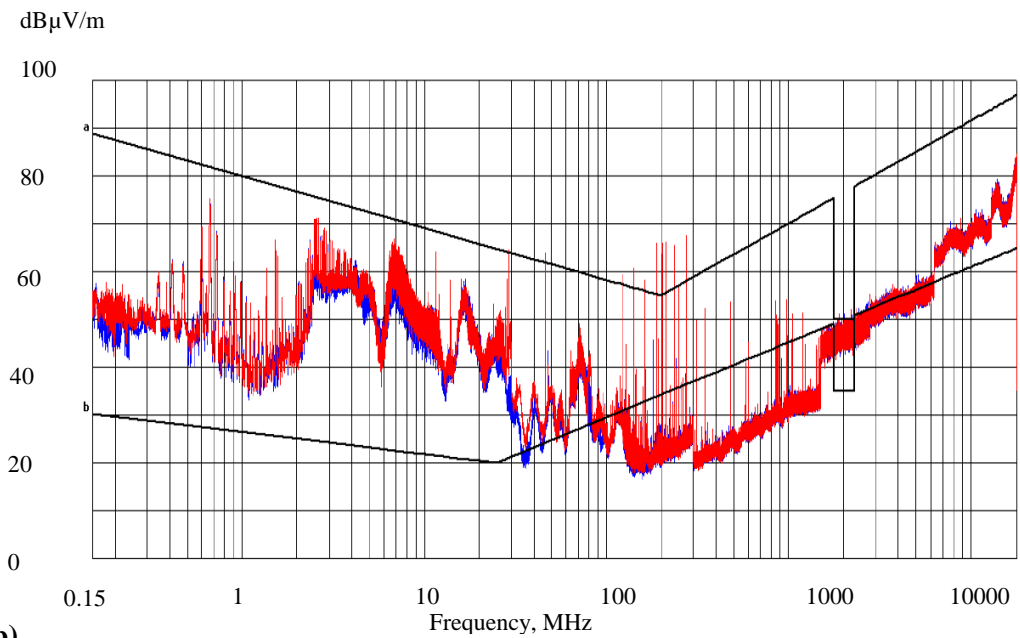


Figure B-2 – PPTCUP conducted emission tests results: a) + 3.3 V differential mode, b) + 7.6 V differential mode, c) ground differential mode, d) +3.3 V common mode and e) +7.6 V common mode

3.2. Radiated emissions



a)



b)

Figure B-3 – PPTCUP electric field radiated emission tests results: a) horizontal antenna arrangement, b) vertical antenna arrangement

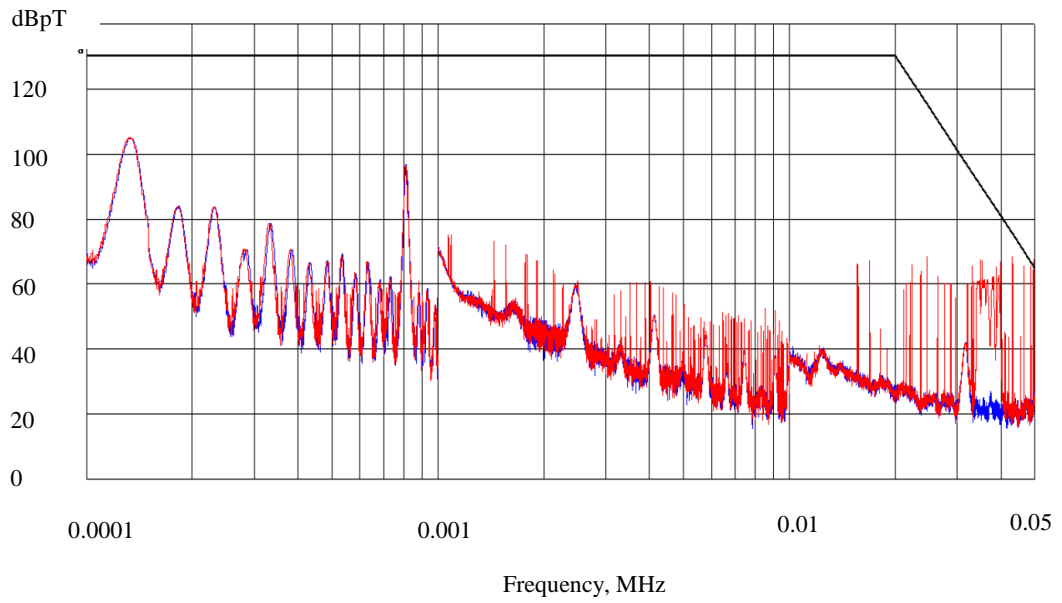


Figure B-4 – PPTCUP magnetic field radiated emission tests results.

List of publications

Peer-reviewed journal articles

- Ciaralli S, Coletti M and Gabriel S B, “*An impulsive thrust balance for μ -PPTs applications*”, *Measurement and Science Technology*, Vol. 24, 115003, 2013
- Coletti M, Ciaralli S and Gabriel S B, “*PPT development for nanosatellites applications: experimental results*”, *IEEE transaction on plasma science*, Vol. 43, no 1, 2015
- Ciaralli S, Coletti M and Gabriel S B, “*Performance and lifetime testing of a Pulse Plasma Thruster for Cubesat applications*”, submitted to *Aerospace Science and Technology*, May 2014
- Ciaralli S, Coletti M and Gabriel S B, “*Performance and lifetime testing of a Pulse Plasma Thruster for Cubesat applications*”, submitted to *Acta Astronautica*, November 2014

Conference proceedings

- M. Coletti, F. Guarducci, A. Mingo Perez, S. Ciaralli, S.B. Gabriel, “*Pulsed plasma thruster development for Cubesats and nanosatellites*”, 2012 4S Symposium, Portoroz, Slovenia, 4-8 June, 2012
- S Ciaralli, F. Guarducci, M Coletti, S.B. Gabriel, “*PPTCUP: performances and extended test results*”, IAA-CU-13-12-07 2nd IAAC Conference on University Satellites Missions and CubeSat Workshop, Rome, Italy, 2013
- M. Compadre, C. Clark, P. Marinov, S. Ciaralli, M. Coletti, S.Gabriel, “*Power Efficient Pulsed Plasma Thruster with Precise Control of High Voltage Generation*“, 10th Annual CubeSat Developers’ Workshop, August 10-11, Logan, Utah, USA, 2013
- S Ciaralli, F. Guarducci, M Coletti, S.B. Gabriel, “*PPTCUP lifetime test results*”, IEPC-2013-164, 33rd International Electric Propulsion Conference, Washington DC, USA, October 2013

- S Ciaralli, M Coletti, S.B. Gabriel, “*An impulsive thrust balance for u-PPTs applications*”, IEPC-2013-165, 33rd International Electric Propulsion Conference, Washington DC, USA, October 2013
- M Coletti, S Ciaralli, S.B. Gabriel, “*PPT development for Nanosatellites applications: experimental results*”, IEPC-2013-198, 33rd International Electric Propulsion Conference, Washington DC, USA, October 2013 (awarded as best paper of the session)
- S Ciaralli, M Coletti, S.B. Gabriel, “*Preliminary results of a qualification test campaign of a Pulse Plasma Thruster for Cubesat Propulsion (PPTCUP)*”, Space Propulsion 2014, 19- 22 May 2014, Cologne, Germany.
- S Ciaralli, M Coletti, S.B. Gabriel, “*Results of the PPTCUP-QM qualification test campaign*”, 65th IAC International Astronautics, 29 September – 3 October 2014, Toronto, Canada (awarded as best paper of the session)

References

- [1] R. L. Burton and P. J. Turchi, "Pulsed Plasma Thruster," *Journal of Propulsion and Power*, vol. 14, no. 5, pp. 716-735, 1998.
- [2] W. J. Guman and D. M. Nathanson, "Pulsed plasma microthruster propulsion system for synchronous orbit satellite," *Journal of Spacecraft*, vol. 7, no. 4, pp. 409-415, 1970.
- [3] M. Coletti, F. Guarducci and S. B. Gabriel, "A micro PPT for Cubesat application: design and preliminary experimental results," *Acta Astronautica*, pp. 200-208, 2011.
- [4] F. Guarducci, M. Coletti and S. B. Gabriel, "Design and testing of a micro pulsed plasma thruster for cubesat application," in *32th IEPC International Electric Propulsion Conference*, Weisbaden, Germany, 2011.
- [5] Mars Space Ltd, 2014. [Online]. Available: <http://www.mars-space.co.uk/Pages/PPTCUP.aspx>.
- [6] W. J. Guman, "Pulsed plasma solid propellant microthruster for the synchronous meteorological satellite," Fairchild Republic company, Farmingdale, NY, 1972.
- [7] W. J. Guman and T. E. Williams, "Pulsed Plasma Microthruster for Synchronous Meteorological satellite," in *10th IEPC International Electric Propulsion Conference*, Lake Tahoe, NV, USA, 1973.
- [8] R. L. Vondra and K. Thomassen, "Flight Qualified Pulsed Electric Thruster for Satellite Control," *Journal of Spacecraft and Rockets*, vol. 11, pp. 613-617, 1974.
- [9] W. J. Guman and D. J. Palumbo, "Pulsed Plasma Propulsion System fo North-South stationkeeping," in *12th IEPC International Electric Propulsion Conference*, Key Biscayne, 1976.
- [10] J. H. Schilling, R. A. Spores and G. G. Spanjers, "Micropropulsion Options for the TechSat21 Space-Based Radar Flight," in *Micropropulsion for Small Spacecraft*, Progress in Astronautics and Aeronautics Series, 2000, pp. 3-23.
- [11] J. Mueller, "Thruster Options for Microspacecraft: a review and evaluation of state-of-art and emerging technologies," in *Micropropulsion for Small Spacecraft*, Progress in Astronautics and Aeronautics Series, 2000, pp. 45-137.
- [12] W. J. Guman, "Designing Solid Propellant Pulsed Plasma Thruster," in *11th IEPC International Electric Propulsion Conference*, New Orleans, LA, USA, 1975.
- [13] W. J. Guman, "Solid propellant pulsed plasma propulsion system design," *Journal of Spacecraft*, pp. 51-53, 1976.

- [14] A. Nawaz, R. Albertoni and M. Auweter-Kurtz, "Thrust Efficiency Optimization of the Pulsed Plasma Thruster SIMP-LEX," *Acta Astronautica*, vol. 67, pp. 440-448, 2010.
- [15] R. L. Burton, M. J. Wilson and S. Bushman, "Energy Balance and efficiency of the Pulsed Plasma Thruster," in *34th AIAA/ASME/SAE/ASEE Joint Propulsion Conference & Exhibit*, Cleveland, OH, USA, 1998.
- [16] R. L. Burton, "Pulsed Plasma Thruster Performance for Microspacecraft Propulsion," in *Micropropulsion for Small Spacecraft*, Progress in Astronautics and Aeronautics Series, 2000, pp. 337-352.
- [17] J. Ziemer, E. Y. Choueiri and D. Birx, "Is the Gas-fed PPT an electromagnetic accelerator? an investigation using measured performance," in *35th AIAA/ASME/SAE/ASEE Joint Propulsion Conference & Exhibit*, Los Angeles, CA, USA, 1999.
- [18] A. Solbes and R. J. Vondra, "Performance study of a solid fuel-pulsed electric microthruster," *Journal of Spacecraft*, vol. 10, pp. 406-410, 1973.
- [19] J. Ziemer, Performance Scaling of Gas-Fed Pulsed Plasma Thrusters (PhD Thesis), Princeton: Princeton University, 2001.
- [20] R. Jahn, Physics of Electric Propulsion, New York: McGraw-Hill, 1968.
- [21] L. B. Holcomb, "Satellite Auxiliary-Propulsion selection techniques," JPL, Pasadena, CA, USA, 1971.
- [22] J. E. Cooley and E. Y. Choueiri, "Fundamentals of PPT discharge initiation: undervoltage breakdown through electron pulse injection," in *39th AIAA/ASME/SAE/ASEE Joint Propulsion Conference & Exhibit*, Huntsville, AL, USA, 2003.
- [23] J. E. Cooley and E. Y. Choueiri, "IR-assisted discharge initiation in pulse plasma thusters," in *38th AIAA/ASME/SAE/ASEE Joint Propulsion Conference & Exhibit*, Indianapolis, IN, USA, 2002.
- [24] H. Horisawa, M. Kawakami and I. Kimura, "Laser-assisted pulsed plasma thruster for space propulsion applications," *Applied physics A: Materials Science & Processing*, vol. 81, pp. 303-310, 2005.
- [25] T. Schonherr, K. Komurasaki and G. Herdrich, "Study on Plasma Creation and Propagation in a Pulsed Magnetoplasmadynamic Thruster," *Word Academy of Science, Engineering and Technology*, vol. 74, pp. 563-569, 2011.
- [26] T. E. Markusic and E. Y. Choueiri, "Visualization of current sheet canting in a pulsed plasma accelerator," in *26th IEPC International Electric Propulsion Conference*, Kitakyushu, Japan, 1999.

- [27] N. N. Antropov, "Application of pulsed plasma thrusters for small satellites," in *3rd international conference on spacecraft propulsion*, 2000.
- [28] G. A. Popov and N. N. Antropov, "Ablative PPT. New quality, New perspectives," *Acta Astronautica*, vol. 59, pp. 175-180, 2006.
- [29] A. I. Rudikov, N. N. Antropov and G. A. Popov, "Pulsed plasma thruster of the erosion type for a geostationary artificial earth satellites," *Acta Astronautica*, vol. 35, pp. 585-590, 1995.
- [30] G. A. Popov and N. N. Antropov, "Development of next generation APPT at RIAME," in *30th IEPC International Electric Propulsion Conference*, Florence, Italy, 2007.
- [31] N. N. Antropov, "Preliminary results on service life development of PPT scale model," in *24th IEPC International Electric Propulsion Conference*, Moscow, Russia, 1995.
- [32] T. E. Markusic, "Ablative Z-pinch pulsed plasma thruster," in *36th AIAA/ASME/SAE/ASEE Joint Propulsion Conference & Exhibit*, 2000.
- [33] M. Keidar, "Performance study of the ablative Z-pinch pulsed plasma thruster," in *37th AIAA/ASME/SAE/ASEE Joint Propulsion Conference & Exhibit*, Salt Lake City, UT, USA, 2001.
- [34] A. Mingo Perez, M. Coletti and S. B. Gabriel, "A micro PPT for Nano-satellite applications: design and experimental results," in *48th AIAA/ASME/SAE/ASEE Joint Propulsion Conference & Exhibit*, Atlanta, GE, USA, 2012.
- [35] T. Schonherr, *Investigation of Performance and Plasma Dynamics of the Pulsed Plasma SIMP-LEX (PhD thesis)*, Tokyo: The University of Tokyo, 2011.
- [36] H. Koizumi, A. Kakami, Y. Kamishima and Y. Arakawa, "Liquid Propellant pulsed plasma thruster," in *28th IEPC International Electric Propulsion Conference*, Toulouse, France, 2003.
- [37] H. Koizumi, Y. Kawazoe, K. Komurasaki and Y. Arakawa, "Performance Improvement of a Liquid Propellant Pulse Plasma Thruster," in *29th IEPC International Electric Propulsion Conference*, Princeton, NJ, USA, 2005.
- [38] D. Simon, H. B. Land and J. Emhoff, "Experimental Evaluation of a micro liquid pulsed plasma thruster concept," in *42nd AIAA/ ASME/SAE/ASEE Joint Propulsion Conference & Exhibit*, Sacramento, CA, USA, 2006.
- [39] R. J. Vondra and K. Thomassen, "Performance improvements in solid fuel microthrusters," *Journal of spacecraft and rockets*, vol. 10, pp. 738-742, 1972.
- [40] J. K. Ziemer, "Performance characterization of a High Efficiency Gas-Fed Pulsed Plasma Thruster," in *33rd AIAA/ASME/SAE/ASEE Joint Propulsion Conference and*

Exhibit, Seattle, WA, USA, 1997.

- [41] J. Ziemer and R. A. Petr, "Performance of Gas Fed Pulsed Plasma Thrusters using water vapour propellant," in *38th AIAA/ASME/SAE/ASEE Joint Propulsion Conference and Exhibit*, Indianapolis, IN, USA, 2002.
- [42] D. J. Palumbo and W. J. Guman, "Effects of propellant end electrode geometry on pulsed ablative plasma thruster performance," *Journal of Spacecraft and Rockets*, vol. 13, no. 3, pp. 163-167, 1976.
- [43] P. Gessini and G. Paccani, "Ablative Pulsed Plasma Thruster System Optimization for microsattelites," in *27th IEPC International Electric Propulsion Conference*, Pasadena, CA, USA, 2001.
- [44] C. Rayburn, M. Campbell, W. A. Hoskins and R. J. Cassady, "Development of a micro pulsed plasma thruster for a Dawgstar nanosatellite," in *36th AIAA/ASME/SAE/ASEE Joint Propulsion Conference & Exhibit*, Huntsville, AL, USA, 2000.
- [45] R. J. Cassady, W. A. Hoskins, M. Campbell and C. Rayburn, "A micro pulsed plasma thruster (PPT) for the "Dawgstar" Spacecraft," in *IEEE Aerospace Conference*, Big Sky, MT, USA, 2000.
- [46] M. Igarashi, "Performance improvement of pulsed plasma thruster for micro satellite," in *27th IEPC International Electric Propulsion Conference*, Pasadena, CA, USA, 2001.
- [47] H. Takegahara, "Evaluation of Pulsed plasma thruster system for u-Lab Sat II," in *27th IEPC International Electric Propulsion Conference*, Pasadena, CA, USA, 2001.
- [48] N. Kumagai, "Research and development status of low power pulsed plasma thruster system for u-Lab Sat II," in *28th IEPC International Electric Propulsion Conference*, Toulouse, France, 2003.
- [49] J. Iio, "Evaluation on Impulse bit characteristics of pulsed plasma thruster by single impulse measurement," in *29th IEPC International Electric Propulsion Conference*, Princeton, NJ, USA, 2005.
- [50] E. J. Pencil, "Evaluation of alternative propellants for pulsed plasma thruster," in *27th IEPC International Electric Propulsion Conference*, Pasadena, CA, USA, 2001.
- [51] G. G. Spanjers, K. A. McFall, F. S. Gulczynski and R. A. Spores, "Investigation of propellant inefficiencies in a pulsed plasma thruster," in *32nd AIAA/ASME/SAE/ASEE Joint Propulsion Conference & Exhibit*, Lake Buena Vista, FL, USA, 1996.
- [52] R. Marques, A mechanism to accelerate the late time ablation for the pulsed plasma thruster (PhD thesis), Southampton: University of Southampton, 2009.

- [53] R. Marques, S. B. Gabriel and F. Costa, "High Frequency burst pulsed plasma thruster research at the university of Southampton," in *30th IEPC International Electric Propulsion Conference*, Florence, Italy, 2007.
- [54] P. G. Mikellides and P. J. Turchi, "Modeling of late-time ablation in teflon pulsed plasma thrusters," in *32nd AIAA/ ASME/SAE/ASEE Joint Propulsion Conference & Exhibit*, Lake Buena Vista, FL, USA, 1996.
- [55] G. G. L. J. S. Spanjers, K. A. McFall and S. R. A, "Propellant losses because of particulate emission in a pulsed plasma thruster," *Journal of Propulsion and Power*, vol. 14, 1998.
- [56] Y. Alexeev and M. N. Kazeev, "Performance study of high power ablative pulsed plasma thruster," in *26th IEPC International Electric Propulsion Conference*, Kitakyushu, Japan, 1999.
- [57] T. E. Markusic and E. Y. Choueiri, "Phenomenological model of current sheet canting in pulsed electromagnetic accelerators," in *28th IEPC International Electric Propulsion Conference*, Toulouse, France, 2003.
- [58] N. N. Antropov, "Development of PPT laboratory model which is as close to the flight one as possible: final report," Moscow, Russia, 1996.
- [59] M. Keidar, "Optimization Issues for a micropulsed plasma thruster," *Journal of propulsions and power*, vol. 22, pp. 48-55, 2006.
- [60] R. Boxman, D. Sanders and P. Martin, *Handbook of vacuum science and technology*, William Andrew Publishing, 1995.
- [61] H. G. Miller and E. J. Furno, "The effect of Mn/Ti surface treatment on voltage holdoff performance of alumina insulators in vacuum," *Journal of Applied Physics*, pp. 5416-5420, 1978.
- [62] M. E. Brady and G. Aston, "Pulsed Plasma Thruster ignitor plug ignition characteristics," *Journal of Spacecraft and Rockets*, vol. 31, pp. 450-451, 1983.
- [63] A. Andres, I. G. Brown, R. A. Mac Gill and M. R. Dickinson, "Triggerless triggering of vacuum arcs," *Journal of Physics*, vol. 31, pp. 584-587, 1998.
- [64] B. Corporation. [Online]. Available: http://en.wikipedia.org/wiki/Bendix_Corporation. [Accessed 2012].
- [65] J. E. Polk, "A theoretical analysis of vacuum arc thrusters and vacuum arc ion thruster performance," *IEEE Transaction on Plasma Science*, vol. 36, pp. 2167-2179, 2008.
- [66] M. Keidar, "Magnetically enhanced vacuum arc thruster," *Plasma sources science and technologies*, vol. 14, pp. 661-669, 2005.

- [67] M. Pietzka, "Development of vacuum arc thrusters and diagnostic tools," in *32nd IEPC International Electric Propulsion Conference*, Weisbaden, Germany, 2011.
- [68] S. Ciaralli, F. Guarducci, M. Coletti and S. B. Gabriel, "PPTCUP: performances and extended test results," in *2nd IAAC Conference on University Satellites Missions and Cubesat Workshop*, Rome, Italy, 2013.
- [69] R. A. Smith, *Semiconductors*, Cambridge: Cambridge University Press, 1959.
- [70] M. Coletti, S. Ciaralli and S. B. Gabriel, "PPT development for Nanosatellites applications: experimental results," in *33rd IEPC International Electric Propulsion Conference*, Washington, DC, USA, 2013.
- [71] F. Karouta, "Structural, compositional and optical properties of PECVD silicon nitride layers," *Journal of Physics D: applied physics*, vol. 45, 2012.
- [72] F. C. Marques, "Stress and thermomechanical properties of amorphous hydrogenated germanium thin film deposited by glow discharge," *Journal of Applied Physics*, vol. 84, pp. 3118-3124, 1998.
- [73] A. Madan and M. P. Shaw, *The physics and applications of amorphous semiconductors*, Academic Press, 1988.
- [74] [Online]. Available: <http://www.southampton-nanofab.com/fabrication/pecvd.php>. [Accessed 2013].
- [75] M. Yudasaka, "Graphite thin film formation by chemical vapour deposition," *Applied Physics Letters*, vol. 64, pp. 842-844, 1994.
- [76] K. L. Chopra and S. K. Bahl, "Structural, electrical and optical properties of amorphous germanium films," *Physical review B*, vol. 1, pp. 2545-2558, 1970.
- [77] E. M. Conwell, "Properties of silicon and germanium," *Proceedings of the I.R.E.*, pp. 1327-1337, 1952.
- [78] M. H. Brodsky, "Structural, electrical and optical properties of amorphous silicon films," *Physical review B*, vol. 1, pp. 2632-2641, 1970.
- [79] A. H. Clark, "Electrical and optical properties of amorphous germanium," *Physical review*, vol. 154, pp. 750-757, 1967.
- [80] F. J. Morin and J. P. Matta, "Conductivity and Hall effect in the intrinsic range of germanium," *Physical review*, vol. 94, pp. 1525-1529, 1954.
- [81] M. Pollak and T. H. Geballe, "Low-frequency conductivity due to hopping processes in silicon," *Physical review*, vol. 122, pp. 1742-1754, 1961.
- [82] J. Schein, "Low mass vacuum arc thruster system for stationkeeping missions," in

26th IEPC International Electric Propulsion Conference, Kitakyushu, Japan, 2001.

- [83] D. Zu Rong, "Novel nanostructures of functional oxide synthesized by thermal evaporation," *Advances functional materials*, vol. 13, pp. 9-24, 2003.
- [84] R. L. Sicotte, "RFI measurements at UHF on a pulsed plasma thruster," *Journal of Spacecraft*, vol. 7, no. 3, pp. 337-338, 1970.
- [85] K. I. Thomassen, "Radiation from Pulsed plasma thrusters," *Journal of Spacecraft*, vol. 10, no. 10, pp. 679-680, 1973.
- [86] R. E. Dolbec, "RFI measurements on a LES-7 prototype pulsed plasma thruster," *Journal of Spacecraft*, vol. 7, no. 7, pp. 889-890, 1970.
- [87] W. A. Hoskins, C. Rayburn and C. Sarmiento, "Pulsed plasma thruster electromagnetic compatibility: history, theory and the flight validation on EO-1," in *39th AIAA/ASME/SAE/ASEE Joint Propulsion Conference and Exhibit*, Huntsville, Alabama, USA, 2003.
- [88] C. Zakrzewski, M. Dabis and C. Sarmiento, "Addressing EO-1 Spacecraft Pulse plasma Thruster EMI Concerns," in *37th Joint Propulsion Conference*, Salt lake City, Utah, USA, 2001.
- [89] J. Ziemer and E. Y. Choueiri, "Dimensionless performance model for gas-fed pulsed plasma thrusters," in *34th AIAA/ASME/SAE/ASEE Joint Propulsion Conference & Exhibit*, Cleveland, OH, USA, 1998.
- [90] P. M. Mostov, J. L. Neuringer and D. S. Rigney, "Electromagnetic acceleration of a plasma slug," *The physics of fluids*, vol. 4, pp. 1097-1104, 1961.
- [91] I. Kohlberg and W. O. Coburn, "A solution for three dimensional rail gun current distribution and electromagnetic fields of a rail launcher," *IEEE Transactions on Magnetics*, vol. 31, pp. 628-633, 1995.
- [92] E. L. Antonsen, "Effects of postpulse surface temperature on micropulsed plasma thruster operation," *Journal of Propulsion and Power*, vol. 21, pp. 877-883, 2005.
- [93] I. Kohlberg, "Prediction of electromagnetic fields generated by a rail guns," Army Research Laboratory, ARL-CR-128, 1995.
- [94] A. Nawaz, G. Herdrich, H. L. Kurt and T. Schonherr, "SIMP-LEX: systematic geometry variation using thrust balance measurements," in *30th IEPC International Electric Propulsion Conference*, Florence, Italy, 2007.
- [95] T. Schonherr, "Influence of the electrode shape on the performance of the pulsed MPD thruster SIMP-LEX," *Journal of Propulsion and Power*, vol. 25, pp. 380-386, 2009.
- [96] S. Ciaralli, M. Coletti and S. B. Gabriel, "An impulsive thrust balance for applications of micro-pulsed plasma thrusters," *Measurement Science and Technology*, p. 115003,

2013.

- [97] H. Koizumi, K. Komurasaki and Y. Arakawa, "Development of thrust stand for low impulse measurement from microthrusters," *Review of Scientific Instruments*, vol. 75, p. 10, 2004.
- [98] D. Krejci, B. Seifert and C. Scharlemann, "Thrust measurement of a micro pulsed plasma thruster for Cubesats," in *1st IAAC Conference on University satellites missions and Cubesat workshop*, Rome, Italy, 2011.
- [99] A. V. Oppenheim, *Discrete-time signal processing*, Englewood Cliffs, NJ: Prentice-Hall, 1999.
- [100] J. R. Taylor, *An introduction to error analysis. The study of uncertainties in physical measurements*, Mill Valley, CA: University Science Books, 1997.
- [101] F. Guarducci, G. Paccani and J. Lehnert, "Quasi-steady MPD performance analysis," *Acta Astronautica*, vol. 68, pp. 904-914, 2011.
- [102] K. Kawahara, "Study on plume characteristics of pulsed plasma thruster," in *28th IEPC International Electric Propulsion Conference*, Toulouse, France, 2003.
- [103] P. Hill and C. Peterson, *Mechanics and Thermodynamics of Propulsion*, Addison-Wesley Publishing Company, Inc, 1992.
- [104] S. Rocca, "ONERA micronewton thrust balance: analytical modeling and parametric analysis," *Aerospace Science and Technology*, vol. 15, pp. 148-154, 2011.
- [105] F. Guarducci, *Design and testing of a micro PPT for Cubesat applications (PhD thesis)*, Rome, Italy: University of Rome La Sapienza, 2011.
- [106] Pumpkin Cubesat structure, 2014. [Online]. Available: <http://www.cubesatkit.com/content/design.html>.
- [107] D. J. Palumbo and W. J. Guman, "Continuing development of the short pulsed ablative space propulsion system," in *8th AIAA/SAE Joint Propulsion Conference*, New Orleans, LA, USA, 1972.
- [108] D. J. Palumbo and W. J. Guman, "Propellant side-fed short pulsed discharge thruster," Fairchild Industries, Inc, Farmingdale, NY, USA, 1972.
- [109] D. Krejci, B. Seifert and C. Scharlemann, "Endurance testing of a pulsed plasma thruster for nanosatellites," *Acta Astronautica*, vol. 91, pp. 187-193, 2013.
- [110] H. Tahara, "Flowfield calculation of electrothermal pulsed plasma thruster for teh PROITERES satellite," in *32th IEPC International Electric Propulsion Conference*, Weisbaden, Germany, 2011.

- [111] R. J. Vondra, K. Thomassen and A. Solbes, "Analysis of solid teflon pulsed plasma thruster," *Journal of Spacecraft and Rockets*, vol. 7, no. 12, pp. 1402-1406, 1970.
- [112] G. Paccani and L. Petrucci, "Self-applied magnetic field intensity effects on solid propellant MPD thruster performance," in *27th IEPC International Electric Propulsion Conference*, Pasadena, CA, USA, 2001.
- [113] N. N. Antropov, "Low bank energy APPT for micro satellites," in *30th IEPC International Electric Propulsion Conference*, Florence, Italy, 2007.
- [114] M. Hirata and H. Murakami, "Electromagnetic noise measurement study of pulsed plasma engine," in *15th AIAA/JSASS/DGLR International Electric Propulsion Conference*, Las Vegas, Nevada, USA, 1981.
- [115] S. Ishigami and I. Takashi, "Two-source model of transient electromagnetic fields generated by electrostatic discharge," in *International Symposium on EMC*, Tokyo, Japan, 1999.
- [116] S. Silver, *Microwave antenna theory and design*, New York: Mc Graw-Hill Book Company, Inc, 1949.
- [117] S. Benson, L. Arrington, Q. Hoskins and N. Meckel, "Development of a PPT for the EO-1 Spacecraft," in *35th AIAA/ASME/SAE/ASEE Joint Propulsion Conference and Exhibit*, Los Angeles, California, USA, 1999.
- [118] C. Rayburn, M. Campbell and T. Mattick, "Pulsed plasma thruster system for microsatellites," *Journal of Spacecraft and Rockets*, vol. 42, no. 1, pp. 161-170, 2005.
- [119] P. Molina-Cabrera, "Pulsed Plasma Thrusters: a worldwide review and long yearned classification," in *32nd IEPC International Electric Propulsion Conference*, Weisbaden, Germany, 2011.
- [120] M. Keidar, "Analysis of teflon surface charring and near field plume of a micro-pulsed plasma thruster," in *27th IEPC International Electric Propulsion Conference*, Pasadena, CA, USA, 2001.
- [121] M. Coletti, R. Marques and S. B. Gabriel, "Design of a two-stage PPT for cubesat application," in *31st IEPC International Electric Propulsion Conference*, Ann Arbor, Michigan, USA, 2009.
- [122] S. Ciaralli, M. Coletti, F. Guarducci and S. B. Gabriel, "PPTCUP lifetime test results," in *33rd IEPC International Electric Propulsion Conference*, Washington, DC, USA, 2013.